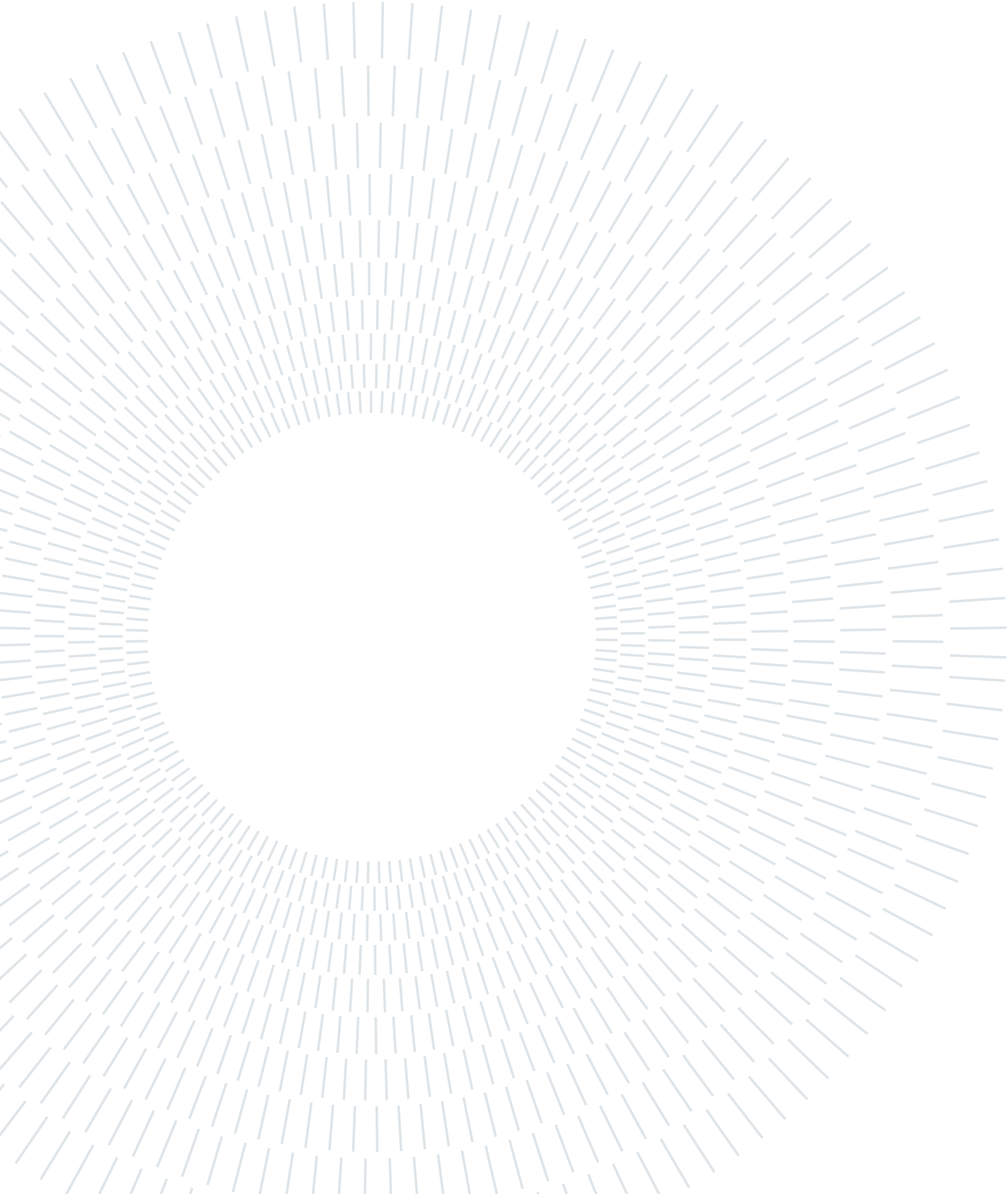

POLITECNICO
MILANO 1863

SCUOLA DI INGEGNERIA INDUSTRIALE
E DELL'INFORMAZIONE

Skoltech
Skolkovo Institute of Science and Technology

Dimmings lifetime: Methods to study the recovery of solar corona after coronal mass ejections

Tesi di Laurea Magistrale in
Space Engineering - Ingegneria Spaziale

Author: **Giulia Maria Ronca**

Student ID: 940553
Advisor: Prof. Giovannni Consolati
Co-advisors: Prof. Tatiana Podladchikova
Academic Year: 2021-22

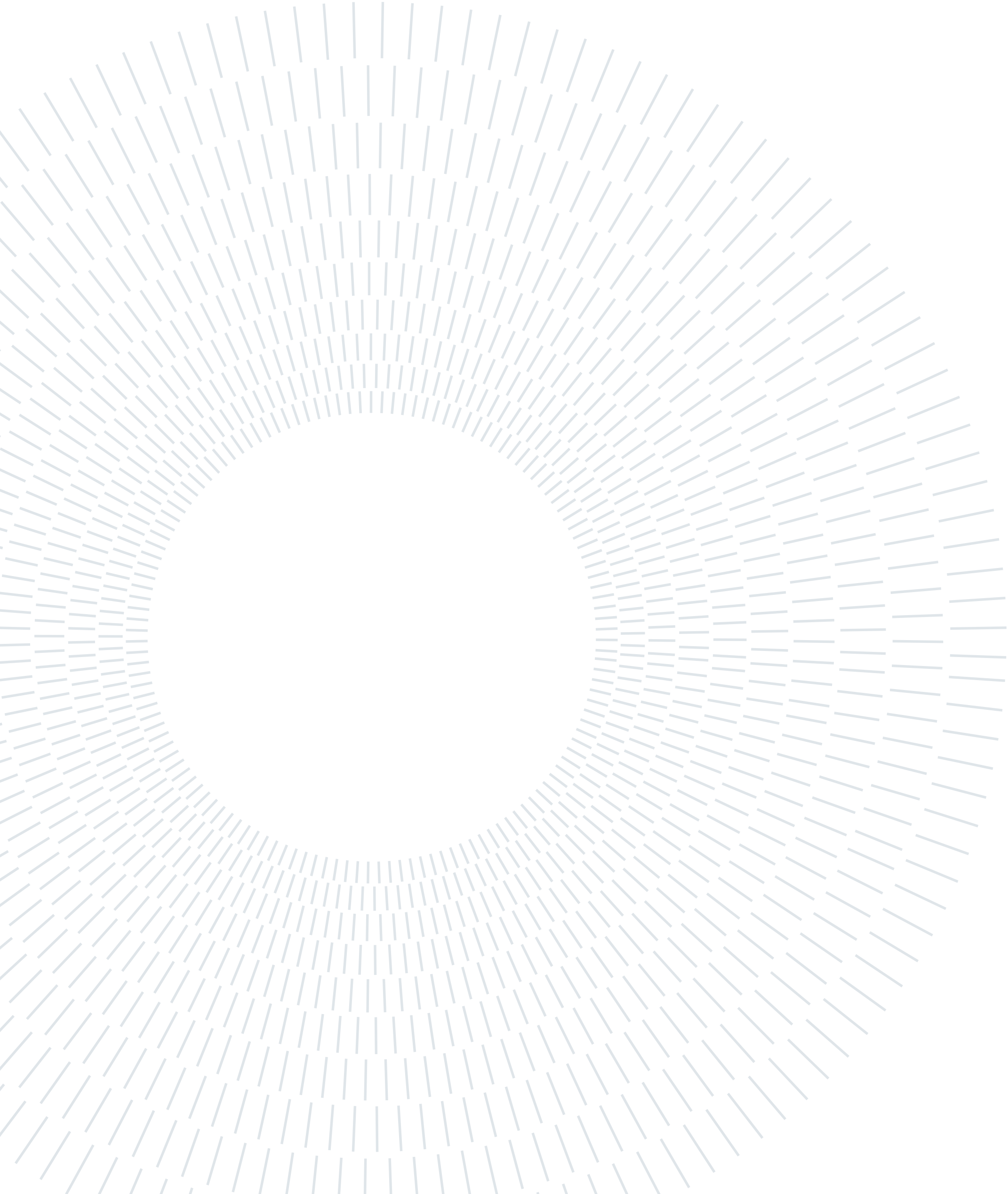

Abstract

The Sun's activity shapes and varies the conditions in the heliosphere, so-called Space Weather. The main driver of Space Weather disturbances in the Near-Earth environment are Coronal Mass Ejections (CMEs), huge clouds of magnetized plasma, expelled from the Sun into interplanetary space with speeds ranging from 100 km/s up to 3000 km/s. Especially for Earth-directed events, the most important to humankind, determining accurate characteristic CME parameters is challenging. Thus, CME associated phenomena are investigated. Among these, coronal dimmings are regions in the solar corona that abruptly undergo a drastic decrease of emission, observed in the extreme ultraviolet (EUV) or soft X-rays (SXR). They are interpreted as a density depletion caused by the evacuation and expansion of coronal plasma due to CME eruptions. On the one hand, characteristic coronal dimming properties may inform on the early CME mass and speed, on the other hand their post-event recovery is important to understand the mass replenishment of the corona after such eruptions. The current project makes use of the high cadence observations by NASA's SDO satellite and aims at developing and testing automatic algorithms to detect coronal dimmings occurring on-disk for four different event cases, segmenting areas of interest and studying the long-term time evolution of dimming relevant parameters, such as their area and brightness as the corona recovers. The algorithms are developed by using the Sunpy package of the Python language. New approaches to investigate the temporal evolution of the dimming are proposed and their limitations due to the long analysis duration (up to three days) have been identified. By focusing on very specific regions in the image, either with the application of a fixed mask or with the restriction of the analysis to 3×3 pixel boxes, it was possible to eliminate the disturbances coming from the surrounding areas on the solar disk and to limit the artifacts detected by the algorithm in the case of events close to the limbs. It is found that the dimming recovery mechanism for three of the cases under study is due to the shrinking of the outer boundaries and refilling of the loops, while the last case may show replenishment due to emerging flux from below. Lastly, long-living areas which do not recover by the end of the analysis time range are identified and their behaviour is compared with the peripheral dimming regions. Overall, the trend seems to work in accordance to what is suggested by Attrill et al. [2008].

Keywords: Sun; Coronal Mass Ejections (CMEs); solar flares; coronal dimmings

Abstract in lingua italiana

L'attività solare influenza le condizioni dell'eliosfera ed è studiata dalla Meteorologia Spaziale (Space Weather). I principali artefici dei disturbi causati dallo Space Weather sono le espulsioni di massa coronale (CME), enormi nuvole di plasma magnetizzato espulso nello spazio interplanetario con velocità da 100 fino a più di 3000 km/s. Soprattutto nel caso di espulsioni in direzione della Terra (le più importanti per il genere umano) determinare parametri accurati è complicato. Per questo motivo, l'indagine si sposta su fenomeni associati ai CME. Fra questi, ci sono i coronal dimming, regioni nella corona solare in cui si registra un improvviso calo di emissioni, sia nell'estremo ultravioletto (EUV) che nei soft X-rays (SRX). I dimming sono considerati una diminuzione di densità dovuta alla fuoriuscita ed espansione di plasma causata da un CME. Da un lato, le proprietà dei dimming possono dare informazioni su massa e velocità dei primi stadi di un CME, dall'altro, il loro ritorno alle condizioni iniziali in seguito a un evento è importante per comprendere il rifornimento di massa della corona dopo un'eruzione. Il presente progetto di tesi fa uso delle osservazioni ad alta cadenza del satellite SDO (NASA) e sviluppa e testa algoritmi automatizzati per il rilevamento di dimming sul disco solare nel caso di quattro eventi, ne segmenta le aree di interesse e studia l'evoluzione di parametri rilevanti, come area e intensità, per lunghi periodi (fino a tre giorni). Gli algoritmi sono sviluppati nel linguaggi di programmazione Phython. Sono stati proposti nuovi approcci allo studio dell'evoluzione temporale dei dimming e i loro limiti, dovuti alla lunga durata, sono stati identificati. Infatti, tramite l'utilizzo di una maschera unica applicata su tutte le immagini oppure la restrizione dell'analisi a quadrati di 3×3 pixel, si è riusciti a eliminare i disturbi provenienti da aree limitrofe al dimming in studio e a limitare le distorsioni create da uno degli algoritmi per la vicinanza ai bordi del disco solare. Il risultato è che per tre dei casi analizzati, il meccanismo di riempimento dei dimming per tornare allo stato pre-eruzione si basa principalmente sul restringimento dei bordi, mentre nel restante caso il processo è dovuto a flusso che emerge da sotto. Infine, aree del dimming che non presentano un ripristino allo stato originario neanche alla fine del periodo di tempo scelto sono state identificate e il loro comportamento è confrontato con le regioni del dimming periferiche. In generale, si è trovato riscontro con quanto indicato da Attrill et al. [2008].

Parole chiave: Sole; espulsione di massa coronale (CME); brillamento solare; dimming coronale

Contents

Introduction

Motivation

Activity on the Sun influences the entire Solar system and hence the Earth, its environment and human activities. The Sun creates a type of weather called Space Weather, which is defined by NOAA/SWPC as "the variations in the space environment between the Sun and Earth. In particular Space Weather describes the phenomena that impact systems and technologies in orbit and on Earth." [105]

Space Weather can sometimes be harmful to either technologies both on-ground and in space or to the astronauts' health. Thus, a major scientific effort is related to the prediction of Space Weather activity.

The most powerful and most energetic drivers of the Sun activity are Coronal Mass Ejections (CMEs), which are huge clouds of magnetized plasma, expelled from the Sun into interplanetary space with speeds in the range of some 100 km/s up to >3000 km/s. Their forecast can be difficult especially in the case of Earth-directed plasma ejections, where projection effects lead to systematic inaccuracies [18]. A possible approach to the problem is based on the study of phenomena that are associated to CMEs, namely coronal dimmings, as they may allow scientists to retrieve information about the early stage of CMEs and their characteristic properties.

Coronal dimmings are defined as transients regions of strongly reduced emissions in soft X-rays [70] [131] and Extreme-Ultraviolet (EUV) [138], which are wavelenghts sensitive to active region plasma the CMEs consist of. Coronal dimmings are considered to be the footpoints of CMEs in the low corona [139] and are generally interpreted as density depletions caused by mass loss due to the CME eruption [156]. For these reasons, coronal dimmings are studied with the final long-term aim of implementing a method to better forecast CMEs.

Goal of the thesis

The main objective of this thesis is the analysis of the lifetime of coronal dimmings, focusing mainly on the end-of-life and on the recovery mechanism. So far, they have been studied for a limited number of hours after the eruption time ([87] [24] [35]) in order to analyse the area growth and expansion direction. However, the final stage of coronal dimmings has only been analysed in a few studies (e.g., [79], [7], [118]). With dimmings being interpreted as areas of reduced intensity and density compared to the surrounding environment, the main questions of this thesis are "Do coronal dimmings recover to the pre-eruption condition?" and if yes, "How does the process work? Is the recovery due to a replenishment of the plasma or to a progressive shrinking of the dimming area?".

In particular, this thesis aims at explaining the approach to the development of tools for this new type of analysis and their functioning in order to provide future investigations with useful and dependable means for this long-period analysis.

Thesis Layout

The layout of the rest of the thesis is as follows:

The first chapter summarizes the theoretical basis on which this thesis is founded; it is followed, in the second chapter, by an updated review of the scientific literature on coronal dimming, presenting the approaches to detect the dimming regions and the current explanations about the recovery mechanisms. The third chapter introduces the datasets used and describes the methodology of the conducted analysis. The fourth chapter contains the results and their discussion. The final chapter summarizes and suggests further research related to the present work.

1 | Introduction to Solar Physics

1.1. An overview of the Sun

The Sun is one out of the 100 billions stars in the Milky Way galaxy. It is a G-type (G2V) main-sequence star, a yellow dwarf. This type of stars are abundant in our galaxy, an example being Alpha Centauri, the next closest star to us, which is also a G2V star.

The Sun was born about 4.5 billion years ago from a cloud of hydrogen-dominated interstellar gas collapsing because of gravity. At a certain point, the fusion of ionized hydrogen into helium became the powering mechanism of this star and counteracted the gravitational collapse, stabilizing the Sun's size. The Sun entered the main sequence with the beginning of nuclear fusion in its core. This gravitational equilibrium, which fuels the Sun, is expected to persist for about 10 billion years and, as any star that progresses through the main sequence, the Sun will gradually brighten due to a slowly increasing rate of fusion in its core. This, in possibly 3-4 billions of years, will lead to an increase of temperature on Earth which will doom life on our planet [70].

Overall, the Sun is an average star in our universe, but it is remarkable for humankind and life on planet Earth. The distance between the Sun and the Earth is called Astronomical Unit (AU) and is equal to $\sim 150 \cdot 10^6\ km$. Table 1.1 contains some relevant parameters about our star.

The Sun produces energy at the rate of $4 \cdot 10^{26}\ W$, equivalent to transforming approximately four million tons of mass into energy every second. The mass of the Sun is about 330 000 times that of the Earth and during the entire solar lifetime in the main sequence less than 0.1% of the solar mass will be turned into energy.

Solar Parameter	**Value**
Radius	696000 km
Mass	$1.989 \cdot 10^{30}$ kg
Luminosity (energy output of the Sun)	$3.846 \cdot 10^{33}$ erg/s
At surface of the Sun	
Temperature	5770 K
Gravitational acceleration	274 m/s^2
Density	$2.07 \cdot 10^{-7}$ g/cm^3
Composition	70% H, 28% He, 2% (C, N, O, ...) by mass
Escape velocity at surface	618 km/s
At center of the Sun	
Central temperature	$15.6 \cdot 10^6$ K
Central density	150 g/cm^3
Central composition	35% H, 63% He, 2% (C, N, O, ...) by mass
Solar age	$4.57 \cdot 10^9$ yr

Table 1.1: Relevant Solar parameters.

1.1.1. Solar Interior

The solar interior can be divided into three main parts [100].

- *The core.*
  This portion of the Sun, which is 200 000 km across, is where nuclear fusion supplies the main source of energy, then transported through the next part, the radiation zone.

- *The radiation zone.*
  This part extends from 0.3 to 0.7 solar radii and rotates as a solid body, according to helioseismology (i.e., the study of the Sun interior by using sound waves). Here, energy is transported mainly by electromagnetic photons .

- *The convection zone.*
  This area is situated above the radiation zone and is the region where the energy is predominantly transported via convective motion to the solar surface. It is approximately 200 000 km thick

There is a substantial distinction between the radiation zone and the convection zone.

As mentioned above, in the former the Sun rotates as a solid body. On the contrary, in the convection zone the Sun moves according to a differential rotation, meaning the Sun moves at different velocities at different latitudes (i.e., the equator rotates faster than the poles). The layer separating the two regions is called *tachocline* [146] and is believed to be a component of the solar dynamo, which is connected with the solar cycle [52].

1.1.2. Solar Atmosphere

As explained in Sec. 1.1.1, the Sun does not exactly have a solid surface. However, it does have a super-heated atmosphere, made of solar material bound to the Sun by gravity and magnetic forces: the atmosphere is the region where rising heat and pressure push the solar material away from the Sun, until the point where gravity and magnetic fields are too weak to contain such material, hence it can directly escape to space. This point is known as the Alfvén critical surface and marks the end of the solar atmosphere and beginning of the solar wind.

Three layers can be identified in the solar atmosphere, with the addition of a transition region. They contain energy that comes from the solar interior and arrives to Earth in the form of sunlight. They are:

- the *photosphere*,
- the *chromosphere*,
- the *transition region* between the chromosphere and the next layer, that is
- the *corona*.

The lowest layer is the *photosphere* (the "sphere of light"), where most of the Sun's energy is emitted. The temperature of the photosphere ranges from $\sim 6500\ K$ at the bottom to $4000\ K$ at the top [161]. It is about 500 kilometers thick [142].

The photosphere has a "granulation structure" where bright areas (showing a Doppler blue shift) denote plasma going from the convection zone up to the surface and the dark boundaries (showing red shift) are where the plasma descends towards the solar interior. The bright regions have a lifetime of 5 to 10 minutes and a size of $1000\ km$ from side to side. They are generally $500K$ hotter than the dark boundaries [100].

Not only is the photosphere characterized by these bright, bubbling granules of plasma, but also by the so-called sunspots, emerging when the Sun's magnetic field breaks through the surface (see Fig.1.1). Indeed, sunspots are regions of strong magnetic field ($\sim 3000\ G$) compared to the rest of the photosphere, where the magnetic field has intensity of a few Gauss. This strong difference inhibits convection. Their temperature is lower with respect to their surroundings, typically $4500K$ compared to the $5800K$ of the photosphere, which is what makes them look darker. They are usually about 10 000 km wide and can last from a few days to a few months, until their decay.

Sunspots appear to move across the Sun's disk, in fact they were used by Galileo Galilei to estimate the solar rotation rate. Later, Richard Carrington was the one to determine that the Sun rotates differentially, because it actually is not a solid body. The Sun's equatorial regions rotate in about 25 days, while the polar regions take more than 30 days (generally 36) to make a complete rotation ([142] [100]). The solar rotation period seen from the Earth and determined from the observation of sunspots is 27.27 days [107].

Two parts can be discerned within a sunspot: the central umbra (the darkest part), where the magnetic field is approximately vertical (normal to the Sun's surface) and at a maximum strength of 2000–4000 G, and the surrounding penumbra (brighter compared to the central part), where the magnetic field is more inclined [74]. Sunspots usually appear in pairs of opposite magnetic polarity [107]. A directivity relative to the direction of solar rotation characterizes the polarity of these pairs. In each hemisphere of the Sun, a leading spot has the same polarity of the dominant dipole field in that hemisphere, whereas the polarity of a trailing spot is the opposite [99].

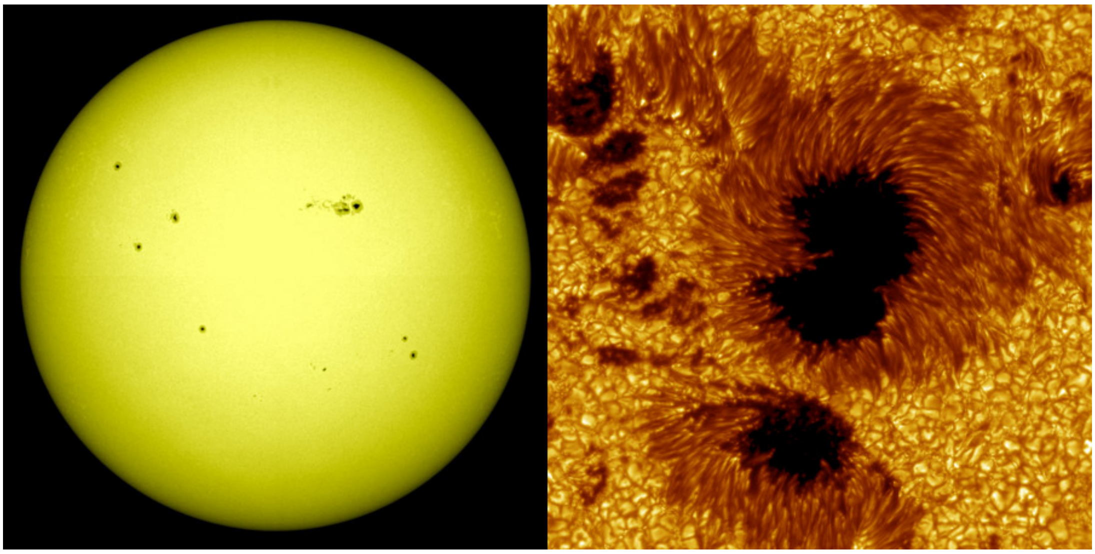

Figure 1.1: *Left:* Photosphere. The dark spots on the surface are sunspots, either alone or in groups. *Right:* closeup view of the photosphere. The dark areas are sunspots, where the umbra and penumbra can be easily distinguished. The granulation structure is observable surrounding the sunspots. *Courtesy of NASA/SDO and the AIA (4500 Å) science teams (left) and Royal Swedish Academy of Sciences - Göran Scharmer and Mats Löfdahl (right)*

Nowadays space-based instruments such as the Helioseismic and Magnetic Imager (HMI) onboard the Solar Dynamics Observatory (SDO) and the Solar Optical Telescope (SOT) aboard the Hinode satellite enable us to measure the intensity of the magnetic field at the visible surface of the Sun and to obtain high-resolution spectropolarimetric data, respectively.

The next layer is the *chromosphere* ("sphere of color"), which is about 1500 km thick. It is characterized by a maximum temperature of about 10 000 K at the height of 2000 km, much higher than the 4100 K temperature at the border with the photosphere [10]. On the other hand, the density of plasma (and so the amount of emitted light) undergoes a rapid decrease as the chromosphere height increases. Because of this, the chromosphere is not visible together with the bright photosphere and only during solar eclipses it is possible to observe a rosy red color, due to the H-alpha (Hα) emission line of hydrogen (i.e., a specific transition of an electron within the hydrogen atom that is associated to a unique wavelength within the visible light). Indeed, the chromosphere is generally observed in Hα and CaII (ionized calcium) wavelengths [100].

The chromosphere can be very dynamic with solar flares, prominence and filament eruptions. They will be described later in Chapter 1.2.2. In the chromosphere, also hot jets of gas called spicules can be observed. They can extend thousands of kilometers above the solar surface. They originate from material that is expelled at velocities of about 20 to 100 km/s [100].

Above the chromosphere, there is a thin layer in which the temperature increases dramatically with height: it is the *transition region*. It is only a few hundred km wide, but the temperature increases by two orders of magnitude (from $\sim 10^4 K$ in the chromosphere to $\sim 10^6 K$ in the corona) whereas the density drops by two orders of magnitude. The behaviour of temperature throughout the atmosphere is visible in Fig 1.3.

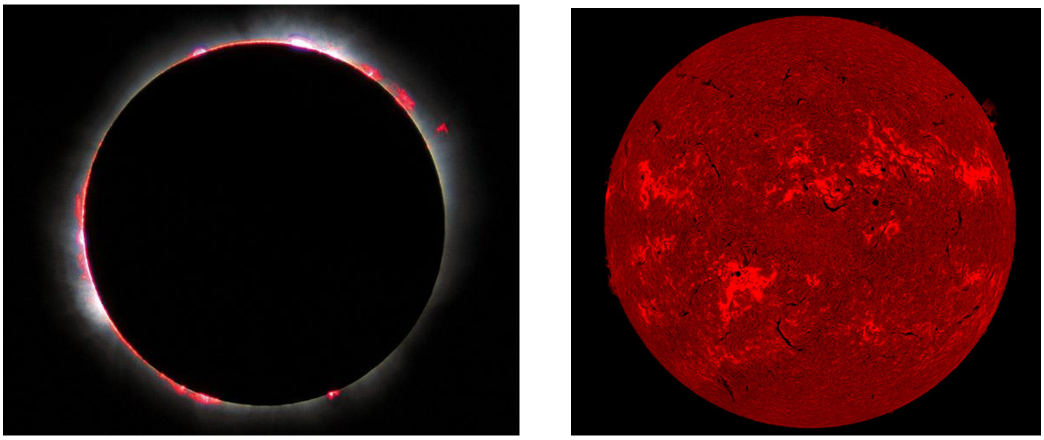

(a) Chromosphere during solar eclipse on August 11 1999. *Credit: Luc Viatour.*

(b) Chromosphere seen with $H\alpha$ (6562.8 Å) filter on July 18 2000. *Credit: Big Bear Solar Observatory.*

Figure 1.2: *Panel a*: the chromosphere appears as a rim of red light during a solar eclipse. *Panel b*: Several solar filaments (dark thin line-like structures) are visible and a few sunspots can be observed as small, black dots. Lighter-colored areas are plages, i.e. magnetically disturbed "active regions".

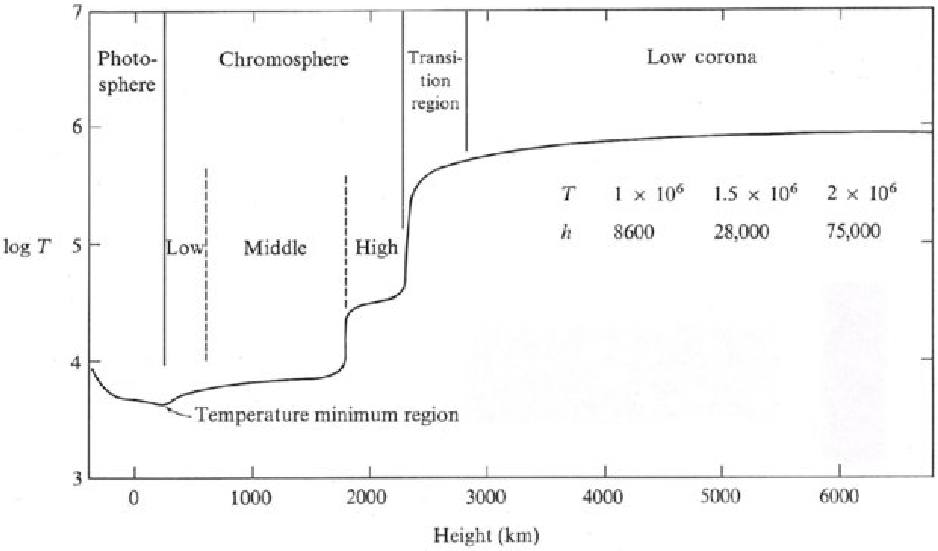

Figure 1.3: Temperature evolution across the solar atmospheric layers. Temperature decreases in the photosphere until it reaches a minimum value. In the chromosphere there is an increase until T= 10 000 K at the height of 2000 km. Then, the transition region is characterized by a sharp rise, of about two orders of magnitude, in a considerably short width, of just a few hundred km. Finally, in the solar corona, temperature is around $\sim 10^6 K$. *Courtesy of [5].*

The last layer of the Sun's atmosphere is the *corona* ("crown"), which extends several million kilometers above the photosphere and chromosphere. The order of magnitude of the temperature is $\sim 10^6 K$, while the density is so low (around 10 million times less dense than the solar surface) that special instruments, called coronographs, are necessary for its observation: working on the same principle of eclipses, they cover the solar disk and filter all the bright photosperic light, enabling the visualization of the much less bright corona. Due to the high temperature, the number density of atomic hydrogen decreases steeply with the dissociation into free electrons and protons. Helium too is deprived of its electrons. Thus, the dominant elements are fully ionized in this intense heat, while heavier elements, namely iron and calcium, still manage to keep some electrons. Partially due to the very low density and thus the low heat capacity, coronal gases are producers of X-rays.

Particles in the corona move with a very high speed because of the extreme temperature, reaching and overcoming the Sun's escape velocity (618 km/s in the low corona). These particles form a stream, called solar wind. There is no clear separation between the solar corona and the solar wind, so the former is considered continuous with the latter. As the height increases, so does the temperature and the consequence is an outflow of pressure-driven solar wind [109]. The solar wind is responsible of dragging the coronal magnetic field out in the entire heliosphere, forming the so-called Heliospheric Magnetic Field (HMF) [106]. The HMF is the only part of the Sun's magnetic field that is accessible to direct measurements.

Having a better understanding of how the solar magnetic field exactly works is one of the objectives of present and future space missions, namely the Parker Solar Probe by NASA which successfully entered the Sun's corona in April 2022 and the ESA's Solar Orbiter [65], launched in February 2020. There are also other on-going space mission whose aim is to investigate the corona and monitor its activity, thanks to the above-described coronographs, namely the LASCO coronograph on-board SOHO satellite [52] and the two coronographs on-board STEREO-A satellite [158]. The solar corona, as observed by the LASCO coronograph, can be seen in Fig.1.4.

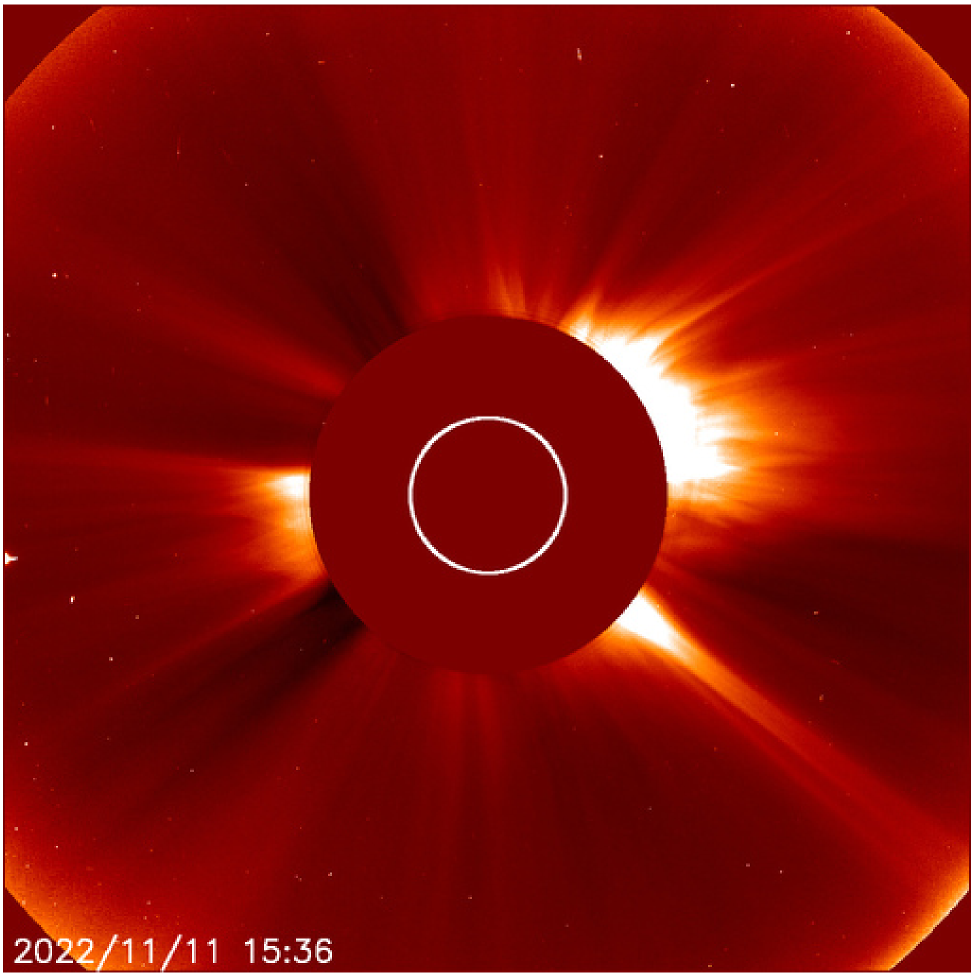

Figure 1.4: The image of the corona on November 11, 2022 by the LASCO coronagraph. *Courtesy of NOAA Space Weather Prediction Center.*

There are still unanswered questions about the solar corona and the most important is related to its high temperature. Why is the corona hotter than the Sun's surface? Why does the temperature increase along with the distance from the Sun's interior hot source? This puzzling behaviour has been deduced since the 1930's and after several decades of study, two processes were identified as the basis of the heating mechanism. The first one is based on the concept of wave heating, which identifies different types of waves as the producers of turbulence in the convection zone. The second one relies on the concept of magnetic heating: energy is released through the magnetic reconnection in the form of solar flares of different sizes [44]. Nowadays, the focus of modern research is on the latter, based on the theory of the Swedish scientist Hannes Alfvén. According to this theory, magnetised waves of plasma are able to carry huge amounts of energy from the Sun's interior to the corona along the so-called solar magnetic flux tubes. In doing so, they bypass the photosphere and then burst in the Sun's upper atmosphere producing the high temperature of the corona [96]. Thus, these magnetised waves of plasma, called Alfvén waves, are the only ones that do not refract or dissipate before reaching the corona and even there are hard to dissipate. Investigations to explain the magnetic heating are currently taking place although the problem is now differently analysed in the case of magnetically closed corona (quiet Sun and active regions) and open corona (coronal holes and solar wind) [82].

1.1.3. Solar Cycle

It has been observed that the number of sunspots on the Sun continuously changes. They typically have lifetimes from a few days to few months, but the total number of sunspots changes with a quasi-regular 11-year cycle, that is hence called solar cycle. The solar cycle describes the level of activity of the Sun, since sunspots are associated with different phenomena, namely flares, which release energy. In theory, the average period of the solar cycle is 11.2 years but its duration is variable between 8 and 15 years. The most active or energetic time interval within the cycle is called solar maximum, whereas the time of least activity is known as solar minimum. During a solar minimum little heating of the upper atmosphere of the Sun is taking place, on the contrary flares and other events heat localized regions of the Sun's atmosphere during a solar maximum.

As sunspots are areas of strong magnetic fields, the variation in their number means also a variation in the solar magnetic field. It does indeed change over a 22-years cycle (also called double solar cycle or Hale cycle [59]) after which the polarity of the Sun's field reverses [100]. The polarity of the sunspots pairs (leading sunspot - trailing sunspot) is also defined by this cycle and reverses around every 11 years.

During solar minimum the Sun's magnetic field is relatively simple and resembles a dipole magnetic field, with the magnetic field originating from one hemisphere and ending in the other. As the Sun approaches solar maximum, it becomes magnetically disorganized and highly structured, losing the dipole appearance. Past solar maximum, the magnetic field again becomes more organized and more dipolar. At the beginning of the solar cycle the sunspots tend to locate at middle latitudes in both hemispheres (opposite polarities across the hemispheres) and during the cycle they progressively appear at lower latitudes until there are no sunspots at the end of the cycle. In the next cycle the process repeats, but the orientation of sunspots is reversed.

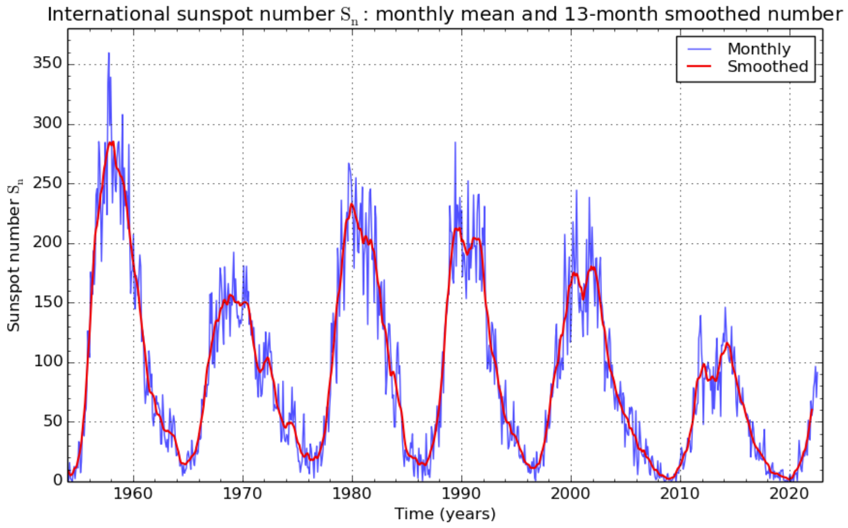

SILSO graphics (http://sidc.be/silso) Royal Observatory of Belgium 2022 August 1

Figure 1.5: The monthly mean sunspot number (blue) and 13-month smoothed monthly sunspot number (red) for the last six cycles. *Courtesy of SILSO graphics, Royal Observatory of Belgium.*

The first to identify the solar cycle was the German astronomer Heinrich Schwabe, in 1843. Six years later, Johann Rudolf Wolf invented a method for the calculation of the solar activity cycle based on counting the number of sunspots R:

$$R = k \cdot (10G_n + S_n) \tag{1.1}$$

where G_n is the number of sunspot groups (regions), S_n is the total number of individual spots in all the groups and k is a scaling factor that corrects for seeing conditions. This formula is still being used to compute R for prediction and analysis of the solar cycle [25]. The cycles are numbered since 1761 and now the the 25^{th} solar cycle is at its beginning. The cyclical behavior of the number of sunspots in the past few years can be seen of Fig.1.5. It is interesting to observe how the 24^{th} solar cycle is weaker compared to the previous ones (it has a lower number of sunspots). Forecasting solar activity behaviour is important for determining the lifetime of satellites in low-Earth orbit, as the drag on the satellites correlates with the solar cycle: a solar maximum is implies higher drag with respect to the solar minimum, thus leading to a decrease of the satellite life. Moreover, solar cycle predictions give a rough idea of the frequency of space weather storms of all types and of their effects on technology (as it will be explained in Chap. 1.1.5). Thus, various agencies and many industry groups demand and use these prediction data to estimate the expected impact of space weather in the coming years. This topic is indeed the subject for scientific research and many papers try to predict the 25^{th} solar cycle maximum ([117] [64] [17]).

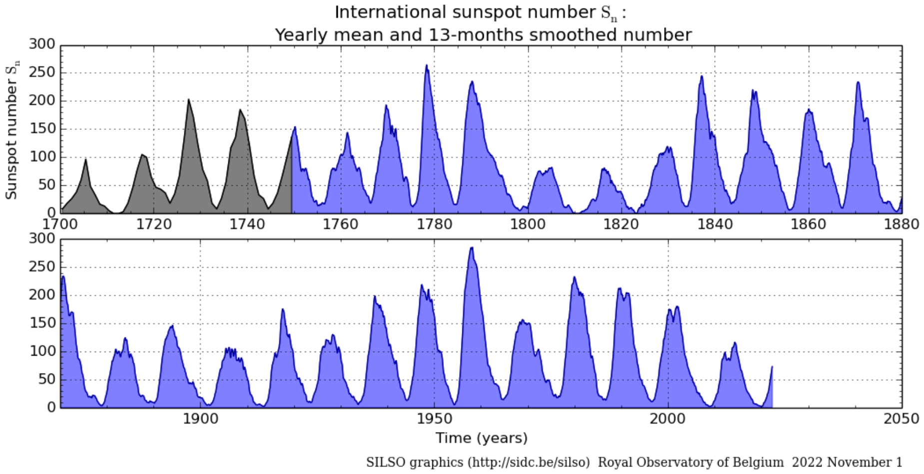

Figure 1.6: Yearly mean sunspot number (black) up to 1749 and monthly 13-month smoothed sunspot number (blue) from 1749 up to the present. *Courtesy of SILSO graphics, Royal Observatory of Belgium.*

1.1.4. Magnetic Field

As mentioned before the motion of conductive plasma inside the Sun generates a magnetic field. The solar magnetic field is on average about 1 Gauss. This value is twice the Earth's magnetic field. Furthermore, because of the massive surface of the Sun (12 000 times larger than Earth's one), the overall influence of the Sun's magnetic field is significant. The strongest magnetic field is observed close to sunspots regions, which often represent pairs of opposite magnetic polarities [58] and indicate the solar cycle.
The solar wind pulls part of the Sun's magnetic field out into the heliosphere and this is hence called Interplanetary Magnetic Field (IMF). IMF is characterised by a spiral configuration, when viewed from above of below the equatorial plane. This configuration is due to the Sun's rotation. The outflowing solar wind expands radially (directly away from the Sun) and pulls the solar magnetic field along with it. However, the Sun rotates in the meantime, so the position (or footpoint) of where the solar wind stream leaves the solar surface moves counter-clockwise. In this way, the magnetic field starts to spiral as it moves farther from the Sun with respect to the original footpoint position. This twisting is known as Archimedian spiral [100] and this phenomenon is called Parker Spiral. Then the solar wind, and hence the magnetic field, move far into space until reaching and interacting the planets' magnetospheres (if they have it) in several and complex ways.

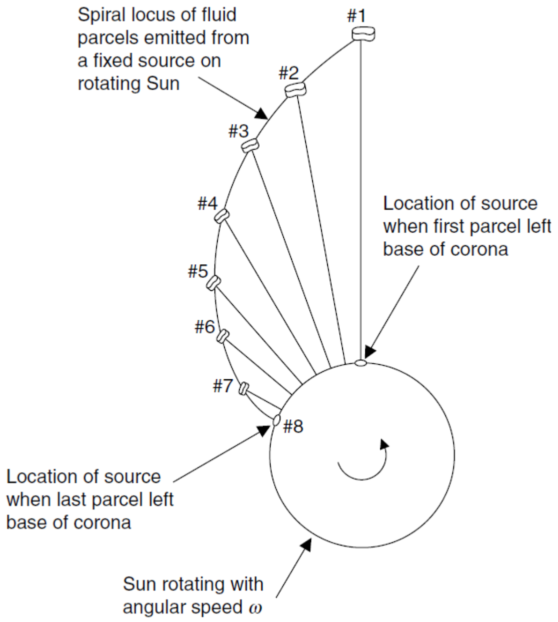

Figure 1.7: Location of eight parcels emitted at constant speed from a source fixed on the rotating Sun. The solar wind expands radially, and pulls the magnetic field along with it: because of the Sun's rotation, the magnetic field is wrapped into an Archimedian spiral. *Courtesy of [72] [100].*

Nowadays, the explanation of the solar magnetic cycle is based on the magnetohydrodynamic (MHD) dynamo theory. This theory investigates the generation and evolution of magnetic fields and describes them as complex nonlinear processes involving interactions between plasma flows within the solar interior and the magnetic field. In other words, the solar cycle generates and recycles (which means it feeds on the energy available in plasma motions) two components of the magnetic field: the poloidal component and the toroidal component [103]. The former has an observed radial component that is vertical field on the solar surface. The toroidal component is thought to be produced by the non-uniform differential rotation of the Sun which stretches and deforms the initial poloidal field (the dynamo Ω-effect) [108]. The poloidal field has to be then regenerated from the toroidal field in a process known as the dynamo α-effect.

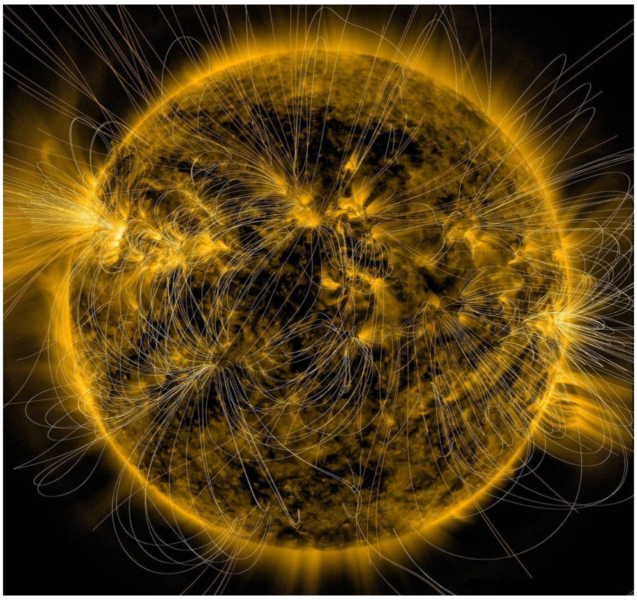

Figure 1.8: Sun's magnetic fields overplotted the image by NASA's SDO on March 12, 2016. Magnetic fields are densest near the bright spots visible on the sun (magnetically strong active regions). Many of the field lines link one active region to another. *Courtesy of NASA.*

Typical magnetic field strengths for various parts of the Sun are:

Part of the Sun	**Magnetic Field Value**
Polar Field	$1 - 2\ G$
Sunspots	$3000\ G$
Prominences	$10 - 100\ G$
Chromospheric plages	$200\ G$
Bright chromospheric network	$25\ G$
Ephemeral (unipolar) active region	$20\ G$

Table 1.2: Magnetic field strengths for different parts of the Sun.

1.1.5. Space Weather

As mentioned before, "Space Weather describes the variations in the space environment between the Sun and Earth. In particular, Space Weather describes the phenomena that impact systems and technologies in orbit and on Earth. Space weather can occur anywhere from the surface of the sun to the surface of Earth. As a space weather storm leaves the sun, it passes through the corona and into the solar wind. When it reaches Earth, it energizes Earth's magnetosphere and accelerates electrons and protons down to Earth's magnetic field lines where they collide with the atmosphere and ionosphere, particularly at high latitudes. Each component of space weather impacts a different technology." [105] To summarize, Space Weather refers to conditions on the Sun, in the solar wind and within Earth's magnetosphere, ionosphere and thermosphere which are able to impact the performance of both space-born and ground-based technologies and can possibly pose a threat to human life or health. [126].

There are different effects on modern technologies: communications, computers, power supplies and navigation system could be damaged or destroyed and the astronauts' health may be endangered. For these reasons, Space Weather is gaining more and more importance as time passes and scientific research progresses. Several space missions have been launched and some spacecraft have observed or are observing the Sun in order to obtain information. The final aim is to be able of predicting solar events. This matters especially from a temporal point of view: flashes of X-rays and EUV light reach the Earth only in 8 minutes, while other events can take hours or even some days to reach Earth.

In the case of *X-rays and EUV rays*, they heat and ionize the upper layers of the atmosphere causing disturbances that reflect radio signals. As a consequence, short-wave radio signals can be interrupted and, in rare cases, strong radio bursts associated with solar flares can introduce noise in the wireless communication systems [90]. Another case is the one of *solar energetic particles (SEP)*. These can be ejected from the Sun with very high velocities, accelerate in the corona and reach the Earth environment in 1-2 hours with high energies. SEP originate from shock-waves associated with CMEs or from the solar flares [26]. They can cause harm to astronauts in outer space or damage spacecrafts and cause computer errors. Then, there are the *Coronal Mass Ejections (CMEs)*, which are huge clouds of magnetized plasma ejected periodically from the Sun at high speeds, namely over 3000 km/s [150], and contain $\sim 10^{12}\ kg$ of material. It takes from around 15 hours to a couple of days for a CME to reach the Earth environment [55]. If a CMEs erupts in the direction of the Earth, it can cause a big geoeffective storm, provoking increased radiation exposure for airline crews and passengers, destroying the satellites and navigation systems on Earth. Lastly, *shocks in the solar wind* take a few days to reach the Earth, too. Then, they hit the Earth's magnetosphere, causing magnetic storms. The huge changes in the Earth magnetic field can even cause the increase of current in long metal structures (pipelines and power lines). Besides, the solar wind may heat and squeeze the magnetic shield, causing satellites at high altitudes to move outside the shield and being hit by charged particles. On a more pictoresque note, geomagnetic storms are the origin of polar aurora: the charged particles precipitate into the upper atmosphere and cause the familiar greenish or pink rays (which usually are the signatures of the excited oxygen and nitrogen atoms, respectively) at polar latitudes.

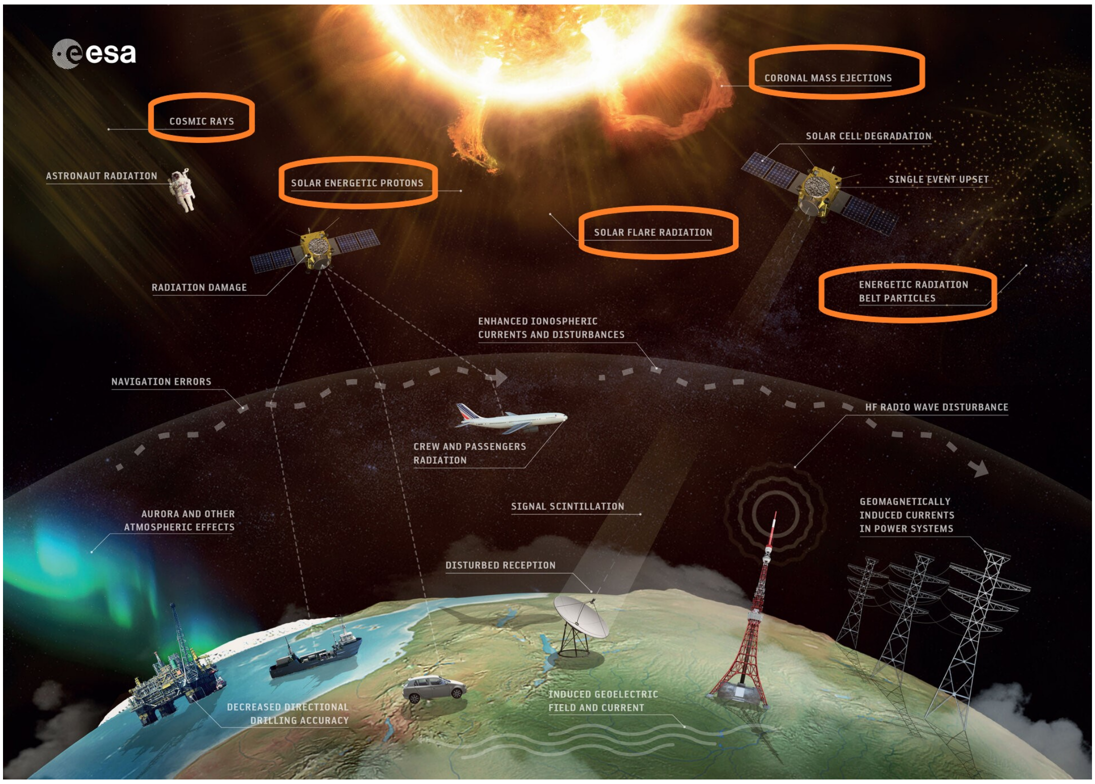

Figure 1.9: Space Weather effects on human technologies. In the orange boxes are different Space Weather phenomena. Non-solar sources such as Galactic Cosmic Rays (GCR) are considered to be a Space Weather element since they can alter space environment conditions near the Earth. Under the right circumstances energy and momentum can be transferred into the terrestrial system, despite Earth's magnetic field protection: the near-earth environment can become disturbed with the effects felt on a global scale. *Courtesy of ESA-Science Office.*

Since the amount of solar activity follows the solar cycle described in Chap. 1.1.3, the number of solar disturbances that impact Earth also follows this cycle. In a way, it can be said that space weather has "seasons", with solar maximum indicating a strong likelihood of severe space weather with possibly harmful consequences, while solar minimum indicates predominantly quiet space weather. Although space weather disturbances could pose a threat to human activities, during this period the amount of cosmic rays hitting Earth is lower. Somehow, the enhanced solar magnetism keeps our planet safe.

In the last century, human technology and their importance in everyday life have advanced remarkably. This makes us more vulnerable to the solar activity: in this era of satellites and global communication, airplanes, electrical power and space travel, all these activities can be affected by the above listed solar eruptive phenomena (see e.g. [46]). Therefore, understanding and forecasting hazards posed by the solar active events has grown in importance for the modern human civilization. Nowadays the impacts of Space Weather on the infrastructure of the global economy are recognized by the society in general.

Usually, the most famous example of large-scale space weather event on Earth is the Carrington event of September 1859 (see [63] for more details). Richard Carrington observed a blinding flash of light which actually was a huge Earth-directed CME. Approximately 17 hours later, polar auroras were so strong they were clearly observed not only at higher latitudes but also throughout the Caribbean, Mexico, Hawaii, southern Japan, southern China, and as far south as Colombia (near the equator in South America) and as far north as Queensland (Australia, near the equator in the Southern Hemisphere). Not only this, but telegraph systems across Europe and North America stopped functioning. In some cases, telegraphs provided electric shocks to operators; in other cases, their lines sparked in populated areas and some even started fires [51]. This type of CMEs is now defined as Carrington-class events and are estimated to occur on average once every several millenial. What would happen if an event of a similar scale were to occur in the present time? How strong would the impact be on space-borne and on-ground technologies?

Even without considering such an extreme case, there are several examples of milder events affecting the correct functioning of industrial devices and instrumentation. For instance, on August 4, 1972 an instantaneous, unintended detonation of dozens of long-forgotten sea mines south of Hai Phong (North Vietnam) was caused by strong eruptive phenomena on the Sun [83].

More recently, Elon Musk's SpaceX declared (on February 8, 2022) that 40 out of the 49 newly launched Starlink satellites were lost because of a geomagnetic storm caused by a solar outburst. This storm determined an increase of air drag which forced the satellites to an uncontrolled and non-programmed reentry into Earth's atmosphere [53].

It is evident how the space weather information and services are required to rapidly grow [30] and become more and more accurate. For this reason, a new generation of space-based instruments appeared, broadening the knowledge of the processes involved near the Sun, in interplanetary space, and in the near-Earth environment [84].

1.2. Coronal Mass Ejections

1.2.1. An overview of CMEs

Coronal Mass Ejections (CMEs) and solar flares are the most violent eruptive processes on the Sun. CMEs are qualified as the main drivers of space weather effects, indeed they induce the majority of troublesome effects on space-borne and ground-based technologies. They are worthy of attention from a technological point of view, but are very interesting from a scientific viewpoint, too. The connection of CMEs to disturbances in the solar wind, affecting planetary magnetospheres, comets and cosmic rays, provides further motivation for research and extends their significance well beyond the traditional area of solar physics knowledge. Moreover, the possibility of analogues to CMEs on other stars and their interplanetary effects suggests a potential scheme extending well beyond the solar system.

CMEs are huge clouds of magnetized plasma, expelled from the Sun into interplanetary space with speeds in the range of some 100 km/s up to $>$3000 km/s [157]. They inject large quantities of mass (billions of tons of coronal material) and magnetic flux (they carry an embedded magnetic field that is stronger than the background solar wind IMF) into the heliosphere and cause major transient disturbances. They are the largest-scale eruptive phenomenon in the solar system: they originate from coronal-loop-sized scale ($\sim 10^4\ km$), then expand and cover a significant part of the solar surface, and extend thoroughly from the low corona to the interplanetary space [19]. CMEs with velocity higher than 1000 km/s (fast CMEs) may create shock waves in front of them when propagating away from the Sun: the background solar wind moves on average 400 km/s and its sound speed is $\sim 40\ km/s$. Therefore, if a CME has a speed greater than this value, a shock wave forms. Shock waves in interplanetary space are very good particle accelerators and the large amounts of energetic particles generated by fast-CME-induced shocks can cause damage to satellites, as the CME moves across the slower solar wind [100].

Coronal Mass Ejections occur in regions of the Sun dominated by the strong magnetic field, i.e active regions (ARs). Different observations indicate that CMEs can be observed in different wavelenghts, such as soft X-rays (SXR), extreme ultra-violet (EUV), radio and others [68]. Despite their scientific and technological value, in most cases they are challenging to be studied because of the complexity of forms and projection effects. In order to study them, coronagraphs (also known as white light telescopes) are used, which block the photospheric white light from the disk. Over the past decade several space missions (namely, SOHO, TRACE, Wind, ACE, STEREO, and SDO spacecrafts) along with ground-based instruments have provided data sets that helped in understanding the origins and development of CMEs at the Sun and their role for Space Weather affecting Earth. SOHO (launched in 1995) has been providing an almost continuous coverage of the

solar corona and until now has worked for almost two solar cycles. The SOHO/LASCO coronagraphs routinely observe CMEs launched along the Sun-Earth line as halo-like features. The heliospheric imagers SMEI (2003–2011 on the Coriolis spacecraft) and the HIs (since early 2007, part of the SECCHI instrument on-board STEREO) managed to image and track CMEs continually across the inner heliosphere. STEREO also permits observing Earth-directed CMEs from different viewpoints of increasing azimuthal separation, thereby enabling the estimation of their three-dimensional properties [157].
With the continuous observations from various ground-based and space-born coronagraphs, more than ten thousand CME events have been recorded. This enables the statistical investigation of their properties. It is important to note that CME observations suffer from projection effects: CMEs are 3D structures originating from the optically-thin corona which are imaged by coronographs in two dimensions, that is, they are projected onto the image plan (the plane of the sky, that is the plane orthogonal to the Sun-Earth line) [18]. This introduces distortions in their appearance and complicates the determination of their properties.

Properties of CMEs

For CMEs' analysis, different properties are measured, including their occuring rates, location, angular widths, speed and acceleration, energy and masses [157]. Since 2008, the first CME database, created thanks to the LASCO instruments' acquisitions, is constantly being updated. This marked the start of studying the solar cycle dependence of CME properties by using only one instrument [56]. However, acquisition and estimation of parameters such as mass and energy are limited by the observation methods and the projection effects so the following discussions about theories, procedures and calibrations for the analysis become complicated. Below is a list of some important parameters for the CMEs analysis.

- *Occurrence rate*
  The frequency of occurrence of the observed CMEs tends to follow the solar cycle, i.e the sunspot number [121]. However, different instruments and software entail a difference in the values of occurrence rate. For instance, the CME catalog in the CDAW data center (NASA) shows that the occurrence rate is around 0.5 per day near solar minimum and around 6 near solar maximum (this result is based on the observation of more than 13 000 CMEs during the solar cycle 23). On the contrary, using the automated software CACTus [120] for CMEs detection during the same observational period, the estimated occurence rate is about 2 per day during the solar minimum, increasing to ~ 8 per day near solar maximum.

- *Angular width*

  Two types of CME are distinguished based on the angular width : "narrow CME" for width less than $\sim 20°$ and "normal CME" for other angles. This distinction is correlated to the progenitor structure that later erupsts as a CME. For narrow CMEs, the originating structure is thought to be the open magnetic field, typically the coronal hole. For normal CMEs (from now on, "CMEs" will refer to normal CMEs, unless differently specified), the origin of the eruption should be a strongly twisted or sheared magnetic structure, that has stored a huge amount of non-potential energy. This structure should have a potential to erupt while being kept in a metastable equilibrium or being close to a nonequilibrium state, likely by the line-tying effect at the footpoints and the closed magnetic field above, which typically consists of active regions and bipolar magnetic field extending over quiescent filaments. As mentioned before, CMEs are strongly associated with eruptive filaments [157].

  It is important to specify that the so-called halo CMEs look like they extend close to 360° when observed (hence the name "halo"), but their real angular width can be very narrow: they are narrow or normal CMEs that propagate close to the Sun-Earth line, either towards or away from the Earth. They are a perfect example of how CMEs analysis can be very complicated when using only a single point of observation.

- *Mass*

  In general, the mass of a CME falls in the range of $10^{11} - 4 \cdot 10^{13}$ kg, averaged at $3 \cdot 10^{12}$ kg ([70], [147], [148]). The value of the mass can be computed with the knowledge of Thomson-scattering nature of intensity observed from coronagraphs. However, all the measurements and estimations made in the literature make the assumption that all the CME parts are located in the plane of sky [157]. This implies that if the CME is exactly located on the solar limb, its mass can be properly estimated, and if not, it is underestimated.

- *Speed and energy*

  The CME velocity (projected in the plane of sky) ranges from around 20km/s to $>$ 2000 km/s, some events can reach 3500 km/s. The kinetic and potential energies are in general of the order of $10^{22} - 10^{25}$ J [40].

- *Acceleration*

  Statistical studies ([152], [11]) computed maximal accelerations values ranging from 10 to 1000 m/s^2 and mean values of about 800 m/s^2. The acceleration phase duration is proportional to the dimensions of the source region; i.e., compact CMEs are accelerated more impulsively [152]. The most powerful events have peak value of acceleration $> 5000\ m/s^2$ ([11], [152], [132]).

Morphology

CMEs may appear in many different shapes, but this variety is mainly attributed to projection effects [126]. Nonetheless, there is a standard model of the structure of normal CMEs, identified by coronagraphic observations, since they are known to be associated with eruptive filaments. Knowing that some active region filaments and almost all quiescent filaments are generally well described by the flux rope model [89], it is often assumed that the flux rope system is the ideal model for the progenitor of CMEs, that is, a magnetic configuration of twisted field lines in a less-sheared magnetic system [19]. This model is based on three parts: a bright front, a dark cavity and a bright core ([75] [61]). Fig.1.10 shows an example of the three-part model for a normal CME.

- The *bright front* of the flux rope moves away from the Sun. It is interpreted as outward moving density structures.
- The *cavity* is dark, since inside the flux rope the gas pressure and density are lower, due to additional magnetic pressure.
- The *bright core* is the innermost part of the flux rope and corresponds to the erupting filament [66], where dense prominence material is supported against gravity by the upward Lorentz force at the dips.

Despite having this three-part standard model for morphology of CMEs, observations show that only $\sim 30\%$ of CMEs fall in the category of having all three parts [154]. Because of thermal instability some events do not form a filament in the pre-event structure or might not even be related to filaments at all [19].

As already hinted in Chap.1.2.1, only 2D projection of CME on the sky plane are observed when using a single viewpoint. This has created a huge challenge for a long time in the determination of the CME 3D structure. Finally, the NASA STEREO mission with its unique capability of imaging the inner heliosphere from two points has greatly improved the understanding of CME structure and evolution [136].

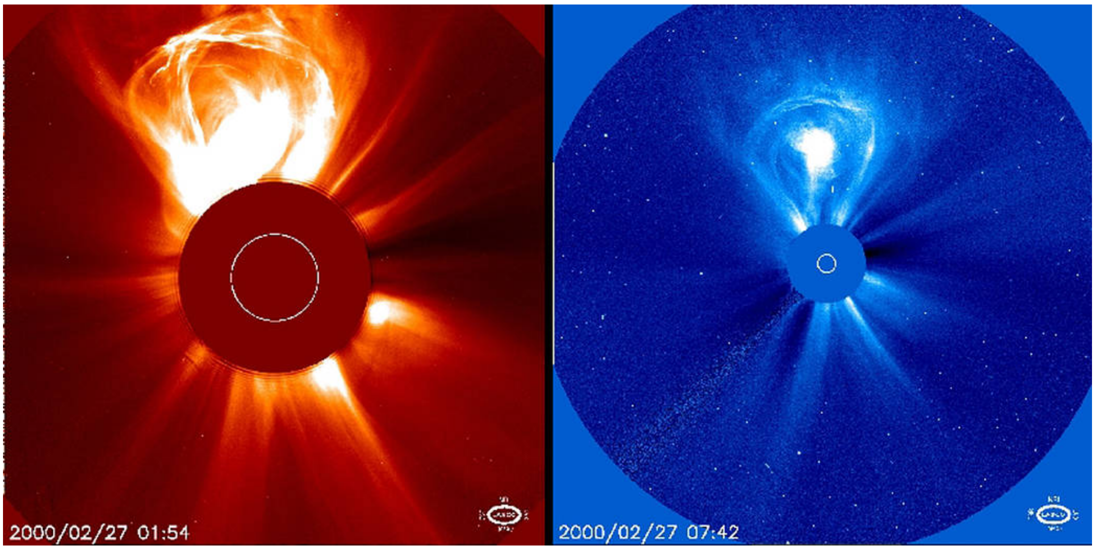

Figure 1.10: A coronal mass ejection on February 27, 2000 taken by SOHO/LASCO C2 (*left*) and C3 (*right*). The coronograph is blocking the light coming from the solar disk: the opaque circle is the occulting disk and the white circle at the center represents the solar disk. The CME looks like a light bulb, in fact this image is an example of the standard three-part model: it is possible to distinguish a bright front that moves away from the Sun, followed by a dark cavity with an embedded bright core. *Courtesy of SOHO ESA and NASA.*

1.2.2. Associated Phenomena

In general, CME are observed with coronographs and nowadays LASCO, STEREO and SDO satellites are used. One of the upcoming problems is related to the limited lifetime of instruments, e.g. already data from the STEREO-B satellite has been lost since 2014. No future instruments are planned to be launched until 2024, so observation capabilities are limited. Even with coronagraphic observations, it is impossible to study the early evolution of Earth-directed CME (halo events), which are the main drivers of Space Weather phenomena, seeing that they affect the Earth environment the most. Despite their damaging potential, they have the least level of measurements accuracy due to strong projection effects. Moreover, coronagraphic observations contain no information on the initial propagation and acceleration phase of CMEs because the occulting disk blocks out the low corona. Thus, while direct observation with the coronagraphs is the most suitable type of observation, it is also related to large uncertainties. For this reason, different phenomena associated to CMEs but occurring lower in the solar atmosphere can be observed, including filament eruptions, flares, post-eruptive arcades, large-scale coronal EUV waves, and coronal dimmings. [68]. The main help obtained from the observation of these associated activity in the low corona is to distinguish whether a halo CME was launched from the front or backside of the Sun with respect to the observer's point of view. Furthermore, studying the evolution of these associated phenomena can provide additional information about the early stages of CME evolution and can help in the prediction of their behaviour and characteristic parameters.

Solar Flares

Flares are sudden localized enhancements of electromagnetic radiation (radio, visible, UV, X-rays) that occur in Active Regions. Their occurrence rate varies along with the solar cycle.

CMEs are usually accompanied with flares as they are caused by the same magnetic processes in the Sun [61] and several studies showed how statistically the most powerful CMEs are associated with powerful flares [57]. Observations also confirm that there is a close relationship between the energy release of the flare and the dynamics of the associated CME. However, there is no one-to-one correspondence between CMEs and flares. Several CMEs are associated with solar flares but many others are not, and vice versa.

CME parameters, such as the velocity, the acceleration or the kinetic energy are strongly correlated with the SXR peak flux that indicates the flare strength, or with the integrated flux of the associated flare, the flare fluence ([151], [133]).

Scientists have developed a simple rating system for this solar x-ray activity based on the detection of X-rays thanks to the X-Ray Sensor (XRS) instrument [41] onboard GOES satellites [37]. They have created five levels (A, B, C, M, and X) based on a logarithmic scale, increasing from A to X as a power of 10. Thus, an X event is 10 000 times stronger than an A event. In addition, each level can be further divided from 1.0 to 9.9, which means it is possible to have a C2.3 event, or a B7.9 or an M6.5. SWPC sends out space weather alerts at the M5 ($5 \cdot 10^{-5}\ W/m^2$) level.

Accordingly, the GOES X-ray plots are used to track solar activity and solar flares: the GOES X-ray flux 6-hour and 3-day plots contain 1 and 5 minute averages, respectively, of solar X-rays in the 1-8 Angstrom (0.1-0.8 nm) and 0.5-4.0 Angstrom (0.05-0.4 nm) passbands. The typical values to categorize each flare event according to its amount of peak flux are shown in Tab.1.3.

Classification	Approximate peak flux range at $0.1 - 0.8$ *nanometre* (W/m^2)
A	$< 10^{-7}$
B	$10^{-7} - 10^{-6}$
C	$10^{-6} - 10^{-5}$
M	$10^{-5} - 10^{-4}$
X	$> 10^{-4}$

Table 1.3: Range of peak flux corresponding to each flare category.

Filaments and Prominences

Prominences are cooler material prolonged along the magnetic field lines, which can be observed in EUV and Hα wavelengths near the limb, where the material is brighter than the surrounding corona. If a prominence is viewed from a different perspective so that it is observed against the solar disk, it appears darker than the surrounding background and is called solar filament [49]. The disappearance of a filament or the eruption of a prominence are often seen in association with CMEs [71]. Part of this material is known to form the core of a three-part CME [149].

EUV Waves

EUV waves are global wave-like disturbances observed on the Sun, characterized by brightness fronts propagating away from eruptive active regions in the extreme ultraviolet (EUV) ([101], [138]). They typically propagate with speeds of several hundred kilometers per second (typical range around 200–400 km/s, but also they can reach 1000 km/s) ([104], [102], [137]). There has been and there still is a controversy over the wave nature of the EUV waves, emerging from the difficulties related to the physical interpretation of their complex behavior. Their nature cannot be satisfactorily explained by either the wave or the pseudo-wave theory ([48], [110], [153]). However, there is one last mechanism used for their explanation, which is the most accepted interpretation thanks to the newest high spatio-temporal observations (SDO/AIA). It is the "hybrid" interpretation that combines the previous two theories and attributes one slow pseudo-wave and one fast EUV-wave component to the observations ([20], [162], [21], [38], [129], [128], [88], [31]).

Because of the strong association of EUV waves to CMEs and other similar expanding drivers, these events where misidentified as the same in literature. This is because both structures may appear as a wave front in the images, but actually their behavior (and interpretation) will be different (see [110] for an accurate discussion of the problem). Due to the dual nature of CMEs and EUV waves, the scientific community proposes a set of

definitions: an EUV wave is a disturbance propagating along the EUV coronal surface at large distances from an eruption. On the other hand, a CME is a magnetic disturbance (i.e. a magnetic fluxrope) propagating outwards from the corona.
Multi-viewpoint observations using the STEREO spacecrafts or combinations of STEREO with SOHO or SDO can provide important geometrical characteristics of EUV waves as well as their associated CME in the 3D space including their lateral extensions ([12], [134], [114]).

Coronal Dimmings: introduction

Lastly, the most distinct phenomena associated with CMEs: coronal dimmings. They are localized regions of reduced emission in the EUV and SXR low in the corona and are interpreted as density depletions due to mass loss or rapid expansion of the overlying corona during the CME lift off [22]. Chapter 2 will describe in details the nature of solar coronal dimmings and their association with CMEs. It will also present the different methods used until now for their detection as well as provide an overview of the works that investigated the recovery process of coronal dimmings. Chapter 3 will present new algorithms for the analysis of dimming observed for long periods.

2 | Coronal Dimmings

2.1. An overview of Coronal Dimmings

Coronal dimmings, or transient coronal holes (TCHs), are localized transient regions of strongly reduced emission in SXR and EUV that occur in association with CMEs in the low corona [79]. They are generally interpreted as density depletions caused by mass loss during the CME eruption [131]. Their locations are sometimes considered to appear at the footpoints of the erupting flux rope. For this reason, they are considered as reliable indicators of halo CMEs, which are difficult to characterize with white light coronagraphs. Some CMEs are observed also without dimmings, and it was noticed that all non-dimming CMEs have speeds lower than 800 km/s, which hints at a more intimate connection between the CME and the dimming [119].

Dimmings appear quite suddenly, on a scale of minutes, and their lifetime varies from 3 to 19 hours. It is considered rare for them to persist longer than a day (see [118] for results of a statistical analysis), but there exist exceptions where there is no recovery at all (e.g.[7]).

2.1.1. Formation and morphology

There are two generally accepted mechanisms of dimming formation ([9], [97]):

1. *Mass-loss dimming.*
   The reduction of intensity in the lower corona is caused by plasma being ejected as part of the outward moving CME and due to the expansion of the CME structure in interplanetary space [9]. The larger the volume of expansion, the more the plasma density is decreased. This type of dimming is observed as a simultaneous decrease in multiple EUV emission lines. Fig. 2.1 shows schematically the process of mass loss works.

2. *Temperature dimming.*
   The drop in intensity could be also caused by a change in temperature [23]: plasma is heated or cooled, so the ionization fraction changes, and so does the intensity

of the emission. This type of dimmings can be misinterpreted as mass loss if only one spectral line is observed but multi-wavelength observations of dimming regions indicate that the drop in emission in one wavelength is not supplied by an increase in another wavelength, and often all observable wavelengths have a co-temporal plunge in emission [62]. Thus, temperature variations cannot account for all, or at least most, of the darkening that is detected. Furthermore, it has been showed that the timescale of the dimming formation observed in Yohkoh/SXT data is faster compared to the corresponding time for conductive and radiative cooling. This suggests that the dimmings are primarily caused by a density depletion rather than by temperature change [69].

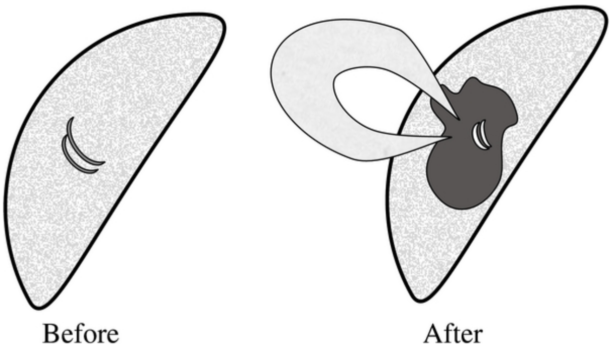

Figure 2.1: Schematic representation of the formation of a mass-loss dimming. Before the eruption (*left*), coronal loops can be considered almost quiescent. During and after the eruption (*right*), the loops become more and more bright and reconfigured, a CME is ejected, and a sort of void forms in the coronal plasma. *Courtesy of [97]*

Currently, coronal dimmings are differentiated into two types in literature:

- *core dimmings*
  Core dimming regions are stationary and localized regions; they usually occur in pairs and are rooted in opposite magnetic polarity regions, close to the eruption site. In simple configurations, they are believed to mark the footpoints of the erupting flux rope. ([131], [156]).

- *secondary dimmings*
  These are more shallow and diffuse and can extend to significant distances from the eruption site: they can develop in all directions, either in symmetrical or in narrow extended structures. They are believed to be caused by the expansion of the overall CME structure and so they are believed to correspond to the spatial extension of the corresponding CME in coronograph data [95].

It is important to note that in the case of off-limb observations it is not possible to distinguish the two types of dimmings from one another.

2.1.2. Relationship to CMEs

Several properties derived from the study of dimmings can be used to obtain information about the associated CME:

1. The mass of CME can be retrieved by information about the volume of the dimming and by calculation of the emission measure to estimate the amount of ejected plasma ([94], [93], [4]).
2. The angular extent of a CME associated to a dimming can be investigated thanks to information on the spatial extent of the coronal dimmings itself ([139], [9]). At the same time, the CME extension correlates with the CME mass [36].
3. Properties of the Magnetic Cloud (MC), i.e. interplanetary flux rope structure, at 1 AU can be related to the coronal dimming, since it is believed to mark the footpoints of the erupting flux rope [95].
4. It is possible to retrieve information about the early stages of CME by analysing the corresponding coronal dimmings (e.g., [116]) and information about the CME post-eruption by studying the dimming long-term evolution, namely investigating their recovery phase (e.g., [7]).
5. It is possible to better understand the interaction of CMEs with their surroundings during the early evolution phase by studying the dimmings distribution in space, their formation and the measurement of their magnetic flux contribution to the associated CME [95].

2.2. Background and Literature Review

Coronal dimmings were observed for the first time in the 1970s thanks to data from Skylab and were called "transitional coronal holes" (TCHs) because of their decreased emission similar to coronal holes (CH) and their short life compared to typical CHs [123]. Later the observations using the Yohkoh Soft X-ray Telescope [85] permitted a better understanding of the dimming source in the inner corona and of their timescales.

Studies based on the Extreme-ultraviolet Imaging Telescope (EIT) mounted on-board SOHO (Domingo et al. [1995]) lead to the association with the CMEs and established that extreme ultraviolet (EUV) dimmings are a reliable indicator of the apparent footpoint of the white light CME [139]. It was thanks to the high-cadence imaging data, collected through seven different EUV filters, from the AIA (Atmospheric Imaging Assembly) [91] instrument on-board SDO that the analysis of plasma properties in coronal dimming regions using Differential Emission Measure (DEM) started [143]. In addition, different observations and spectroscopic studies (e.g. [60]) supported the theory of the mass-loss nature of dimmings. In the past few years, studies have demonstrated a correlation between dimming parameters and CME parameters with statistical analysis (e.g. [36], [24]).

2.2.1. Detection Algorithms and Dimmings Analysis

There are several factors that may hinder the dimming analysis, namely they vary much in their appearance or there may be other physical processes that could be misinterpreted as dimmings. Since the analysis is not trivial, new methods for dimming detection and extraction of significant parameters are continuously developed by the scientific community. Among these, the automated algorithms are of particular interesting. Some of the works, in chronological order, that made use of and suggested new approaches by using automated algorithms will be briefly presented below.

- *NEMO algorithm - Podladchikova and Berghmans (2005)* [113]
  The Novel EIT wave Machine Observing (NEMO) algorithm was created as a tool for detection of coronal dimmings and EIT waves. It is implemented for on-disk measurements using SOHO/EIT data. After the detection of the desired phenomena, its working principle relies on the analysis of statistical properties (e.g. dimming coordinates, dynamics of shape changes, area and direction of propagation, integral decrease of intensity) and on the understanding of the physics behind eruptive events.
  To better observe the changes in intensity two types of images are computed: running difference (RD) images are the result of the difference between the current image and the previous one, and base difference (BD) images are computed by subtracting a fixed reference image, that is an image taken before the event, from each subsequent image. Then, in order to detect and extract the dimming region, two masks are created: one contains pixels that decreased in intensity below a weak (i.e., quite high) threshold (maximal pixel map), while the other consists of seed pixels, representing the darkest pixels of the image (minimal pixel map). The final dimming region is formed by using the seed pixels for a region growing method and keeping the condition of a simply-connected region within the boundaries of the maximal pixel map. The method works with the assumption that dimmings are

simply connected areas, and their area is much larger than other areas of reduced intensity (which can be interpreted as noise). This detection algorithm is difficult to be applied for events without EUV waves.

- *Bewsher, Harrison and Brown (2008)* [14]
  In this statistical study, the authors detected dimmings at the solar limb using spectroscopic data: the Fe XVI and Mg IX spectral lines, which represent temperatures of $1 \cdot 10^6\ K$ and $2 \cdot 10^6\ K$ respectively, were used for coronal dimmings investigation. Mosaic images to trace the images are produced, then the Base–difference (BD) images were obtained for each dataset of mosaics by subtracting a pre-event frame from each event image. If the BD intensity value of a given pixel is greater than twice the statistical error of each pixel computed with the equations in [140], then the pixel is noted as dimmed and the pixels in the neighboring space and time are examined, until the extent of a given dimming is established. The spatial extent of the dimming is limited by a minimum group size of one hundredth of the dimming mosaic area. The CME-dimming association could be confirmed by showing that up to 55% of the dimming events were associated with CMEs and up to 84% of CMEs in the data set could be tracked back to dimmings.

- *Reinard and Biesecker(2008)* [118]
  A statistical analysis of 96 CME-associated EUV coronal dimmings between 1998 and 2000 was performed. For the analysis, the SolarSoft library [47], available in the IDL programming language, is used. By creating base-difference (BD) images, the sub-regions of each dimming location are selected by hand in a way to include the dimming region at its maximal extension, managing to partially leave out the unnecessary non-dimming-related portions of space, for example the overwhelming bright flare pixels. Then a thresholding algorithm is applied: pixels are flagged as dimmed if their intensity is below the threshold. The detection method allows to derive dimming location and their area and brightness for the next steps in the analysis. As a result, it was noted that coronal dimmings are likely to occur near active regions and typically have a rapid decrease in emission followed by a more gradual recovery. In addition, even though CME can be observed without dimmings, all fast CMEs imply the observation of dimmings. Another result was the estimation of the mean lifetime of the dimmings around 8 hours (see Chap.2.2.2 for more details).

- *Attrill and Wills-Davey (2010)* [9]
  The method was developed using the NEMO algorithm as a basis, but implementing the detection process with running-difference (RD) images and the thresholding

level indicated by [118]. The used programming language was IDL [13]. NEMO calculates statistical properties of the RD images, but producing this type of images is expensive in terms of computational time (each image has to be de-rotated to the reference image before subtracting the previous image from the current one). Hence, the authors also investigated the possibility of running the detection algorithm directly on original intensity images, with the ultimate goal of running real-time detection with AIA data. In the end, they managed to detect the occurrence of a coronal dimming event by using this technique. The method could also be implemented for off-limb dimming detection.

- *Mason, Woods et al. (2014, 2016)* [98]
  This work goes through the description of different physical processes that could be interpreted as dimmings and proceeds with a spectroscopic analysis of mass-loss coronal dimmings, identified from spatially unresolved full-disk irradiance light curves acquired by the EVE instrument [159] on-board SDO. The technique, which was described in [97], was applied to 37 dimming events that appeared during two separate two-week periods in 2011.
  According to the authors, observing just one single dimming spectral line is insufficient to have a reliable prediction of a CME occurrence. Rather, they suggest to observe spectral lines from a wide span of an ionization sequence, including both dimming and non-dimming lines, since this allows the removal of the gradual phase peak in the EVE dimming time series. First, they temporally align the peak in the non-dimming line with the same in the dimming line, then they scale the non-dimming peak down to match the dimming peak intensity and lastly they subtract the re-normalized non-dimming time series from the dimming series. This method deals only with percentage changes, and this is a positive aspect because it does not imply a direct irradiance alteration.

- *CoDit - Krista and Reinard (2017)* [87]
  The authors performed a statistical study of 154 dimmings with the associated flares and CMEs occurred throughout 2013 and analyzed their physical and morphological properties. Each dimming in the catalog was processed with the semi-automated Coronal Dimming Tracker (CoDiT) using SDO/AIA 193Å observations and HMI magnetograms. They used a new coronal hole detection algorithm to detect transient dark regions "directly" in extreme ultraviolet (EUV) images instead of the typical use of BD images. Indeed, BD images showed large and diffuse dimmings that represent the projected view of the rising, expanding plasma; on the other hand, the new method allowed to study dimmings as the footpoints of CMEs. A

comparison of the physical properties of dimmings, flares, and CMEs lead to the discovery of different relationships, namely that larger dimmings have a longer lifetime (it takes more time to "close down" large open magnetic regions) and that the EUV intensity of dimmings correlates with how much plasma was removed and how energetic the eruption was.

It is important to note that the above mentioned work laid the basis in understanding the relationship between dimmings and their associated CMEs. However, most of them are case studies. A statistical work is needed to prove any correlation between dimming parameters and CME mass. Hence, the last work here presented is the first to make a comprehensive statistical analysis of coronal dimmings and their associated CMEs, later followed by other works (e.g., [24]). The current thesis relies on this work methodology for the initial implementation of the detection algorithm.

- *Dissauer, Veronig, Temmer et al. (2018a, 2018b, 2019)* ([34], [35], [36])
  In order to detect coronal dimming regions, a thresholding technique is applied on logarithmic base-ratio (LBR) images (for details see Chap.3.2.2): a pixel is flagged as a dimming pixel if its logarithmic (log10) base-ratio intensity decreased below $-0.19\ DN$. As a next step, morphological operators (IDL routines *dilute.pro* and *erode.pro*) are used to smooth the extracted regions, namely to remove small features due to noise and to fill small holes and gaps. This procedure enables the identification of seed pixels for a region growing algorithm (IDL routine *region_grow.pro*). Lastly, the final dimming region is extracted from the detected pixels that are connected neighbors to the seed pixels [34]. With this method, the detected coronal dimming region is a combination of the footpoints (core dimmings) and of the expanding CME body (secondary dimmings).
  The extraction of characteristic dimming parameters is performed through the cumulative sum of dimming pixels over time; this permits to describe the dynamics, morphology, magnetic properties, and the brightness of the dimming regions. It was shown in this work that coronal dimmings are flux balanced, i.e. the same amount of positive and negative magnetic flux within the uncertainties that core dimming regions are a subset of the overall identified dimming region [35]. The method was successfully applied to 62 dimming events [36], where dimmings were observed on-disk by SDO/AIA and HMI, and the early propagation of CMEs was studied close to the limb with STEREO/EUVI and COR, to minimize projection effects. The dimming area, its total unsigned magnetic flux and its total brightness reflect properties of the total dimming region at its final extent and can be called first-order coronal dimming parameters. The CME mass shows the strongest corre-

lations (c$\sim 0.6-0.7$) with these parameters, while the maximal speed of the CME is strongly correlated with second-order dimming parameters, i.e. the time derivative of the first-order dimming parameters such as the total magnetic flux rate and the area growth rate.

2.2.2. Dimming recovery

Dimmings have been indicated as a reliable indicator of Earth-directed CMEs. By assuming that the CME is rooted in the dimming, the study about dimmings could provide information about the early stages of a CME eruption and some relevant CME properties. Not only this, but the study of the dimmings lifetime, especially during their recovery phase, could be used to obtain information about the evolution of the CME post-eruption [6]. The need to understand how the dimming are related to the CMEs while they expand out into the interplanetary space is at the basis of the works presented below, which mostly focus on the dimming recovery phase.

- *Kahler and Hudson (2001)* [79]
  The authors analyze 19 transient coronal holes (TCH) events, associated with halo CMEs, over 9 years from Yohkoh Soft X-ray Telescope (SXT) observations with the aim of analyzing the changes in TCH boundaries. The chosen events include magnetic configuration recognized in the form of either active region (AR) or neutral line (NL). They investigate the possibility that TCH are the footpoints of the flux ropes detected as magnetic clouds (MC) at 1 AU (as suggested by [131], [155] [156]). Since the boundaries of a TCH are never static, they could be indicative of the reconnection process. Hence, the TCH shapes and sizes would reflect the solar magnetic connectivity between the imbedded coronal fields and the flux rope fields detected at 1 AU: the disconnection regions of the MC could be associated to regions of the TCH that have already closed. Even if there were no correspondence between TCHs and MCs, the authors consider two extreme cases that could explain how TCH disappear:

    - they could shrink inwards from their boundaries (with no internal brightening), which implies absence of magnetic reconnection along the internal field lines.

    - they could begin to brighten internally, which implies a reconnection occurring along the internal field lines.

  As a result, they found that dimming lifetime ranges from 5 to 66 hours, but by taking into account some possible errors due to foreshortening and obscuration by the foreground corona, they state that TCHs generally live for no more than 48 hours. Because of this identified lifetime, the authors disagree with the correlation of dimmings to flux ropes detected at 1 AU, since the dimming lifetime is in any case shorter than the 3- to 5-day interval needed for a MC to reach Earth. They suggest a complete disconnection between the TCH and the MCs. Lastly, they observed that all the events in the study disappeared because of shrinking from the external boundaries inwards.

- *Attrill, van Driel-Gesztelyi, Démoulin et al. (2008)* [7]
  The goal of the authors is to understand the mechanism behind coronal dimming disappearance before the associated MC reaches 1 AU. To do so, they analyze the evolution and the recovery in intensity of three dimming events, observed with the SOHO/EUV Imaging Telescope (EIT) in 193 Å, for approximately two days. This time range is due to the appearance of brightening/darkening effects due to the de-rotation of the images. They use BD images and identify a longest-lived part within the dimming, the "core". They observe that dimmings shrink in their spatial extent in a fragmentary and inhomogeneous manner, as suggested by [79]. However, the authors of this paper also notice a progressive increase of intensity within the dimmings and consider that Yohkoh/SXT could have not detected this behaviour because of the lack of power, during the recovery process, to heat the plasma to temperatures high enough for detection. In the end, the identified core regions have not recovered by the end of the time series, but the average intensity of the dimmings without the core has recovered to the pre-eruption level. Fig.2.2 shows the behaviour of the dimming regions for one of the analyzed cases. By assuming that the recovery gradient stays the same and by performing a least-square linear fit to the recovery segment of the obtained light curves, an estimation of the time at which the corona should recover to its pre-event intensity level is done. However, the timing of the dimming recovery and of the MC arrival at 1 AU do not coincide: in two out of the three cases, the estimated time of departure from the Sun of the electron stream detected at 1 AU is not the same as the estimated time of the core dimming recovery. This leads to two possible options: either dimmings are actually not the source region of the MC [79] or the relationship between the ICME/MC and the dimming is to be redefined in further studies to understand how the magnetic reconnectivity with the Sun is maintained.
  In conclusion, to explain the dimming recovery mechanism, they consider an interchange reconnection between the open magnetic field of the dimming and the small coronal loops or emerging flux bipoles that disperse the concentration of open magnetic field into the surrounding quiet Sun, rather than closing the global coro-

nal magnetic field. Bright loops at the boundary of the dimming or emerging flux could play a role in diminishing the dimming size and replenishing the flux from the inside, by bringing closed loops into the open magnetic field of the dimming. Internal recovery is hence expected to be slower than the process occurring at the periphery.

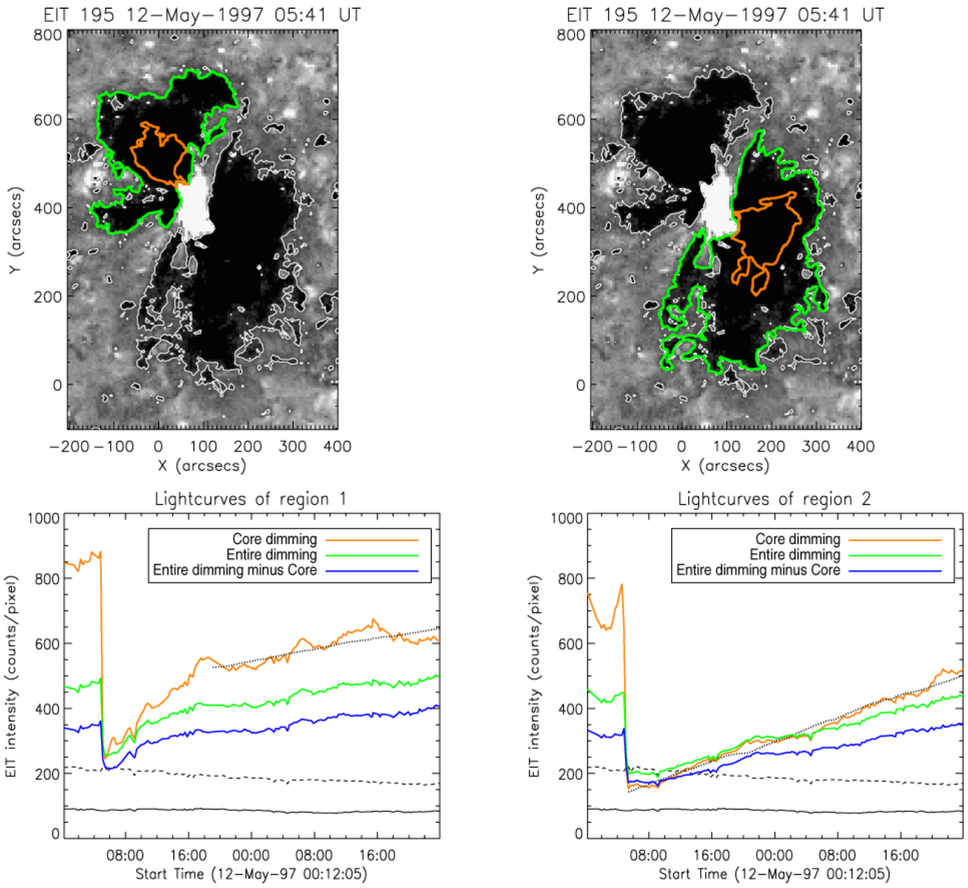

Figure 2.2: *Top*: BD images of 12 May, 1997 dimmings, marked by white contours. Green regions: full extent of the dimming. Orange regions: cores of each green region, i.e. dimmings still existing the end of the dataset. *Bottom*: light curves. Green light curves: average intensity of the entire dimming region. Orange light curves: average intensity of just the core dimming region. The overlaid black dotted line is the best fit calculated during the recovery phase. Blue light curves: average intensity of the the peripheral dimming (i.e., the full dimming, minus the core). Dashed line: intensity level in a region of quiet Sun. Solid line: intensity level in a pre-existing coronal hole (for comparison). *Courtesy of [7].*

- *Reinard and Biesecker(2008)* [118]
  The methodology used for this work in already described in Chap.2.2.1. This work is a statistical analysis of 96 dimming events associated to CMEs, over a period of three years in the rising phase of solar cycle 23. The authors use area (number of dimming pixels) and brightness (sum of intensity of dimming pixels) curves to observe the dimmings evolution in time. They define the rise time as the time between the beginning (two successive decreasing points for brightness and rising points for area) of the dimming and its peak value (i.e., maximum area); the recovery time is the time interval between the peak and the dimming end, that is a series of 3 successive flat points. The dimming durations range from 1 to 19 hours, with an average of 8 hours. The lifetime of the majority of the events varies from 3 to 12 hours, and the overall median is 7 hours. Overall, the rise time is shorter than the recovery time. In addition, dimmings do not recover to the pre-eruption value in most of the cases; this is indicated as a consequence of the darkenings caused by the de-rotation of the images to a fixed time to compensate for solar rotation. The authors observed that the recovery slope can have either a single slope or a two-part slope. The single slope was observed for $\sim 76\%$ of the brightness and $\sim 72\%$ of the area time series, while the remaining events show the two-steps decay (or rise, for area) behaviour. Generally, the slope during the rising segment of brightness is steeper than during the recovery period, in the case of single-component slope, whereas in the case of events with two-part decay, the first decay segment has a similar slope to the rise period, and is followed by a second, more gradual decay. As a conclusion, the two-part slope could indicate a faster inflow of plasma then followed by a slower inflow and this consideration could help in the analysis of the dimming recovery method: since the initial segment of the recovery time and the dimming rise slopes are similar in magnitude, there could be some similarity in how the plasma is removed and then initially restored.

- *Attrill, Harra, van Driel-Gesztelyi et al. (2010)* [8]
  This case study analyzes the evolution of two coronal dimmings, each associated with a flare/CME occurring one day after one another. Data from Hinode/EIS and SOHO/EIT are used to investigate the evolution and the recovery phase. The chosen events (13 and 14 December, 2006) have been previously studied and, despite the impossibility to identify the core dimmings because of the bright light from the flares/CMEs, the events are characterized by extended and well-observed secondary dimmings. The authors use base difference images, which are subjected to projection effects for long-period analysis, to obtain brightness curves and then observe the

original images, also in different wavelengths, to understand the physics behind the obtained data. The lightcurves provide the average intensity within four localized regions per event. Three of these are in areas of relatively high intensity, while the latter is indicative of the CH intensity level, as a CH is present nearby the AR and is characterized by dominantly "open" magnetic field lines. The selected regions show a gradual recovery process, with a substantial recovery within two hours from the dimming onset. The mechanism behind the dimming recovery seems to be due to an upflowing mass supply from beneath the dimming region, in accordance to [78], but the re-establishment of overlying coronal loops plays a major role in the process. Overall, the recovery process of the analyzed secondary dimmings is similar to the formation of AR flare ribbons and flare loops, but the footpoints are more scattered.

- *Vanninathan, Veronig, Dissauer et al. (2018)* [143]
  The authors perform six detailed case studies using Differential Emission Measure (DEM) analysis for the investigation of the plasma characteristics in the coronal dimming regions. They use 12 hours of Atmospheric Imaging Assembly (AIA) [91] observations with high cadence. The results suggest two types of the recovery behavior: the core dimming regions perform very sharp drop (up to 50-70%) of the intensity during the dimming appearance and remain the same low level of intensity for more than 10 hours, while the secondary dimming regions show more gradual decrease of intensity (10-45%) with a faster recovery, starting after 1-2 hours form the beginning. These observations are in agreement with the interpretation of the core dimming regions as the foot-points of the flux rope, connected to the Sun, and the secondary dimmings as the signatures of expanding coronal structures during CME evolution. The statistical study of the coronal dimmings off-limb from STEREO by [24] reports the similar bimodal distribution of the coronal dimming recovery.

3 Research procedure

3.1. Working environment

This section aims at providing an overview of the SDO mission [111] and of the STEREO mission [80], from which the data used for this work are acquired. Another type of data that is briefly described is the X-ray flux obtained by the GOES mission. Then, a portrait of the Sunpy library of the Python programming language is done. This library was used for the creation of algorithms for the data pre-processing and analysis. A comparison with IDL, the programming language used so far for the solar corona and, more specifically, dimming analysis, is also done.

3.1.1. The SDO mission

The Solar Dynamics Observatory (SDO) was launched on February 11, 2010. It is the first mission of the NASA's Living With a Star (LWS) Program, which aims at understanding the causes of solar variability and its impacts on Earth. SDO's special feature is that it studies the solar atmosphere on small scales of space and time in many wavelengths simultaneously. Its aim is to help understanding the Sun's variations that affect Earth and Near-Earth space by investigating how the solar magnetic field is generated and structured and how this stored magnetic energy is converted and released into the heliosphere in the form of the solar wind, energetic particles, and variations in the solar irradiance. This type of observation, based on small scales of space and time, may assist the development of predictive capability.

The spacecraft is 4.5 meters high and over 2 meters on each side, weighing a total of 3100 kg at launch (fuel included). It is a Sun-pointing semi-autonomous spacecraft that guarantees nearly continuous observations of the Sun, thanks to its geosynchronous orbit inclined by 28° about the longitude of the SDO-dedicated ground station in New Mexico, with a continuous science data downlink rate of 130 Megabits per second (Mbps) [111]. The SDO satellites carries three scientific experiments, visible in Fig.3.1:

- the Atmospheric Imaging Assembly (AIA) [91]

- the EUV Variability Experiment (EVE) [159]
- the Helioseismic and Magnetic Imager (HMI) [124]

Each of these instruments aims at characterizing how and why the Sun varies. They observe the Sun simultaneously.
For this thesis, the most relevant scientific instrument of the SDO mission is the AIA instrument, which will be briefly described below.

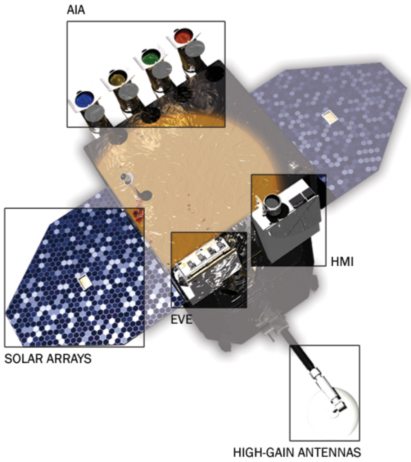

Figure 3.1: SDO spacecraft overview. The three scientific instruments' location on the spacecraft is highlighted. The three instruments observe the Sun simultaneously. In particular, the AIA instrument consists of four telescopes that image seven EUV band passes centered on specific emission lines. *Courtesy of NASA.*

AIA instrument

The Atmospheric Imaging Assembly (AIA) provides multiple simultaneous high-resolution images of the full solar disk, including the corona and the transition region up to 0.5 $R_\odot$ above the solar limb. It has a spatial resolution of 1.5-arcsec and a temporal resolution of 12-second. AIA is composed of four telescopes that employ normal-incidence, multilayer-coated optics in order to provide narrow-band imaging of seven extreme ultraviolet (EUV) band passes centered on specific lines: Fe XVIII (94 Å), Fe VIII, XXI (131 Å), Fe IX (171 Å), Fe XII, XXIV (193 Å), Fe XIV (211 Å), He II (304 Å), and Fe XVI (335 Å). Additionally, one telescope observes C IV (near 1600 Å) and the nearby continuum (1700 Å) and has a filter to observe in the visible in order to enable coalignment with images from other telescopes. The temperature covered by this range of EUV emissions goes from $6 \cdot 10^4 K$ to $2 \cdot 10^7 K$ [91]. Fig.3.2 shows a detail of the solar corona in each of the filters, while Fig.3.3 illustrates observations in the different wavelengths, indicating also which part of the atmosphere is better observed in that specific wavelength. For this thesis work, the choice of using only the 211 Å filter was made, since this wavelength is better suited to show the hotter, magnetically active regions in the Sun's corona.

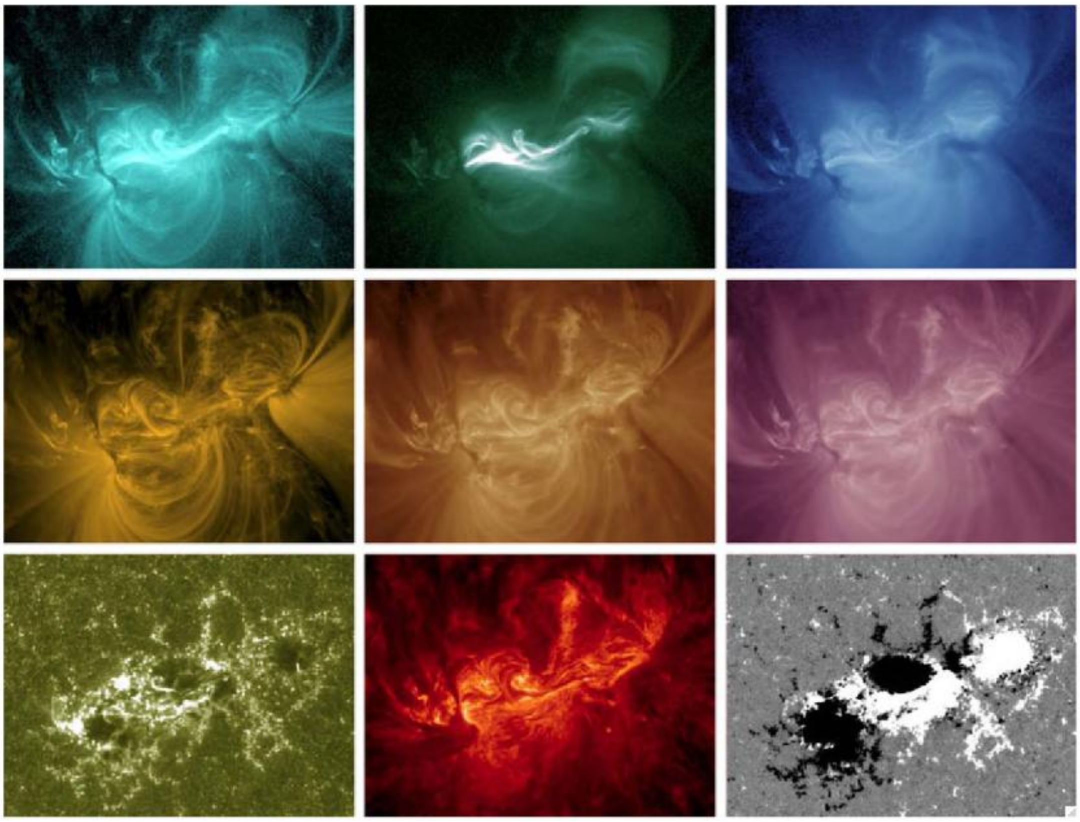

Figure 3.2: Images of an active region observed by AIA on 15 February 2011 at 01:45 UT. This mosaic of images helps to understand how different filters enable to differently sample the temperature-dependent solar corona. *Top row, from left to right:* observation in 131 Å, 94 Å, 335 Å. *Middle panels (left to right):* observation in 171 Å, 193 Å, 211 Å. *Bottom row (left to right):* observation in 1600 Å and 304 Å, with an addition HMI line-of-sight magnetogram of the same field of view. *Courtesy of [91].*

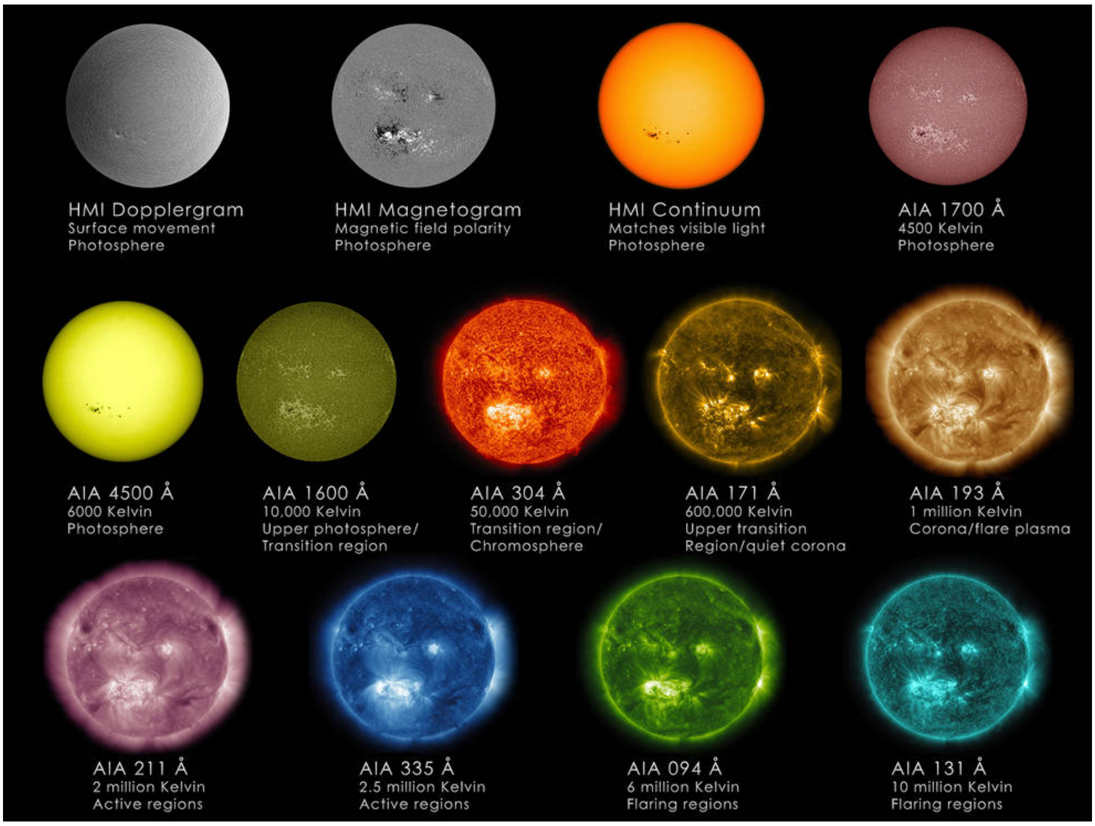

Figure 3.3: Portrait of the different wavelengths imaged by SDO, especially by AIA, to observe how solar material moves around the Sun's atmosphere, and HMI, which focuses on the movement and magnetic properties of the solar surface. Each of the wavelengths observed by SDO was chosen to emphasize a specific aspect of the Sun's surface or atmosphere. *Courtesy of NASA/SDO/GSFC.*

Each SDO science investigation team has a data archive of its science data products for the duration of the SDO mission. They made these data publicly available. For example, graphic formats are available at several websites, namely Helioviewer (http://helioviewer.org) and jHelioviewer (http://jhelioviewer.org), which allow the user to browse the AIA images to make and share movies from an archive of images in the JPEG2000 format.
From these public databases, AIA data can be obtained as either Level 1.5 or Level 1.0 data, which need to be upgraded to Level 1.5 by user software (for a description of the AIA data-product level see [91] and Chap.3.2). Routines for this purpose are available in the IDL language through the SolarSoft package [47] and in the Python language through the SunPy package [135].

Overall, AIA represents an increase in the information rate for coronal observations in comparison to the previous missions. Fig.3.4 shows a comparison of the image resolution of AIA with other two instruments, STEREO/SECCHI/EUVI [160] and SOHO/EIT [32]:

SDO's AIA instrument has twice the image resolution than EUVI and 4 times greater imaging resolution than EIT. The image cadence is also different: SDO/AIA is capable of taking 1 image per second (the general temporal resolution is approximately 10 to 12 seconds). In the best case, STEREO/EUVI is able of taking 1 image every 3 minutes whereas SOHO/EIT takes 1 image every 12 minutes.

Nowadays the SDO mission is one of the largest informative projects in the human history, providing more than 1.5 terabytes of the scientific data every day.

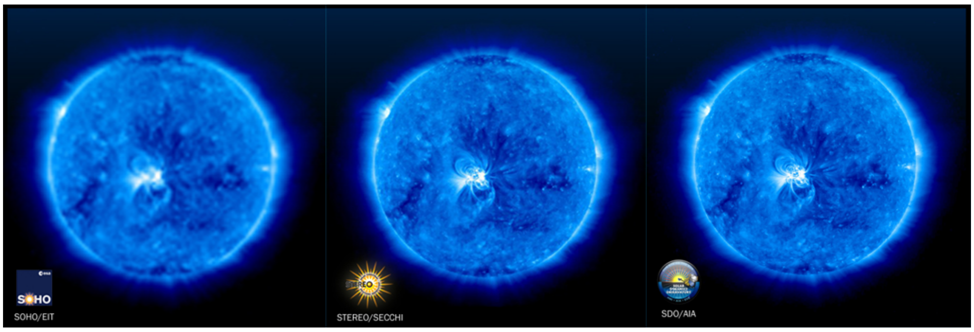

Figure 3.4: Comparison of the image resolution of SDO/AIA (*right*) with STEREO/SECCHI/EUVI (*middle*) and SOHO/EIT (*left*). *Courtesy of NASA.*

3.1.2. The STEREO mission

The twin Solar TErrestrial RElations Observatory (STEREO) [80] spacecrafts were launched on October 25th, 2006. STEREO is the third mission of the NASA's Solar Terrestrial Probes program (STP). It employs two nearly identical space-based observatories on heliocentric orbits: one is *ahead* of Earth in its orbit (STEREO-A), the other is trailing *behind* (STEREO-B). The two STEREO spacecraft provide the first-ever stereoscopic view of the Sun and its atmosphere. When these views are combined with data from observatories on the ground and in low-Earth orbit, STEREO data allows scientists to track the build-up and lift-off of magnetic energy from the Sun and to construct the trajectory of Earth-bound CMEs in 3-D. In fact, STEREO's scientific goal is to understand the causes and mechanisms of CME initiation and to characterize their propagation throughout the heliosphere. Furthermore, the STEREO mission investigates the mechanism of energetic particle acceleration in the low corona and the surrounding heliosphere and aims at improving the determination of the structure of solar wind.

Since STEREO-A is on a faster and closer to the Sun orbit compared to STEREO-B, the two satellites separated from each other over time, making the stereoscopic observation more difficult. On Oct. 1, 2014 communications with STEREO-B were lost, due to multiple hardware anomalies that affected the control of the spacecraft orientation. Communications with STEREO-B were re-established on Aug. 21, 2016, during a monthly attempt to reach the spacecraft using NASA's Deep Space Network. However, the attempt to recover the spacecraft was not successful. STEREO-B has now been out of contact since Sept. 23, 2016.

From a technological point of view, the two STEREO observatories are nearly identical: they are two solar-powered satellites with 3-axis-stabilization, with mass at launch of $\sim$ 620 kg, including propellant. The spacecrafts communicate with the APL-based Mission Operations Center via NASA's Deep Space Network. Fig.3.5 shows the STEREO satellite and its payloads.

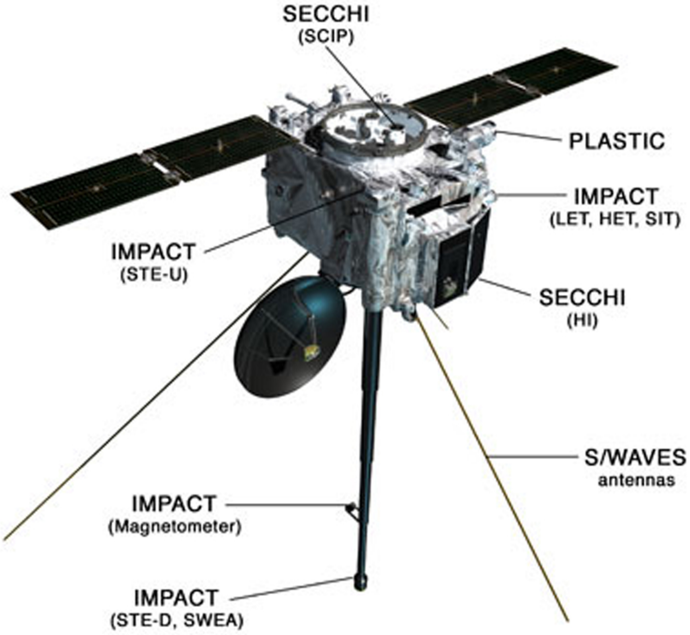

Figure 3.5: STEREO satellite overview. The scientific instruments and their location on the spacecraft are easily observable. *Courtesy of NASA*.

Each STEREO satellite carries four instrument packages:

- Sun Earth Connection Coronal and Heliospheric Investigation (SECCHI) [67], which consist of four instruments.
    - Extreme UltraViolet Imager (EUVI) [160]
    - Inner Coronagraph (COR1) [141]
    - Outer Coronagraph (COR2) [67]
    - Heliospheric Imager (HI) [45]

- STEREO/WAVES (SWAVES) [16]
- In-situ Measurements of Particles And CME Transients (IMPACT) [1]
- PLAsma and SupraThermal Ion Composition (PLASTIC) [50]

It will be shown in Chap.4 that data from SECCHI EUVI instruments were used in this thesis project for a comparison with the results obtained from AIA data.

The GOES mission

The GOES-R [37] Series is a National Oceanic and Atmospheric Administration (NOAA) mission, supported by the National Aeronautics and Space Administration (NASA): it is the latest generation of Geostationary Operational Environmental Satellites (GOES). The GOES-R Series is a four-satellite program including GOES-R, GOES-S, GOES-T and GOES-U (the letter is designated before the launch and is then converted to a number once the satellites reach the geostationary orbit). It provides advanced imagery and atmospheric measurements of Earth's weather, oceans and environment, real-time mapping of total lightning activity, and monitoring of solar activity and space weather. The instruments used for the GOES mission are:

- Advanced Baseline Imager (ABI) [125]
- MAGnetometer (MAG) [130]
- Geostationary Lighting Mapper (GLM) [54]
- Space Environmental In-Situ Suite (SEISS) [86]
- Solar UltraViolet Imager (SUVI) [144]
- Extreme Ultraviolet X-Ray Irradiance Sensor (EXIS) [43]

In particular, on board EXIS are two main sensors, the Extreme Ultraviolet Sensor (EUVS) [42] and the X-Ray Sensor (XRS) [41], to monitor activity on the Sun. XRS monitors solar flares and helps in predicting solar proton events that can penetrate Earth's magnetic field. It is useful to alert scientists in case of X-ray flares that are strong enough to cause radio blackouts or that may be associated to CMEs, so it is a really important for space weather predictions.

3.1.3. SunPy environment

SunPy is a free and open-source solar data analysis environment for Python. In particular, this research used version 4.0.0 of the SunPy open source software package [135].

Its goal is to be a comprehensive data analysis environment that allows researchers within the field of solar physics to carry out their tasks with the minimal effort. SunPy is build upon the scientific Python environment. This environment already includes several core packages, namely NumPy, SciPy, Matplotlib and Pandas. Furthermore, SunPy is also developed in close association with the AstroPy package in the Python astronomy ecosystem, which is fundamental since SunPy deals with key astrophysical concepts. The SunPy package firstly appeared in March 2011 thanks to the work of a small group of scientists and developers at the NASA Goddard Space Flight Center. Since then, SunPy has grown from the original small group into a large community python package and is continuously evolving and updating.

Indeed, since the beginning of this thesis work, the Sunpy package underwent several improvements and new functionalities have been added.

This thesis uses the sunpy core package, which enables the data downloading in the FITS format and their handling, and the aiapy package, for analyzing data from the SDO/AIA instrument, namely for converting AIA images from Level 1 to Level 1.5 and further solar data analysis.

Figure 3.6: Sunpy logo.

As already pointed out in the previous chapters, the majority of scientists rely on the usage of the SolarSoft (SSW) library in the IDL language, which is available for the community since 1990s [13]. A survey in 2020 asked researchers in the field of solar physics for a preference; 73% of respondents reported using IDL compared to 66% who use Python [15]. In particular, SolarSoft supports the latest missions in the Heliophysics System Observatory, including the Parker Solar Probe, Solar Orbiter, SDO and GOES 16 and 17 missions.

However, Sunpy has had a huge development in almost 10 years and this can be attributed to its versatility and flexibility, but mostly to its being a free open-source environment. This aspect is enough to guarantee a ceaseless and rapid growth thanks to the users sharing advice and corrections. In addition, the computer science field, e.g. Machine Learning and Computer Vision communities, are developing algorithms mostly in Python.

The solar physics community still strongly appreciates the value that SolarSoft provides trending towards a seamless access to both SolarSoft and SunPy tools in one interface to allow researchers to work in one single environment. SSW support for running in Jupyter notebooks, and Jupyter-based interactive tutorials are being developed [73].

3.2. Data acquisition and pre-processing

To search for and download data the primary interface *sunpy.net.Fido* is used. It is a unified data search and retrieval tool that provides simultaneous access to several online data sources, some of which cover multiple instruments and data products, like the Virtual Solar Observatory (VSO), while some are specific to a single source. To search for data with Fido, attributes, like observatio time, instrument and wavelength, need to be specified: for this thesis work SDO/AIA instrument and data in 211Å are primarily used. The selected time cadence is of 5 min for the first 24 hours and 30 min for the remaining 48 hours, except for one of the cases (September 06 2011), where the time cadence is 5 min for the entire 48 hours interval.
The data found with *Fido* can be saved in the format of FITS files (Flexible Image Transport System), which is an open standard defining a digital file format useful for storage, transmission and processing of data in astronomy and solar physics.
Once all the data are correctly saved in the form of FITS files, they can be uploaded in Jupyter Notebooks from the local memory and be converted into *maps*. Maps are the primary data type in Sunpy: they are 2D data associated with a coordinate system. Sunpy Maps can be used with any image with two spatial axes ("data" part) that has FITS standard compliant metadata ("metadata" part). Some relevant metadata are related to the *exposure time* the image was taken at, the *dimensions* in pixel of the image, the *coordinate system* (default: helioprojective), the *observation date* and the *wavelength*. Some more technical metadata keywords are *crpix-n* (pixel of the reference coordinate, that is n=1 or n=2 for axis x and y respectively), *cdelt-n* (angular resolution per pixel, in $arcsec/pixel$, and the value of n is the same as for *crpix-n*) and *radius of the Sun*, both in $meters$ or $arcsec$.

Fido provides data at Level 1.0. However, the high temporal cadence of SDO/AIA full-disk solar images in multiple wavelength channels enables also the display of images into a movie sequence. To do so, Level 1.5 data processing is essential as it accomplishes three corrections in a single step [91]:

1. The raw images need to be rotated so that solar North is at 0° (at the top of the image array). The four AIA telescopes were aligned prior to launch but no further adjustment is available on orbit, so a small residual roll angle exists between the

four AIA telescopes.

2. The second correction has to do with the plate-scale size of the telescopes: a plate-scale adjustment is made to set the image scale to exactly 0.6 arcsec per pixel (in Sunpy, the change is visible through the *cdelt* metadata keyword). This is needed since each telescope has a slightly different focal length and, as a result, the number of arcsecs per CCD pixel varies slightly among the telescopes.
3. The third adjustment regards the bore-sight pointing of each telescope, which was coaligned prior to launch to within 20 arcsec (similarly as the roll angle). The four telescope bore-sights are coaligned by adjusting on orbit the secondary-mirror offsets. Then, residual differences are removed during ground processing by interpolating the images onto a new pixel coordinate that places the Sun's center at the middle of each telescope detector.

When exported as FITS files, the file header structure for Level 1 and Level 1.5 have exactly the same keywords but with values set to reflect the level of processing.

The pre-processing of the Sunpy maps comprises their calibration and upgrade of from Level 1 to 1.5. These steps are done in Sunpy by means of *aiapy*, which is a Python package created for analyzing data from the SDO/AIA instrument. The steps and the corresponding functions (also shown in Fig.3.7) are:

- Check the metadata keyword for exposure time. If the map has a higher or lower exposure time than the chosen threshold, then discard it.
- Correct the metadata keywords for the heliographic longitude and latitude (*fix_ observer_ location* function).
- Process the full-disk Level 1 AIA Map into a level 1.5 AIA Map (*register* function).
- Normalize each image by the exposure time, that is divide each pixel intensity by the exposure time value extracted from the FITS header, where some relevant metadata keywords are (*normalize_ exposure* function).
- resample from 4096 × 4096 to 2048 × 2048 pixels. Note that this steps modifies the *cdelt* metadata keyword from 0.6 arcsec/pixel (result of *register* function) to 1.2 arcsec/pixel.

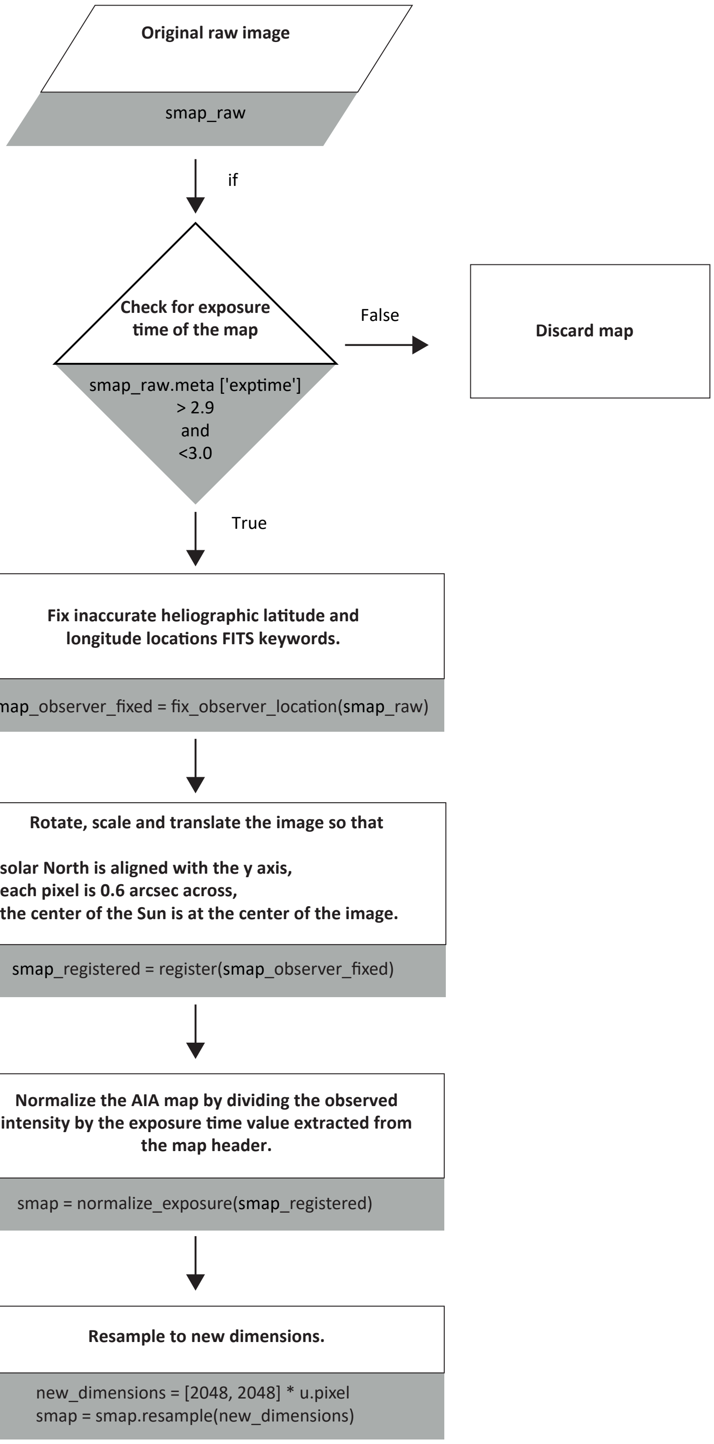

Figure 3.7: Flowchart of the pre-processing and calibration of the Level 1 SDO/AIA images in Python, using *aiapy* functions. The white boxes contain a qualitative description of the steps, while the grey boxes contain lines from the code. Parallelograms contain variable names, rectangles contain the step description and the corresponding Python functions, the diamonds indicates a condition to check, whose output is either True or False.

3.2.1. Differential rotation

To study the evolution of a solar event (e.g., a solar flare or coronal mass ejection), it is useful to rotate each image in the dataset to the same fixed frame. Taking into account the differential nature of the Sun's rotation, the maps not only need to be rotated to a selected frame, but they need to be differentially rotated depending on their latitude. The event occurring on September 6, 2011 will be used as an example to show the algorithm's implementation.

Each image is rotated back in time to a pre-event frame, that is taken 30 min before the eruption begins. This pre-event image will be hereafter called basemap.

The differential rotation algorithm outputs a map whose frame is the same as the input map (map at a generic time t_n) but rotated by a certain amount, according to a prescribed time difference of t_n to t_0, that is the deduction of the input map observation time from to the basemap observation time t_0. The WCS (World Coordinate System) [28] of the basemap is used to reproject the pixels array from the input map frame to the basemap's frame. WCS is a functionality of the *astropy* library that describes the geometric transformations between one set of coordinates to another. Sunpy indicates a procedure for rotation of the Sun's disk from the WCS of one image to a desired one and some of the needed functions are *Helioprojective*, *RotatedSunFrame* and *transform_with_sun_center*. The required steps and the corresponding functions are shown in Fig.3.8.

One thing to notice is that after the differential rotation is applied to the image the off-limb data of the image are lost, meaning that the off-limb pixels assume the Not-a-Number (NaN) value, as observable in Fig.3.9. In addition, there is distortion of the image due to the rotation of the available pixels that needs to be taken into account. The longer the time of rotation, the stronger the distortion in the image, until portions of the solar disk disappear because of the eastward rotation of the area of interest on the other side of the solar sphere, thus implying a lack of data in the image. This is already partially visible in Fig.3.9, where the map of interest is taken 3 days after the basemap.

Since the goal of this work is to analyze a sub section of the images that contains the dimming, the progressive appearance of NaN pixels in the desired sub-portion brings a non-acceptable estimation of the desired parameters, thus events close to the eastern limb cannot be analyzed for the 3 days of interest of the thesis.

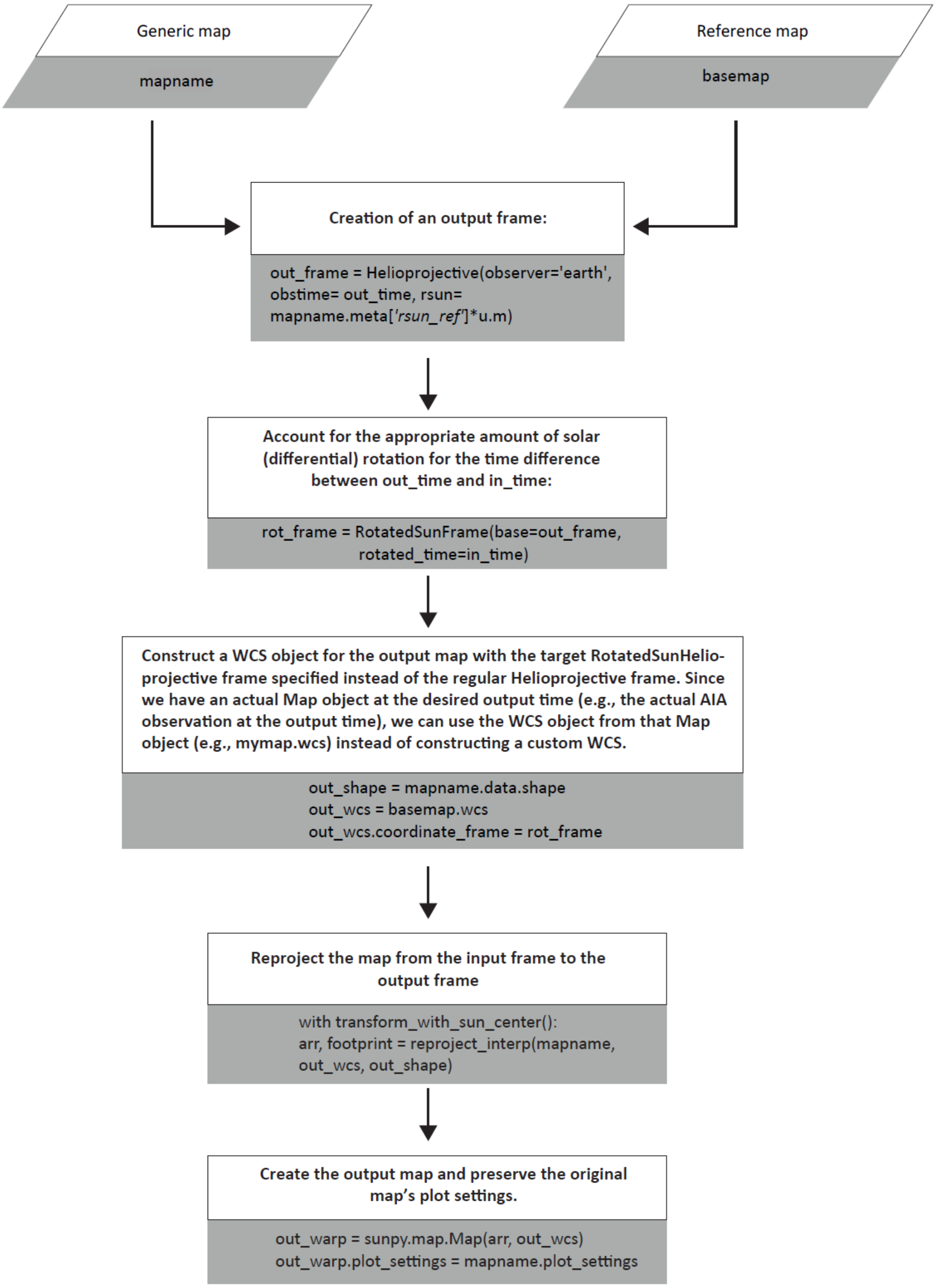

Creation of an output frame:

```
out_frame = Helioprojective(observer='earth',
obstime= out_time, rsun=
mapname.meta['rsun_ref']*u.m)
```

Account for the appropriate amount of solar (differential) rotation for the time difference between out_time and in_time:

```
rot_frame = RotatedSunFrame(base=out_frame,
rotated_time=in_time)
```

Construct a WCS object for the output map with the target RotatedSunHelioprojective frame specified instead of the regular Helioprojective frame. Since we have an actual Map object at the desired output time (e.g., the actual AIA observation at the output time), we can use the WCS object from that Map object (e.g., mymap.wcs) instead of constructing a custom WCS.

```
out_shape = mapname.data.shape
out_wcs = basemap.wcs
out_wcs.coordinate_frame = rot_frame
```

Reproject the map from the input frame to the output frame

```
with transform_with_sun_center():
arr, footprint = reproject_interp(mapname,
out_wcs, out_shape)
```

Create the output map and preserve the original map's plot settings.

```
out_warp = sunpy.map.Map(arr, out_wcs)
out_warp.plot_settings = mapname.plot_settings
```

Figure 3.8: Flowchart of the differential rotation algorithm. The white boxes contain a qualitative description of the steps, while the grey boxes contain lines from the code. Parallelograms contain the input variable names, rectangles contain the step description and the corresponding Python functions.

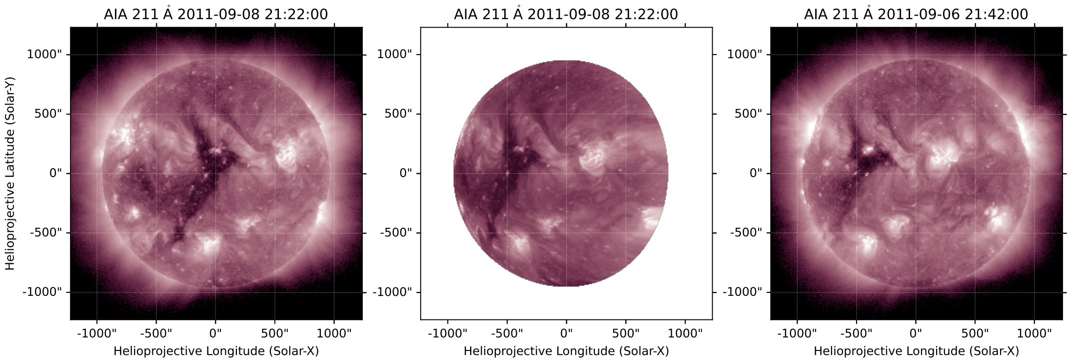

Figure 3.9: *Left*: original image on September 8, 2011 at 21:22 UT. *Center*: map on September 8,2011 at 21:22 UT after differentially rotating it back to the basemap time, i.e. September 6, 2011 at 21:42 UT (*on the right*). The first thing that can be noticed (in the *central map*) is that the differential rotation procedure discards the off-limb data, so only on-disk measurements are available. Secondly, a distortion of the solar disk on the right appears, making the image of the Sun no more circular; this is because those pixels are located on the other side of the solar sphere on September 8 at 21:22 UT and information about them cannot be retrieved when the rotation correction is performed.

3.2.2. Base-Difference and Logarithmic Base-Ratio images

To study their evolution in time, the dimming regions must be firstly identified. In accordance to the procedure described by Dissauer et al. (2018a) [34] in Chap.2.2.1, BD images and LBR images are employed.

BD images are usually used for the identification of dimmings. They allow to visualize the absolute changes in intensity, knowing that the regions showing large changes are generally active regions and coronal loops on the Sun. BD images are obtained by subtracting the basemap from each image in the data set:

$$BD = F_n - F_0 \tag{3.1}$$

where F_n and F_0 are the image's frame at the generic time t_n and the pixel frame of the basemap, which is at the reference time t_0, respectively.
However, coronal dimmings, and particularly secondary dimmings, develop in quiet Sun regions, which are regions of low coronal intensity. Thus, the changes in brightness cannot be resolved by using only absolute values. In addition, the density in the upper corona is lower compared to regions closer to the Sun surface, so it is also difficult to detect changes

in the upper corona by looking at the absolute values.
This is why LBR were introduced [34]: they show relative changes in intensity, since they are obtained by the division of each image by the basemap. In this way, changes in the intensity of high-intensity regions (namely, coronal loops) and low-intensity regions (namely, quiet Sun) are considered in an equal manner. To make these relative changes even more visible, a logarithmic operator (log10) is used.

$$LBR = log(F_n/F_0) = log(F_n) - log(F_0) \tag{3.2}$$

where, again, F_n and F_0 are the generic image's frame at the time t_n and the base image's frame, respectively.
Finally, data are cropped to create sub-maps that contain the dimming region. The selection of the cropping coordinates is done manually.

In this thesis, the detection algorithm is based both on logarithmic base-ratio and base-difference data. In particular, LBR are used for the identification of the darkest pixel within the dimming and BD images are used for the extraction of relevant dimming parameters.

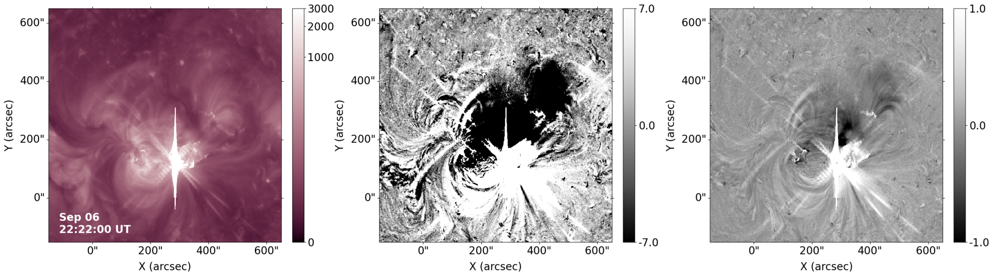

(a) September 6, 2011 at 22:22 UT, that is the flare peaking time.

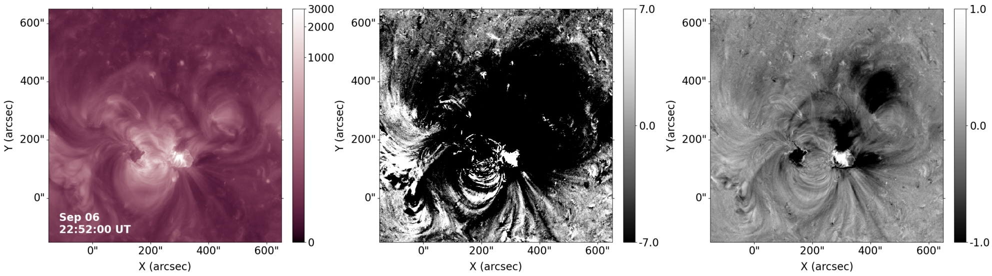

(b) September 6, 2011 at 22:52 UT, 30 min after the flare occurred.

Figure 3.10: The basemap time is September 6 2011, 21:42 UT. *Left*: original image. *Center*: BD image. *Right*: LBR image. obtained from two images on and at and plotted against the histogram of the basemap (*in black*). *Top row*: BD images, used to observe absolute changes in intensity. It is possible to observe the dimming formation and expansion. *Bottom row*: LBR images, used to observe relative changes in brightness. Some concentrated darker areas are more evident.

3.3. Dimming Detection Methodology

Hereafter is a description of the steps for dimming detection and next is an explanation of the dimming parameters computation. To analyze the dimming recovery time, the parameters that were deemed relevant for the thesis' purpose are the brightness and the area. In particular, for what regards the brightness, the sum of the instantaneous values is used to study the dimming over time in accordance with [34]. However, after the first results, it was decided to apply different approaches, which will be be described in Chap.3.3.3. Note that the region growing algorithm and the algorithm to compute the area are created ad hoc for this thesis, since they were not available for Python language.

3.3.1. Histograms and thresholding method

As mentioned above, the processed maps are cropped in correspondence of the dimming location. Then, the histogram of these maps are obtained. They are used to analyse the evolution of the event: after the flare/CME eruption, the behaviour of the pixel intensity in the histograms shows a shift towards negative values, as expected of a dimming appearance. Fig.3.11 shows the histograms for the BD cropped image and LBR cropped image for September 06, 2011 at two different time instants to better appreciate the variation in the pixel behaviour.

After histograms are prepared, the thresholding level for pixel intensity has to be determined in order to identify the dimming region [34]. The mean value of the intensity of the image is used for this purpose.

By looking at both the BD and LBR histograms behaviour and at the mean value evolution of different events and by making a comparison with previous works ([34], [24]), the threshold level is decided as $-0.19\ DN$ for LBR images. All pixels below this threshold are identified as dimming pixels.

Actually, the resulting regions are still too noisy to be considered 100% dimming regions. Noise is identifiable in the form of small regions scattered throughout the image and by the lack of well-defined boundaries for the expected dimming. This is why a region growing procedure is introduced and the definition of dimming pixels of this chapter will be useful for the identification of the thresholding level of the region growing algorithm.

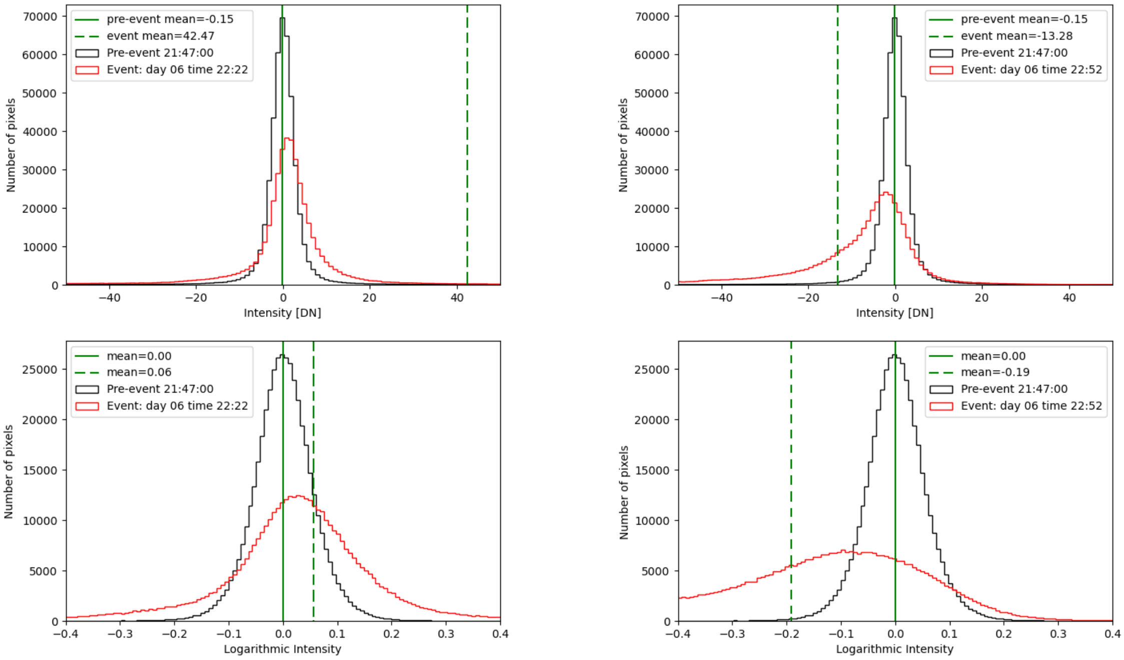

(a) Histogram at the flare peaking time. (b) Histogram 30 min after the flare occurred.

Figure 3.11: Histograms (*in red*) obtained from two images on September 6, 2011, one at 22:22 UT (flare peaking time) and at 22:52 UT and plotted against the histogram of the basemap (*in black*). *Top row*: BD images. *Bottom row*: LBR images. The vertical lines correspond to the mean intensity value of the dataset. In particular, the full line corresponds to the basemap mean value, equal to 0 since there is no particular predominance of either bright or dark pixels, while the dashed line is the event image mean value. It is possible to notice how at the flare peak time the dashed line is visibly on the right side (majority of bright pixels), while at 22:52 UT it is on the left side, meaning that dark pixels are more numerous.

3.3.2. Region Growing algorithm

The region growing procedure is one of the segmentation techniques, i.e. processes to partition a digital image into multiple image segments (also called regions or objects), that are sets of pixels. Segmentation helps in simplifying and changing the representation of an image into something that is more meaningful and easier to analyze [127]: it is typically used to locate objects and boundaries (lines, curves, etc.) in the images. More specifically, the region growing is a simple region-based segmentation or could also be classified as a pixel-based image segmentation method, because of the selection of initial seed points.

The region growing is a method that is easily available in IDL thanks to the routine *region_grow*, where "the REGION_GROW function performs region growing for a given region within an N-dimensional array by finding all pixels within the array that are connected neighbors to the region pixels and that fall within provided constraints. The constraints are specified either as a threshold range (a minimum and maximum pixel value) or as a multiple of the standard deviation of the region pixel values. If the threshold is used (this is the default), the region is grown to include all connected neighboring pixels that fall within the given threshold range. If the standard deviation multiplier is used, the region is grown to include all connected neighboring pixels that fall within the range of the mean (of the region's pixel values) plus or minus the given multiplier times the sample standard deviation."
As an output, "REGION_GROW returns the vector of array indices that represent pixels within the grown region. The grown region will not include pixels at the edges of the input array. If no pixels fall within the grown region, this function will return the value -1."[29]

This type of function does not exist in Sunpy nor is there an indicated procedure to implement this method. For this reason, a Python algorithm was developed using the IDL routine as a guideline. It was chosen to implement the threshold approach. First, it is necessary to identify the seed pixels: they are retrieved from the LBR images as the 10% of the darkest pixels in the image. This percentage value is chosen after a trial and error procedure and is the percentage that guarantees that the extracted area is not very noisy (due to the presence of small areas) nor suffers the loss of significant areas, which may be not detected with a too small number of seeds.
Once the seed pixels are identified, the region growing algorithm is applied to the LBR maps. The initial region begins at the exact location of the seeds and then the image regions are grown from these seed pixels to adjacent pixels depending on a certain "membership" criterion, that in this case is the threshold of -0.19 DN (histograms were useful to determine a suitable threshold value for segmentation as well). If needed, a threshold range, like in IDL, could be set, but for this thesis' goal it is enough to set only the maximum pixel value.
It is possible to use 4-connected neighborhood (left, top, right and bottom pixels) to grow from the seed points or, alternatively, the 8-connected neighborhood (which counts also the diagonal pixels). The former is the default method, since it is less computationally expensive while providing satisfying results. As long as the neighboring pixels have inten-

sity below this value, they are added to the region and increase its size. Region growing is iterated until there are no pixels which respect the selected criterion.
To sum up, the algorithm is applied to every LBR map in the data set and the main steps are:

- Seed pixels are chosen: 10% of darkest pixels in the image.
- Seed pixels are compared with neighbouring pixels (4-connected neighborhood);
- Region is grown from the seeds by adding in neighbouring pixels that are similar, i.e. respect the "membership" criterion: intensity lower than $-0.19\ DN$. As a result, the size of the region is increased by adding in these pixels;
- When the growth of one region stops, the algorithm moves to another seed pixel which does not yet belong to any region and starts again;
- The algorithm stops when there are no more seed pixels.

A more accurate representation of the algorithm main steps can be seen in Fig.3.12. The output of the region growing function is a new Sunpy map containing a binary data array and the metadata of the original LBR map. On computers, RGB color components are standardly defined on a scale from 0 to 255, which is 8 bits or 1 byte: the values 0 and 255 correspond to black (minimum amount of light) and white (maximum amount of light) colors, respectively. Hence, all the non-dimming pixel in the output map have value 0 and where all the detected dimming pixels' value is 255. Pixels on the edge are assigned the intermediate value of 150 and are ultimately discarded (their value is converted to 0) since they do not respect the chosen criterion: they are generally positive pixels that stopped the region from growing further. It was also decided not to use any morphological operator to fill the small gaps in the image, so as to avoid the possible inclusion of bright pixels within the dimming region.
The output binary map can be used to define an instantaneous dimming pixel mask $D_n(p_i, t_n)$ that allows the identification of the dimming pixels p_i at each time step t_n [34]. Masking is performed by feeding the binary data array to the attribute *mask* of the Sunpy map of interest (be it the original AIA map, a BD map or a LBR one): Boolean value for the mask is 0 (False, do not mask) for dimming pixels and 1 (True) elsewhere.

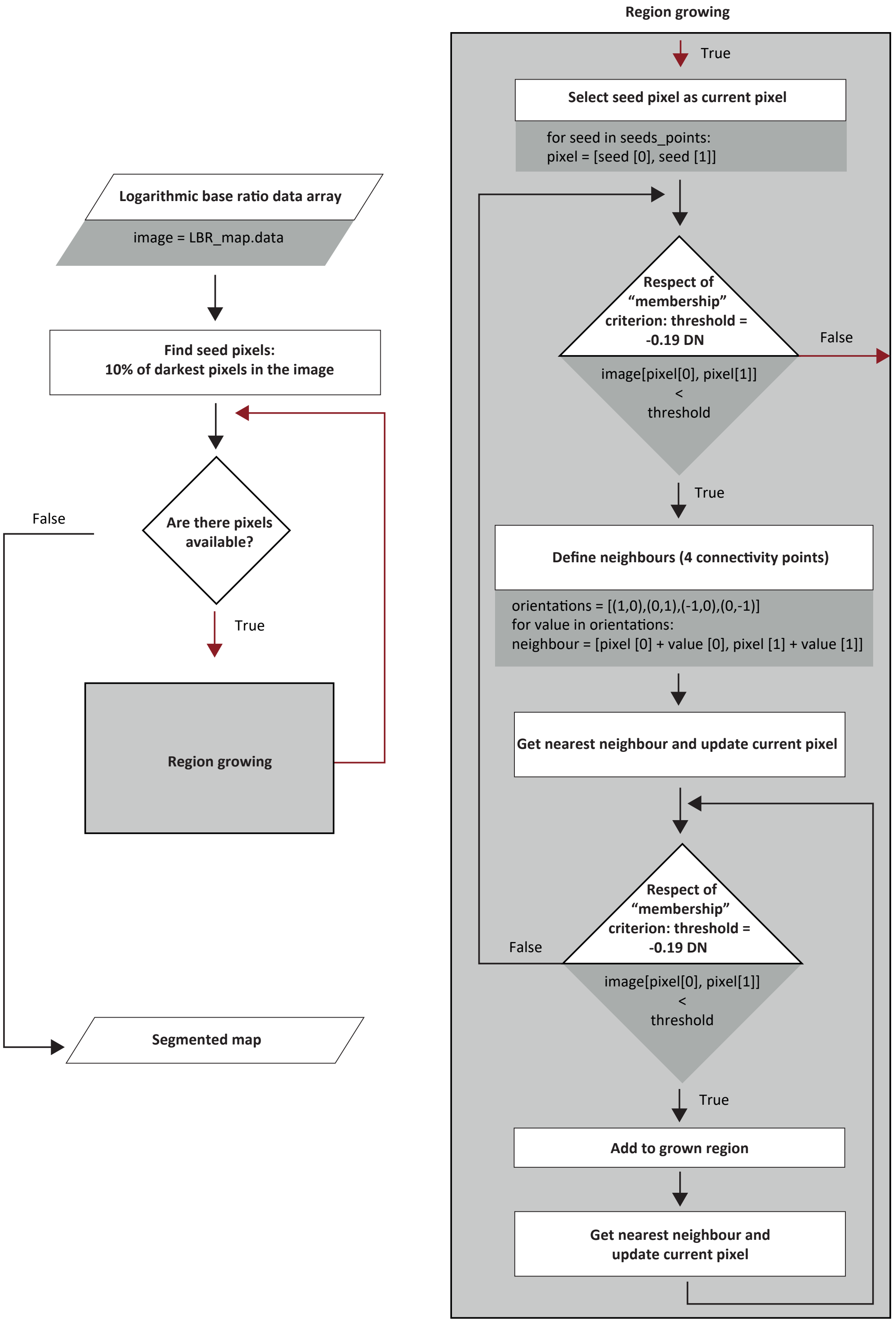

Figure 3.12: Flowchart of the region growing algorithm. *Left*: main flow of the algorithm. *Right*: zoom and expansion on the steps to grow the region. The white boxes contain a qualitative description of the steps, while the grey boxes contain lines from the code. Parallelograms contain the input and output variable names, rectangles contain functions and diamonds contain conditions for loops.

Overall, there are several advantages in using the region growing approach, some of which are: the capacity of correctly identifying regions which have the indicated properties, the creation of images with clear edges and need of a not too big number of seed points to represent the desired properties. However, this method is computationally expensive and requires long time to obtain results for huge data sets. A comparison between a simple thresholding method and the output of the region growing is presented in Fig.3.13. The threshold to identify dimming regions is the same ($-0.19\ DN$) in both cases, but using region growing allows to discard all the scattered and numerous noisy pixels.

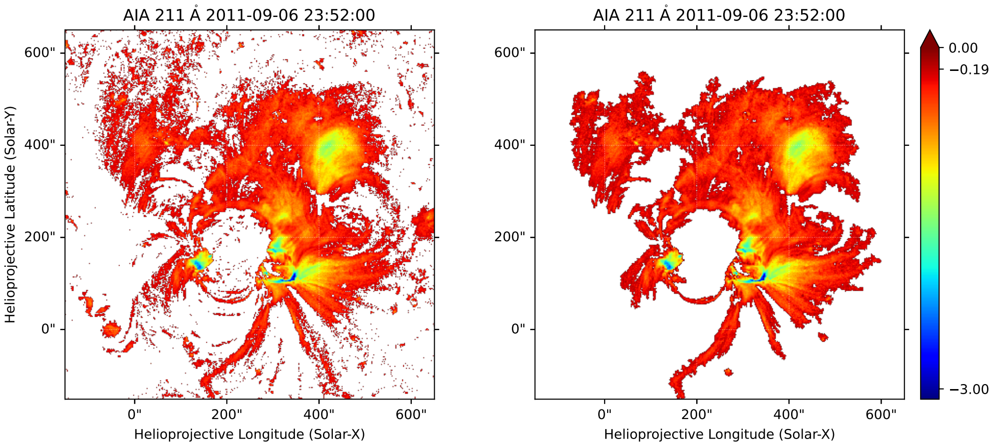

Figure 3.13: *Left*: BD image after the application of the mask: pixels with intensity below $-0.19\ DN$ are masked. The red color is chosen to better visualize the remaining noise. *Right*: output of the region growing algorithm. The image is a binary (black/white) image. The boundaries of the region are more defined, noise is no more present and some area are not included in the grown region because they are not simply connected to the identified seeds.

3.3.3. Fixed mask and Pixel boxes approach

Coronal dimmings are CMEs-related and, in particular, the dimming represents the CME footpoint in the low corona. Thus, the total brightness of a dimming could be used to measure the amount of evacuated plasma: the darker and the more extended the dimming region, the more plasma should be evacuated ([3], [98]). In this work, the total brightness is defined as the sum of dimming pixel intensities in base-difference images. The instantaneous total brightness I_{inst} of the dimming region at time step t_n is computed as:

$$I_{inst}(t_n) = \sum I(p_i, t_n) D_n(p_i, t_n) \tag{3.3}$$

where $I(p_i, t_n)$ is the intensity at t_n for a certain dimming pixel p_i within the instantaneous dimming mask $D_n(p_i, t_n)$. In this way it is possible to analyze the instantaneous state of the dimming region in terms of intensity. A minimum in the time evolution of I_{inst} can be due to either a maximum dimming area or a minimum intensity of these pixels. Hence, it is important to accompany the instantaneous intensity with the dimming area evolution. Instantaneous brightness curves are the standard approach suggested by [34].

However, this method has been generally used for analysis of short periods of time after the solar event occurred, whereas the analysis in this thesis covers about 3 days. In addition, this approach is dependent on the extension of the dimming region itself, which generates a limitation in the long-term: by using the region growing algorithm, seed pixels that are not strictly related to the dimming case under study will be identified, e.g. due to other eruptions from the same AR. The presence of new dark areas, which may not be proper dimming regions or could be dimmings related to other events, triggers the algorithm to grow regions and so the detected dimming is always evolving in shape and extension. In order not to be influenced by this variation, a new approach is suggested: a unique mask is applied to each image in the data set. This "fixed" mask is chosen as the largest dimming, quantified by the number of total dimming pixels p_{tot} in the LBR maps, within the first two hours from the beginning of the flare activity. This amount of time is considered enough to comprise the impulsive phase of the flare and of the dimming. Then, the map with the maximum dimming extension at time t_{max} within the impulsive phase is used as a mask on top of every BD map. Finally, the instantaneous brightness in the fixed mask $I_{f.m.}$ is computed as the sum of all the pixels intensity inside the unmasked region, with no distinction between dimming pixels and non-dimming pixels.

$$I_{f.m.}(t_m) = \sum I(p_i, t_m) D_{fixed}(p_k, t_{max}) \tag{3.4}$$

where $I(p_i, t_m)$ is the intensity at t_m for a certain dimming pixel p_i within the fixed dimming mask $D_{fixed}(p_k, t_{max})$.

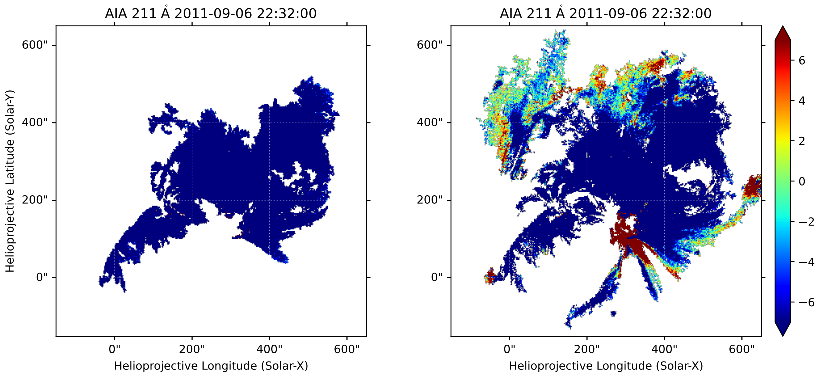

(a) September 6 2011, at 22:32 UT, 10 min after the eruption of an X-class flare. *Left*: instantaneous dimming mask. *Right*: fixed dimming mask. Both masks are applied on the same BD image.

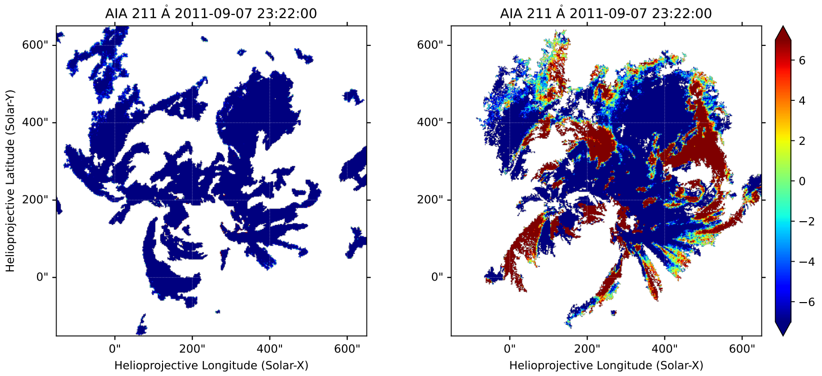

(b) Same as Fig.3.14a but for September 7 2011, at 23:32 UT, around 1 hour after the eruption of an X-class flare.

Figure 3.14: Comparison between the instantaneous dimming mask and the fixed dimming mask at two different time instants. In both cases, the basemap is taken on September 6, 2011 at 21:42 UT and the fixed mask is the dimming extension on September 6, 2011 at 23:22 UT. The difference between the two approaches is quite evident.
Fig.3.14a: the detected dark areas (*in blue*) are similar, but the fixed mask includes also some bright pixels. *Fig.3.14b*: the instantaneous dimming region has a completely different orientation with respect to the fixed dimming mask. In this case, the region growing algorithm has detected the dimming related to the flare on September 7, thus the information about the dimming generated after the flare on September 6 is mixed with these new dark pixels. On the contrary, the fixed mask is keeping the focus on the region of interest, thus limiting the radius of action of the unwanted dimming detection.

Furthermore, it was decided to investigate an even smaller fraction of the overall map: 3x3 pixel boxes are small enough to avoid interference from outside their boundaries but big enough to track the intensity behaviour. They are placed on top of the original SDO/AIA images, the BD images and the LBR images, then the mean value of the pixels' intensity inside each box is computed. The location of each box is manually selected: interesting area are identified by looking at the sequence of original images, then the positioning is adjusted by means of the LBR images, where dimming regions and boundaries are identified more easily even bare-eyed. At first, the majority of the boxes were placed dark areas firstly appear (origin of dimming regions), and the evolution over time was monitored to ensure that the boxes were inside the dimming region for most of the time. Then, some other boxes were located in other interesting areas, namely very close to the eruption site to investigate the region after the flare bright light stops covering the corona beneath. This approach is very versatile and permits to observe different behaviours.

3.3.4. Area estimation

As explained at the beginning of Chap.3.3.3, the area needs to be computed to have a better understanding of the instantaneous intensity behaviour. However, it is tricky to estimate the area of a specific region on the solar disk since data from SDO and the other satellites are 2D planar images, which cannot account for the tridimensionality of the Sun. Taking into consideration the spherical nature of the Sun is essential not to underestimate the area: pixels close to the limb do not represent the same surface as pixels close to the solar disk center. For this reason, two approaches were implemented and compared. The first, hereafter called geometrical approach, is a rough approximation of the solar sphere, while the second, called integral approach, is more precise and is hence chosen for the analysis.

For what regards the geometrical approach, it is assumed that pixels at the center of solar disk have pixel area equal to 1, i.e. the pixel's area is equivalent to one pixel (no distortion effects due to the curvature of the Sun). A new map is created and its size is the same as the input map. The meta data are inherited from the input map, namely:

- Radius of the Sun "$R_{Sun_{pix}}$" in pixel is obtained by dividing the keywords "$rsun\_obs$" [$arcsec$] and "$cdelt1$" [$arcsec/pixel$]
- Central pixel coordinates [cenX, cenY] :
  - $cenX$: "crpix1"-1
  - $cenY$: "crpix2"-1

Note that CRPIXn (n is either 1 for axis x or 2 fr axis y) follows the Fortran convention of counting from 1 to N, instead of 0 to $N-1$ as is done in Python programming language. For this reason 1 is subtracted from each coordinate. After this, the coordinates of each pixel on the solar disk are found by means of the Sunpy functions "*all_ coordinates_from_ map*" and "*coordinate_ is_ on_ solar_ disk*", which enable the creation of a map where True corresponds to a pixel on solar disk. The coordinates are then stored and will be used for the computation of the radius of each pixel:

$$r = \sqrt{(cenX - x)^2 + (cenY - y)^2} \tag{3.5}$$

This radius is normalised with respect to the radius of the Sun:

$$r_{norm} = \frac{r}{R_{Sun_{pix}}} \tag{3.6}$$

Lastly, the area of each pixel is computed, with respect to their distance from the center of the disk:

$$pixel\_area = \frac{1}{acos(r_{norm})} \tag{3.7}$$

Then, Sunpy maps where each pixel value corresponds to the area value are created. There is a large interval between 1 (at the center of the Sun's disk) and the obtained maximum values (close to the limbs) and this is dependent on the ratio $\frac{r_{norm}}{R_{SUN_{pix}}}$: the further the coordinate is from the center of the solar disk, the closest to 1 the ratio will be and so the *arccosine* will tend to 0, implying high values of pixel area. Hence, really huge values suddenly appear in proximity of the limbs.

Thus, this method is not reliable for observations close to solar limbs. Being the main focus of this thesis the analysis of on-disk events, the values of the Sun's boundaries could be ignored.

To overcome the limitation and imperfections of the geometrical method, a more sensitive and accurate algorithm was developed and validated in this thesis work.

The idea is to calculate the entire area of the solar surface, which is projected on a circle delimited by solar limbs, using a double integral over the surface:

$$A = \int\int \sqrt{1 + \left(\frac{dz}{dx}\right)^2 + \left(\frac{dz}{dy}\right)^2} dxdy \tag{3.8}$$

considering the relation between the coordinate set (x, y, z) and the solar radius $R^2 = x^2 + y^2 + z^2$.

To do so, a first approximate area of a pixel is estimated. Knowing that the area of the sphere is $4\pi R_{km}^2$, then the Sun's visible surface is half of the sphere

$$Area_{Sun_{km}} = 2 \cdot \pi \cdot R_{km}^2 \tag{3.9}$$

Then, by knowing the radius of the Sun in pixels (rad_{pix}), it is possible to compute the Sun's visible surface in pixels, which in this case is a circle area (AIA images are projections of half the solar sphere onto 2D planes):

$$Area_{Sun_{pix}} = \pi \cdot rad_{pix}^2 \tag{3.10}$$

Finally, the area of the pixel can be computed as

$$Area_{pixel} = \frac{Area_{Sun_{km}}}{Area_{Sun_{pix}}} \tag{3.11}$$

The meta data stored in the Sunpy maps contain the keywords '$rsun\_ref$', that is the value of the solar radius in km, $R_{km} = 696\ 000\ km$, '$rsun\_obs$', that is the solar radius in $arcsec$, and '$cdelt$'=1.2, that is the angular resolution per pixel ($arcsec/pixel$). '$rsun\_obs$' is a value slightly changing from map to map, but here is approximated as 966 $arcsec$. It is possible to compute the solar radius in number of pixels as $rad_{pix} = \frac{rsun\_obs}{cdelt} = 805$. By using these values, one gets

$$Area_{Sun_{km}} = 3.0437 \cdot 10^{12}\ km^2$$

$$Area_{Sun_{pix}} = 2.035 \cdot 10^6$$

$$Area_{pixel} = 1.495 \cdot 10^6\ km^2$$

This is the general concept that is applied in the integral, but by taking into account the coordinates of each pixel in the image and discarding the ones that are located off-limbs. Then, one integral is solved analytically, the other one is solved numerically (by integration). The main steps of the algorithm can be seen in Fig.3.15. The output is a surface image of the Sun, where each pixel stores the value of the area extension in that point. This image (data array) can be combined with the metadata of the corresponding AIA map (where pixels values are related to brightness) to create a surface map, which takes into account the solar 3D nature. The creation of a surface map is a very time demanding process and, if applied to every map in the dataset, would provide similar results, since the only difference from map to map is in the *rsun_ obs* metadata keyword, but is really small. For this reason, it was decided to compute only one surface map and then apply each dimming map on top of it as a mask. By summing the values of pixels p_i identified by the mask $D_n(p_i, t_n)$ at every time instant t_n, the instantaneous dimming area is retrieved:

$$A_{inst}(t_n) = \sum A(p_i, t_n) D_n(p_i, t_n) \tag{3.12}$$

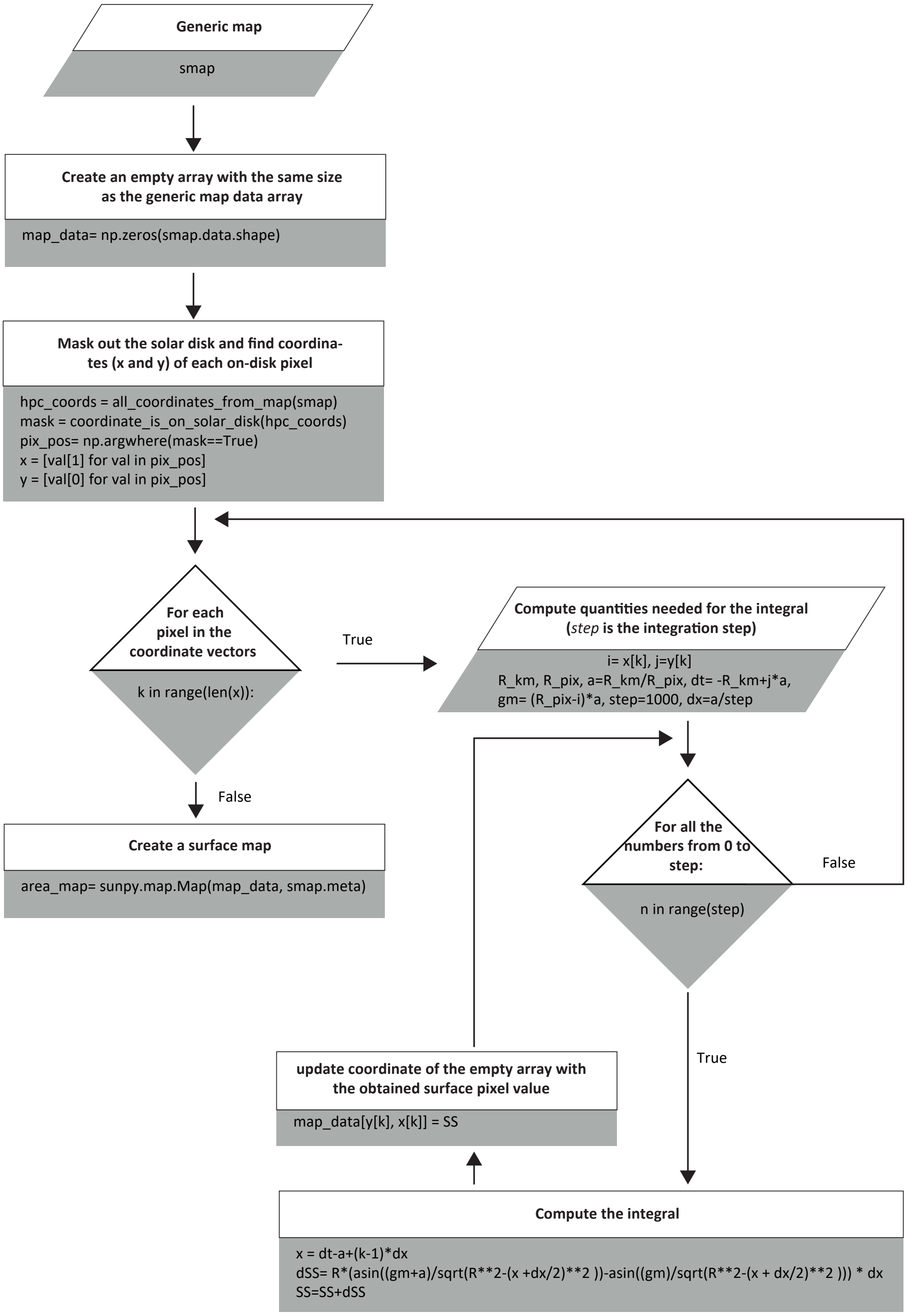

```
smap
```

```
map_data= np.zeros(smap.data.shape)
```

```
hpc_coords = all_coordinates_from_map(smap)
mask = coordinate_is_on_solar_disk(hpc_coords)
pix_pos= np.argwhere(mask==True)
x = [val[1] for val in pix_pos]
y = [val[0] for val in pix_pos]
```

```
k in range(len(x)):
```

```
i= x[k], j=y[k]
R_km, R_pix, a=R_km/R_pix, dt= -R_km+j*a,
gm= (R_pix-i)*a, step=1000, dx=a/step
```

```
n in range(step)
```

```
area_map= sunpy.map.Map(map_data, smap.meta)
```

```
map_data[y[k], x[k]] = SS
```

```
x = dt-a+(k-1)*dx
dSS= R*(asin((gm+a)/sqrt(R**2-(x +dx/2)**2 ))-asin((gm)/sqrt(R**2-(x + dx/2)**2 ))) * dx
SS=SS+dSS
```

Figure 3.15: Flowchart of the algorithm to compute the area using the integral method. The white boxes contain a qualitative description of the steps, while the grey boxes contain lines from the code. Parallelograms indicate the variables defined for the algorithm, rectangles contain functions and diamonds contain conditions for loops.

3.4. Event selection

Four event cases, each relative to solar flares associated with a CME and occurring on solar disk, will be analyzed. For three of them, data are downloaded for a total time interval of 72 hours, while the remaining case is analyzed for a total of 48 hours, but with a higher cadence. All the cases are quite different from each other, be it for the location on the solar disk, the intensity of the flare, the number of successive eruptions in the chosen time interval or even the period of occurrence within the solar cycle. This is intentional, to guarantee that the extraction of the dimming region and of the parameter analysis is not biased due to the restriction of the research to a specific category of solar events. Even though for some of the cases there may be more than one eruption originating from the same AR, what matters the most is the first solar event of each sequence, hence each case is named after the date of occurrence of the first flare/CME event. A detailed description of each event will be presented below.

September 6 2011

On September 6, 2011 a X2.1-class flare, associated with a halo CME, was produced by NOAA AR 11283 at 22:20 UT.

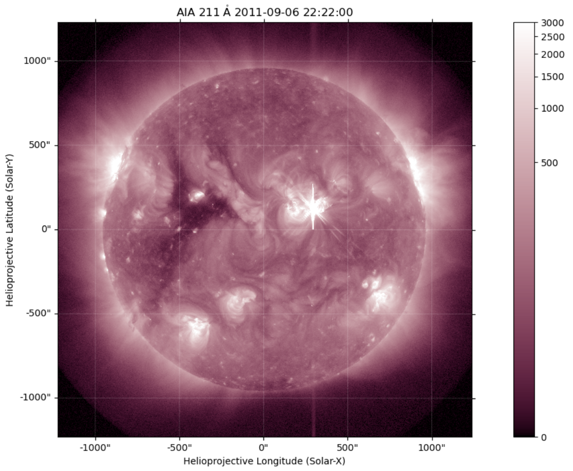

Figure 3.16: Image from AIA on September 06 2011 at 22:20 UT, i.e. the flare time. The AR is located in the upper right quadrant of the solar disk, where the star-shaped light (the flare) is.

About one day later, a second X1.8-class flare occurred at 22:38 UT and, lastly, a third M6.7-class flare took place on September 8 at 15:46 UT, originating from the same Active Region. The NOAA AR 11283 caught the attention of several scientists due to its strong activity with a total of 4 eruption in three-day interval happening when its location was close to the disk centre; hence numerous studies have already analyzed this AR and the related flares/CMEs (e.g., [77], [76], [122]) as well as the coronal dimmings ([33], [143], [115]). The first flare started at 22:12 UT and ended 11 minutes later, showing a peak of activity at 22:20 UT. Information about it can be retrieved in Tab.3.1, which also shows the basemap time and the fixed mask (maximum dimming) time. For what regards the other two flares, they are associated with a partial halo CME and a normal CME (angular width= 37°) [27], respectively.

This case is the only one that has been analysed for a time interval of 48 hours and the reason lies in its location. Even though being close to the Sun's center is a positive aspect (easy to observe), the AR is already in the right half of the plane, which implies reprojection effects because of the differential rotation applied to images taken after more than 2 days since the reference time (Chap.3.2.1). Thus, it was decided to limit the observation time to a few hours after the third flare occurrence so as not to suffer from this disturbance. Fig.3.17 shows the GOES x-ray flux (1-8 Åband) over the 3-days time interval. The solar flares are particularly evident and well-separated and their intensity is $> 10^{-4}$ W/m^2 for the first and second event and in the range between 10^{-5} and 10^{-4} W/m^2 for the third flare.

Date	Flare Class	Time (UT)					Time interval (min)
		Basemap	Start	Peak	End	Maximum dimming	
2011 09 06	X2.1	21:42	22:12	22:20	22:23	23:02	11

Table 3.1: September event main data: flare class, basemap time, time of the flare eruption (from start to end, including the peak time) and the total time interval of the solar activity.

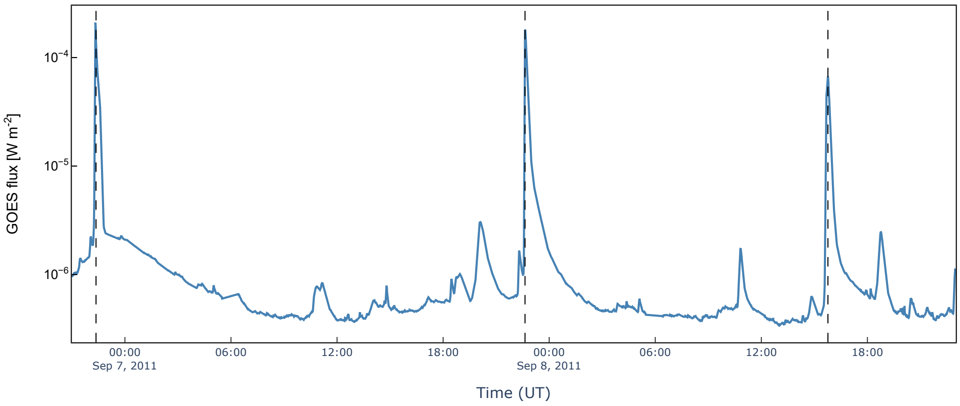

Figure 3.17: GOES (1-8 Å band) plot from September 6, 2011 at 21:00 UT to September 8, 2011 at 23:00 UT. The dashed line corresponds to each flare peak time that occurred within the time interval.

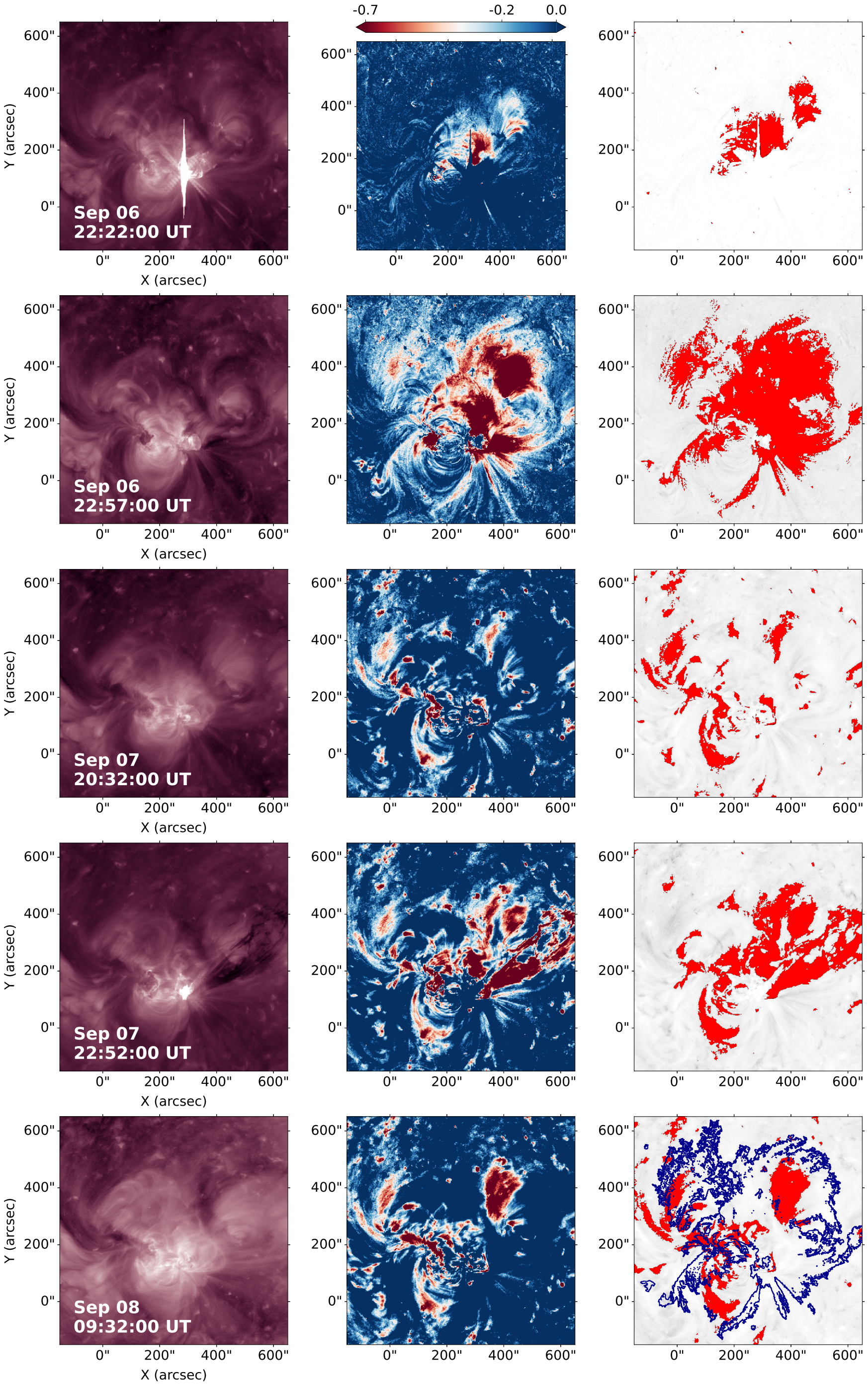

Figure 3.18: Evolution of coronal dimming region of the event on September 6 2011. *Left column*: time sequence of the SDO/AIA 211 Å during the dimming expansion. *Middle column*: Logarithmically scaled Base-Ratio (LBR) evolution of the dimming region. *Right column*: dimming pixel mask on top of the LBR image. In the *bottom right panel*, the contour of the fixed dimming mask is showed on top of the dimming mask.

Fig.3.18 shows five time instants out of the entire September dataset. It is possible to compare the original AIA images (in the left column) and the corresponding LBR image (in the middle column), plotted in a color palette that permits to easily visualize the changes in intensity. Pixels below -0.19 DN are coloured in white or reddish tones. It is also possible to visualize the instantaneous dimming masks (in red) plotted on top of the LBR images in gray scale (in the right column). The first three rows refer to the time interval between the first and second flare. The coronal dimming originated from the first flare expands towards North-East with an asymmetric pattern, meaning that during the flare more plasma has been ejected from the North part rather than the south part of the AR [112]. After reaching a peak, the dimming region seems to gradually disappear, but with the second eruptions dimming pixels are observed. In the last row, the contour of the fixed mask, according to the definition of Chap.3.3.3, is plotted on top of the instantaneous dimming mask. This helps in comparing the initial phase and the end of the analysed time range.

March 7 2012

2012 March is a very interesting period, being at the rising phase of solar cycle 24. During this month, a series of M/X class flares and big CMEs occurred.

In particular, NOAA AR 11429 generated five CMEs during the first two weeks of March. Among these, the CME occurring on March 7 is the largest and most energetic [92]. It is interesting to note that two flares occurred on March 7: one is a X5.4-class flare at 00:24 UT and the second is a X1.3-class flare at 01:14 UT [2]. In this case, the second CME is not visible because it was occulted by the first one, as it occurred close in time with the first one. For this thesis, the focus is on the first X5.4 flare/CME of March 7, to detect the dimming origin and evolution. During the 3-day interval of the analysis, also the M6.3-class flare/CME at 03:58 UT on March 9 is taken into account. The associated CMEs are halo CMEs. The active region is located in the North-West quadrant of the solar disk, not far from the western limbs.

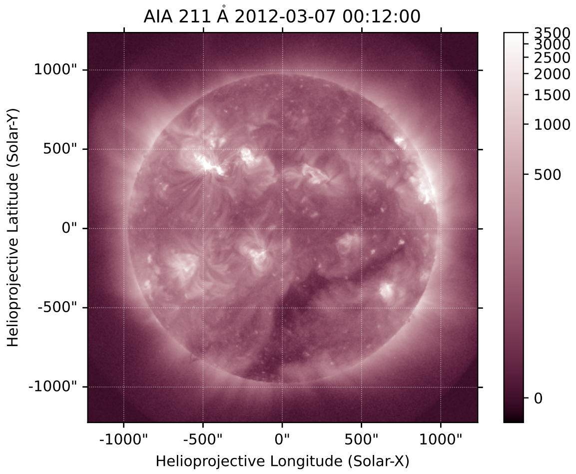

Figure 3.19: AIA image on March 7 2012 at 00:12 UT, i.e. a bit before the flare peaking time. The AR is located in the northern hemisphere.

It is possible to observe from the GOES plot in Fig.3.20 the strong intensity of the first flare and the subsequent spike rising in correspondence of the second flare, two days later. Tab.3.2 summarizes the relevant information for this case, while Fig.3.21 shows the original AIA image, the LBR image and the instantaneous dimming masks at five different time steps. The dimming is easily observable with bare eyes in the original images. Indeed, this dimming was the strongest coronal dimming event identified by SDO/EVE [145].

Date	Flare	Time (UT)					Time interval (min)
	Class	Basemap	Start	Peak	End	Maximum dimming	
2012 03 07	X5.4	2012 03 06 23:32	00:02	00:24	00:40	02:02	38

Table 3.2: March event main data: flare class, time of the flare eruption (from start to end, including the peak time) and the total time interval of the solar activity. The basemap time and the fixed mask time (maximum dimming within the first two hours from the eruption start time) are indicated too.

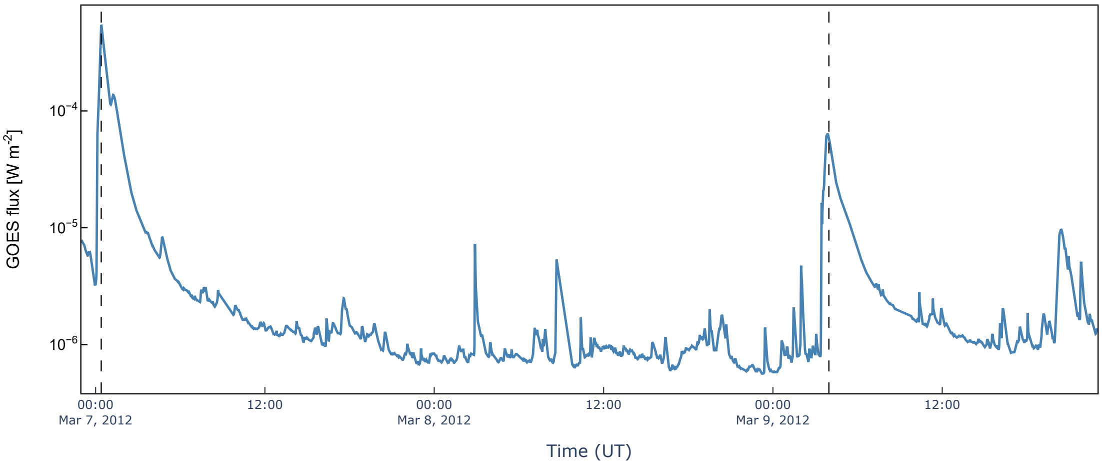

Figure 3.20: GOES plot (1-8 Å band) from March 6, 2012 at 23:00 UT until March 9, 2012 at 23:00 UT. The dashed line corresponds to each flare peak time.

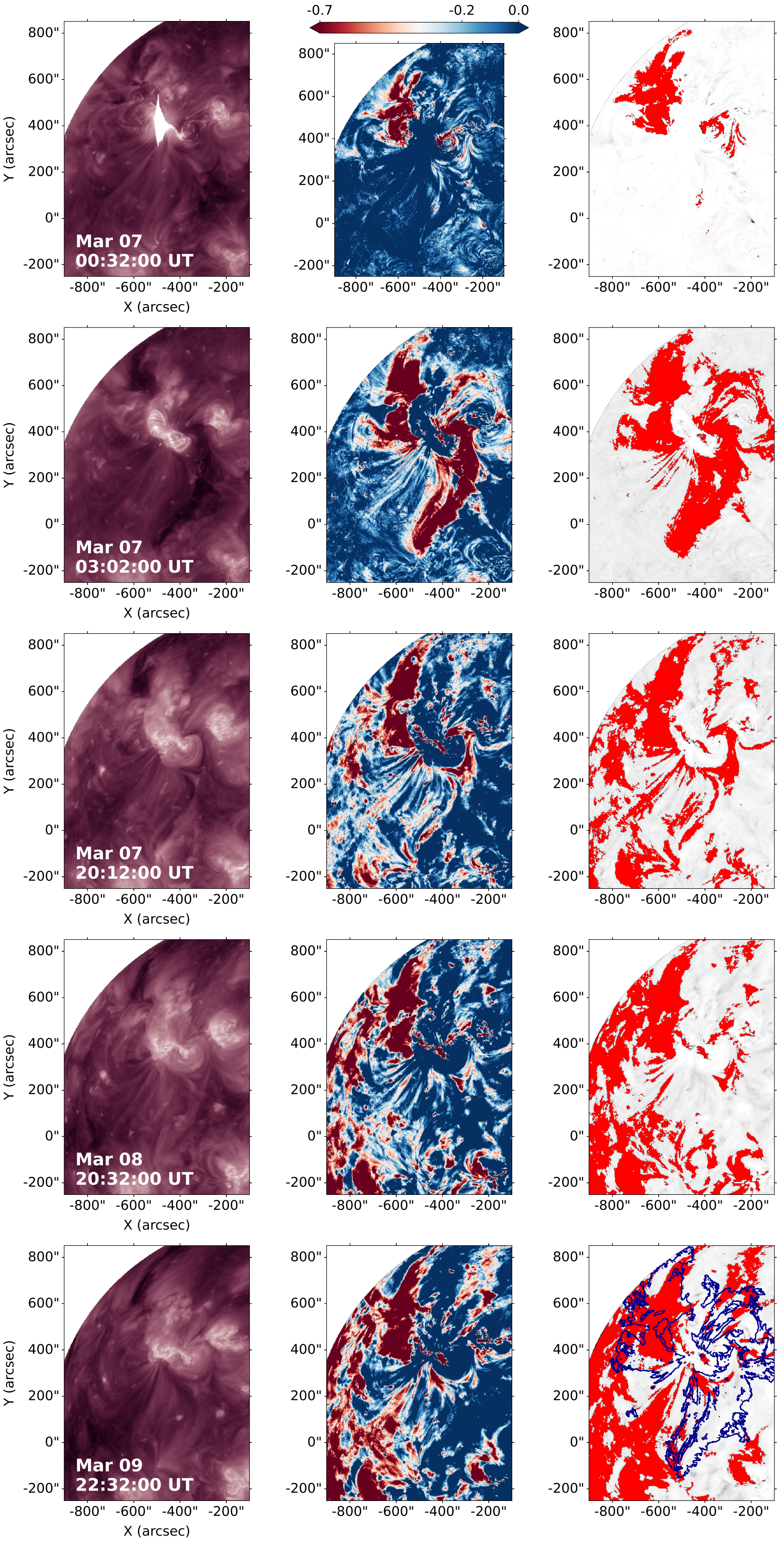

Figure 3.21: Same as Fig.3.18, but for March 7, 2012 case. It is possible to clearly see the dimming in the original AIA images at 03:02 UT.

June 14 2012

A long-duration M1.9-class flare, associated with a halo CME, originates from NOAA AR 11504 on June 14 at 14:35 UT.

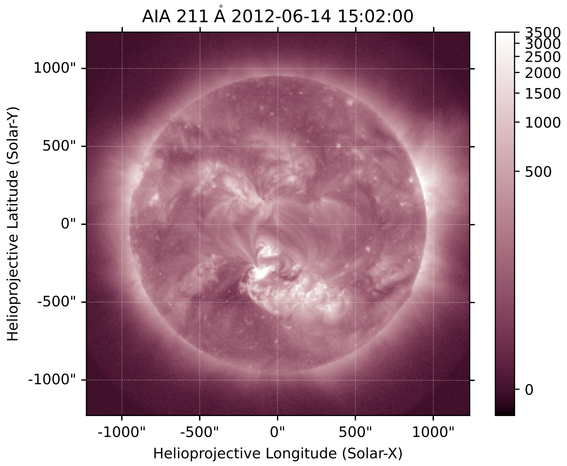

Figure 3.22: Image from AIA on June 14, 2012 at 15:02 UT, i.e. shortly after the flare peak time. The AR is located in the bottom half of the solar disk, slightly on the left.

June 2012 is at the beginning of the maximum of solar cycle 24.

The AR is located in the southern hemisphere, close to the center of the solar disk. This half of the solar disk is quite crowded with active regions and also a coronal hole (CH) can be seen on the left of the AR of interest. The flare/CME under study is the last out of the three eruptions originating from AR 11504, in a 3-day interval, and the strongest [81]. Tab.3.3 summarizes the relevant information for this case, while Fig.3.24 shows the original AIA image, the LBR image and the instantaneous dimming masks at five different time steps. In the column containing the original images, the proximity to the coronal hole is evident, while the instantaneous dimming masks in the right column show the effect of the distortion due to the differential rotation procedure as the detected dimming pixels move closer to the limb with the passing of time. Lastly, Fig.3.23 shows the GOES X-rays flux (1-8 Å band), where the first spike corresponds to the flare/CME under study, while the subsequent fluctuations are related to the dynamics of the surrounding ARs.

Date	Flare Class	Time (UT)					Time interval (min)
		Basemap	Start	Peak	End	Maximum dimming	
2012 06 14	M1.9	12:22	12:51	14:35	15:56	14:52	185

Table 3.3: June event main data: flare class, time of the flare eruption (from start to end, including the peak time) and the total time interval of the solar activity.

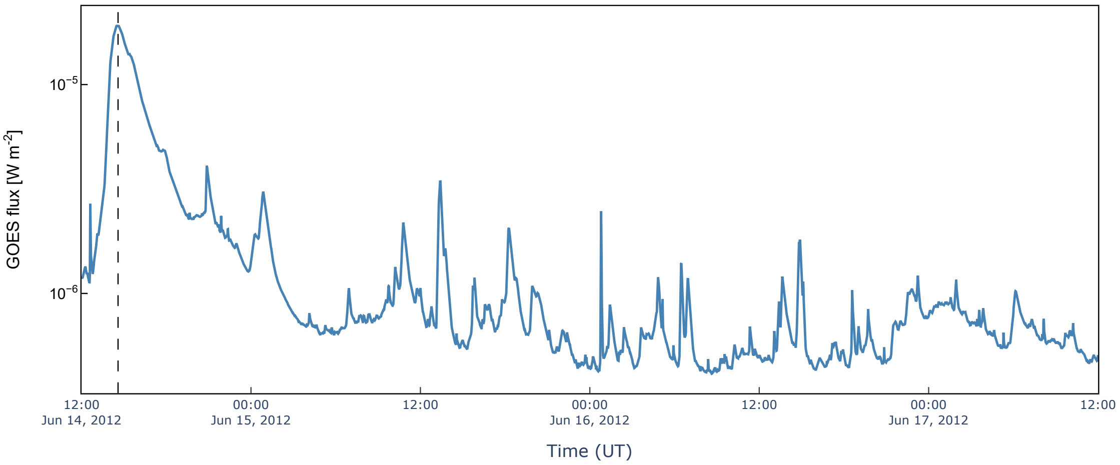

Figure 3.23: GOES plot (1-8 Å band) from June 14, 2012 at 12:00 UT until June 17, 2012 at 12:00 UT.

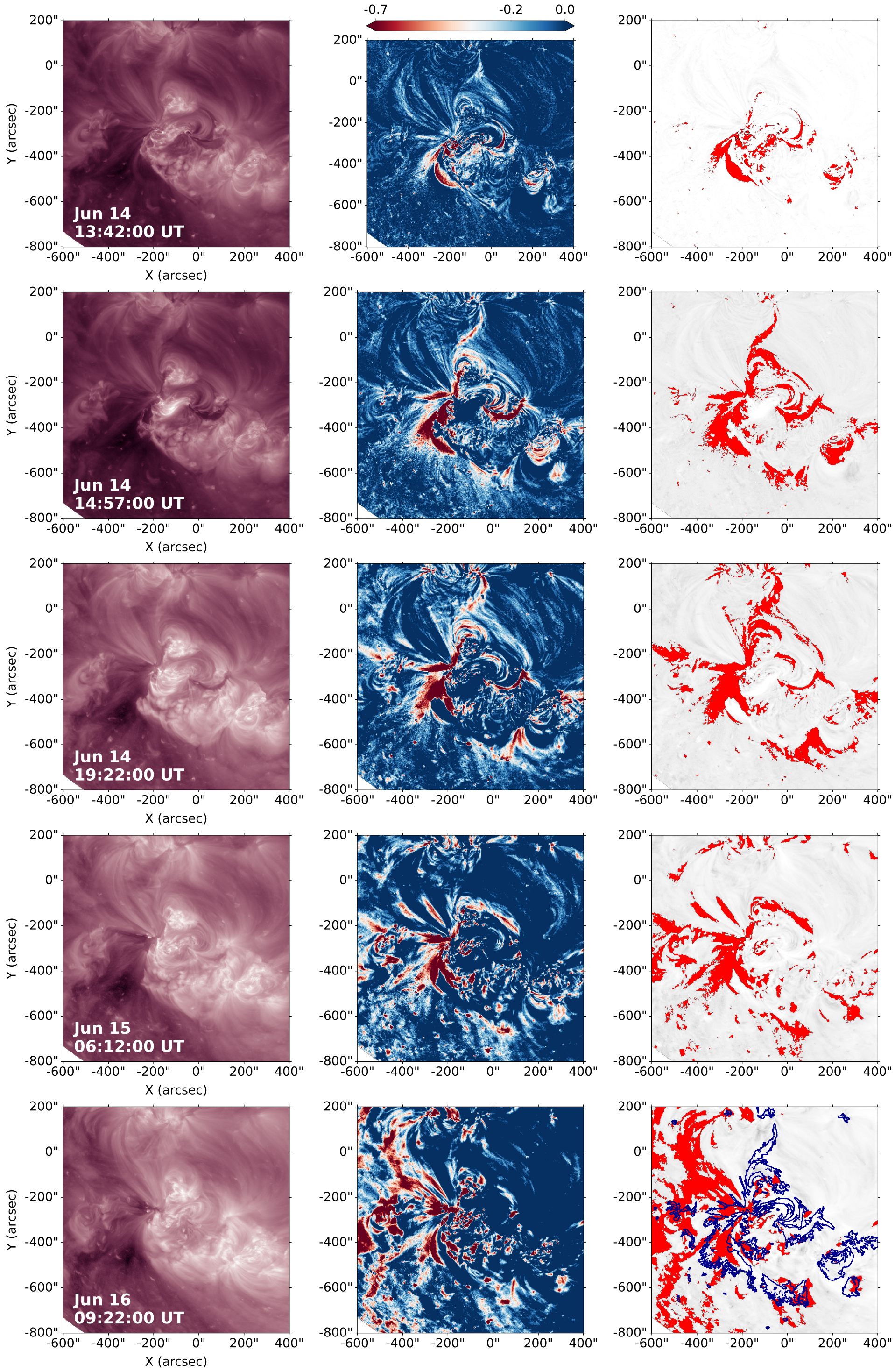

Figure 3.24: Same as Fig.3.18, but for June 14 2012 case.

March 08 2019 - International Women's Day event

A double-peaked C1.3 flare occurs on March 8 at 03:07 UT and a second B6.2 flare occurs on March 9 at 12:26 UT. They originated from active region AR 12734 and are associated with a CME each. Because of the peculiar date of the flare occurrence, this event has been studied as the International Women Day's event [39] and the related case in this thesis will be named after it. Women Day's event occurred during the minimum between solar cycle 24 and 25.

The AR is located in the upper half of the solar disk, at the center. The flares are chacterised by a low GOES flux, however the first flare caught the attention of the scientists because it is associated with several phenomena distinctive of solar eruptions: coronal dimmings, two EUV waves, type II and III bursts, and two coronal loop ejections, coming in "pairs" [39]. The two stages of the first flare can be divided in an interval going from 03:07 to 03:20 UT and another one going from 03:20 UT on. Fig.3.23 shows the GOES X-rays flux (1-8 Å band), where two peaks can be observed in correspondence of the first flare's spike, with one peak around 03:18 UT and the other around 03:37 UT. Tab.3.4 summarizes the relevant information for this case, without differentiating between the two stages. Fig.3.27 shows five different time instants of the data set and the evolution of the dimming. In particular, the dimming is composed by two extended regions, at the eastern and western edges of the AR, respectively. These positions correspond to the location where the flare ribbons terminate [39]. The evolution of the dimming shows a distinct two step behavior, pointing at two eruptions. In fact, the western dimming region grows first,between 03:10 and 03:16 UT, and is co-temporal with the impulsive phase of the first flare peak, while the eastern one develops in a more gradual way, until an impulsive increase of the region from 03:32 to 03:38 UT, which is simultaneous with the second peak of the derivative of GOES flare emission [39].

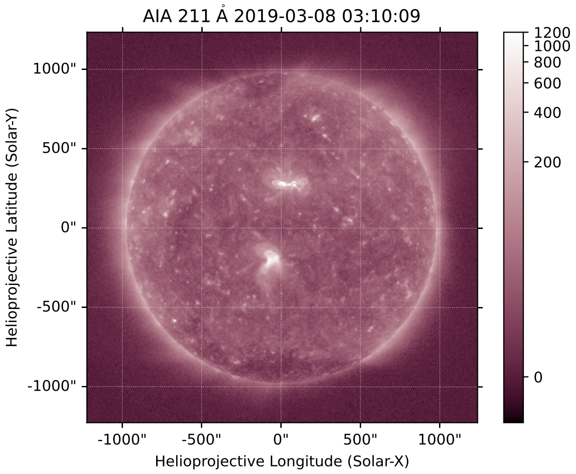

Figure 3.25: Image from AIA on March 8 2019 at 03:10 UT, i.e. a right after the flare peaking time. It is possible to observe that the intensity of the pixels on the colorbar has a maximum at 1200 DN, which is quite low compared to the previously described events.

Date	Flare Class	Time (UT)					Time interval (min)
		Basemap	Start	Peak	End	Maximum dimming	
2019 03 08	C1.3	02:40	03:07	03:18	03:58	04:25	51

Table 3.4: Women's Day event main data: flare class, time of the flare eruption (from start to end, including the peak time) and the total time interval of the solar activity. The basemap time and the fixed mask time are indicated too.

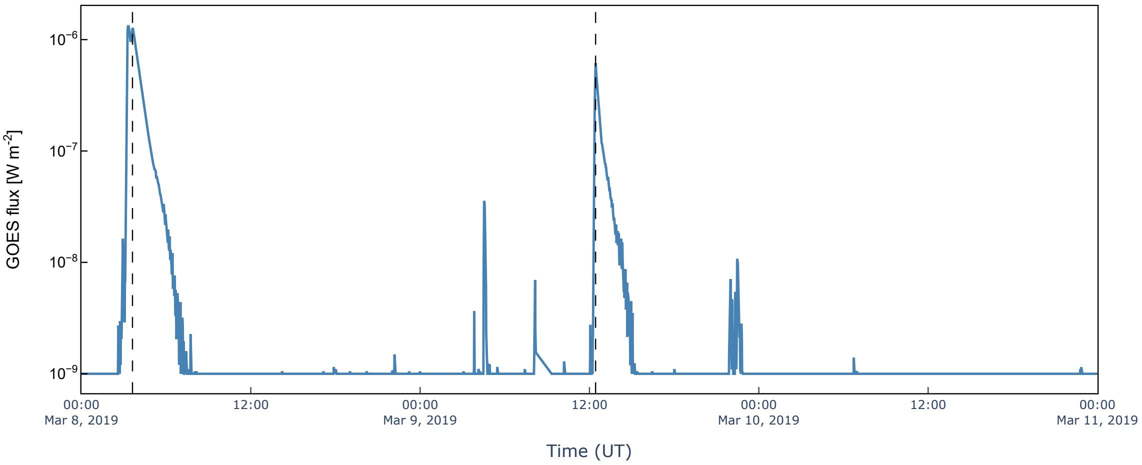

Figure 3.26: GOES plot (1-8 Å band) from March 8, 2019 at 00:00 UT until March 11, 2019 at 00:00 UT.

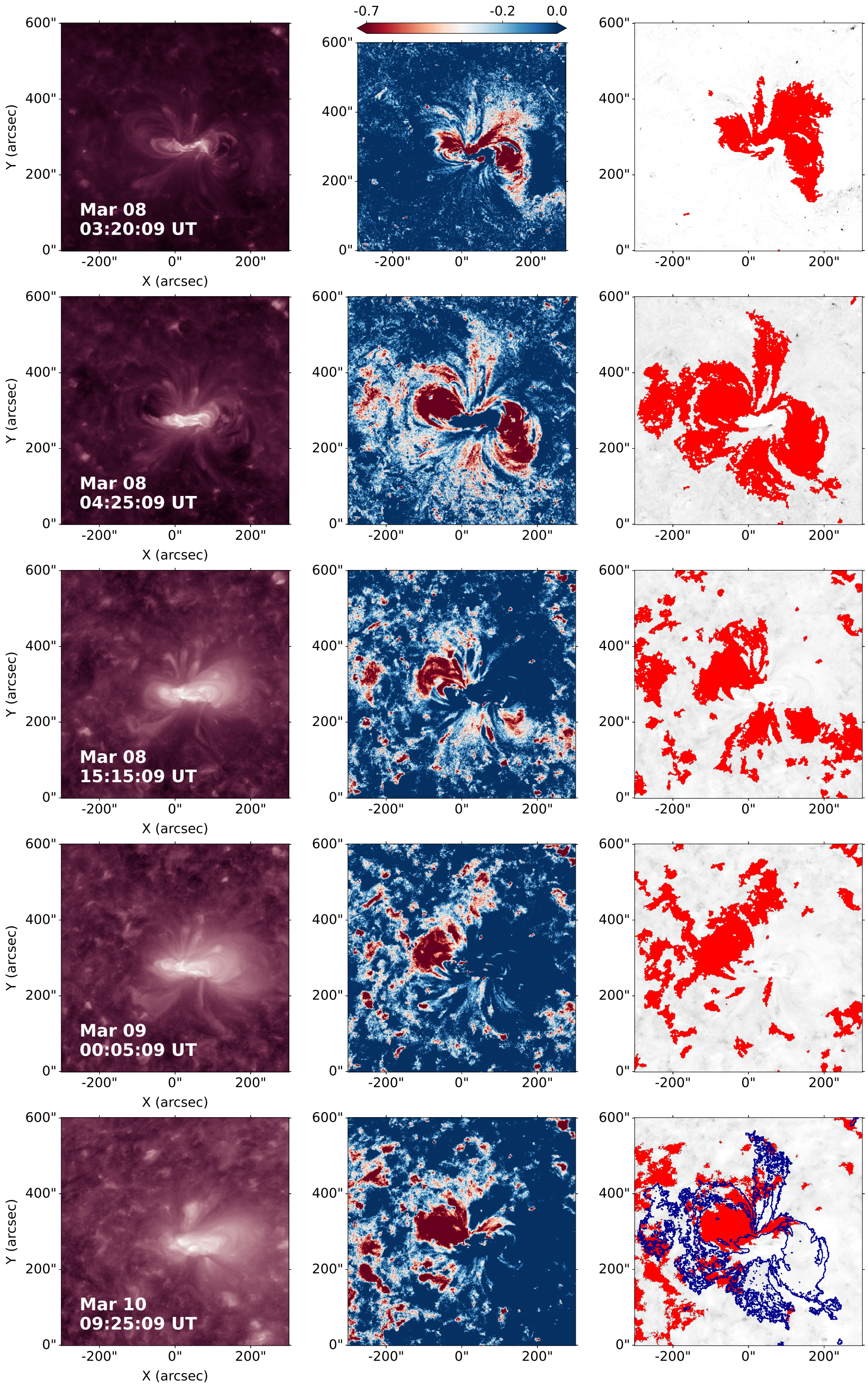

Figure 3.27: Same as Fig.3.18, but for March 8 2019 case.

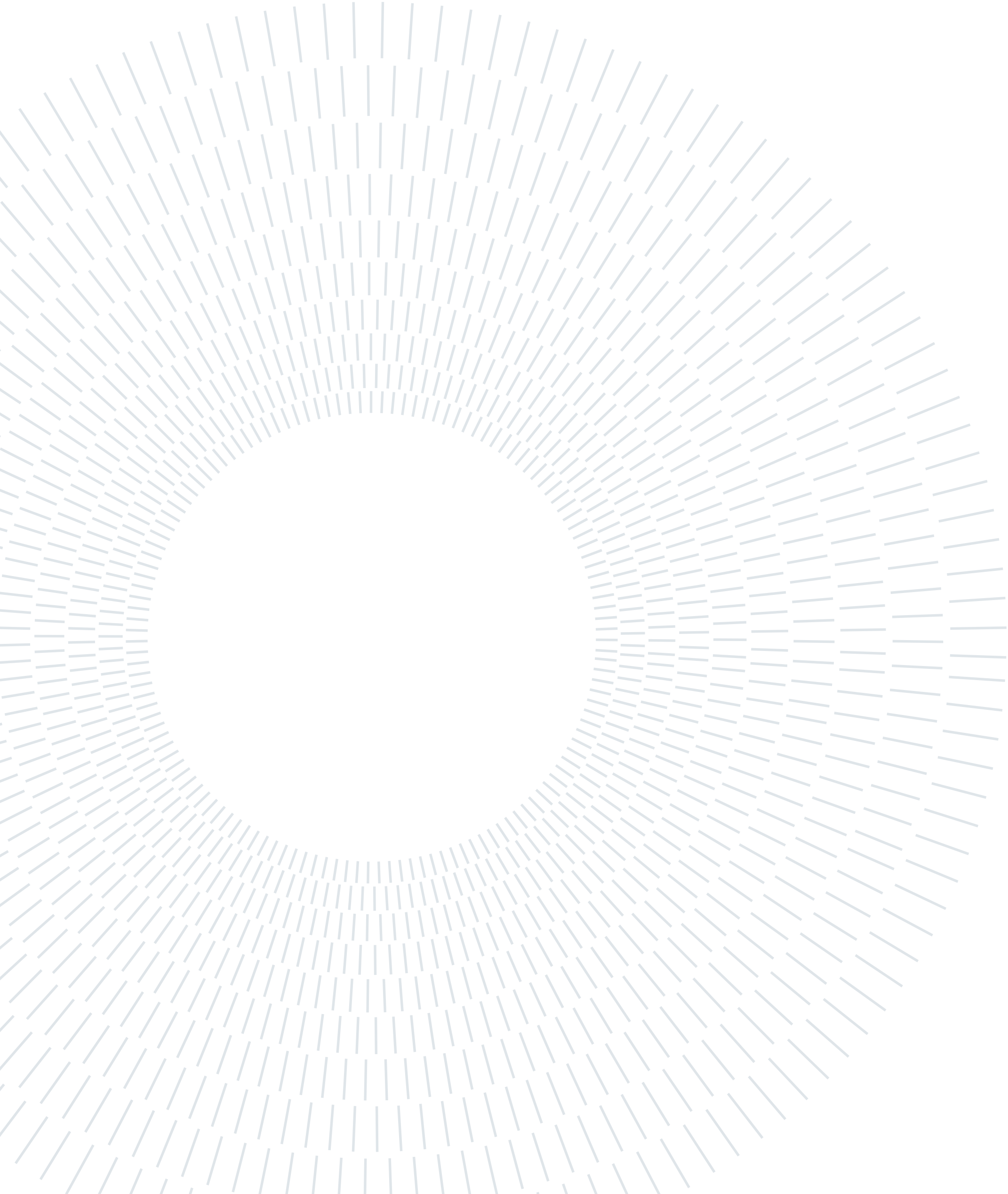

4 | Results

In the next paragraphs, the results regarding the performed analysis will be presented for each event. A comparison between the different methodologies to investigate the dimmings lifetime is shown and data from the STEREO mission are used to further interpret the obtained results.

4.0.1. September 6 2011

The outcome of the analysis for September case is shown in Fig. 4.1. The four images contain the GOES soft X-ray flux (panel a), the dimming instantaneous area A_{inst} (panel b), the dimming instantaneous brightness I_{inst} (panel c) and the instantaneous brightness $I_{f.m.}$ of the region within the fixed mask (panel d). Panels (b) and (c) also contain a comparison of instantaneous area and brightness between data from SDO and STEREO satellites.

For the instantaneous brightness, it is immediate to observe when the dimming reaches its peak values: there is a minimum in intensity right after each solar flare for a total of 3 relative minimum values. In particular, after the first two flares, the intensity drastically decreases and, right after the minimum is reached, a steep recovery trend is visible. However, it appears that the dimming related to the first flare recovered only about 70% in intensity: the sharp, fast recovery behaviour is followed by a steady trend until the second flare takes place. A similar behaviour occurs for the second eruption, but after a steep recovery, the dimming appear to decrease in intensity until reaching the relative minimum, shortly after the third flare. Since a minimum in intensity can be due to a maximum in the dimming expansion or a minimum in intensity of the dimming pixels [34], the area evolution over time is used to better understand the dimming evolution. It can be noticed that the maximum absolute values of both area and intensity are co-temporal . Overall, also the dimming instantaneous area did not show a complete recovery during the entire time interval.

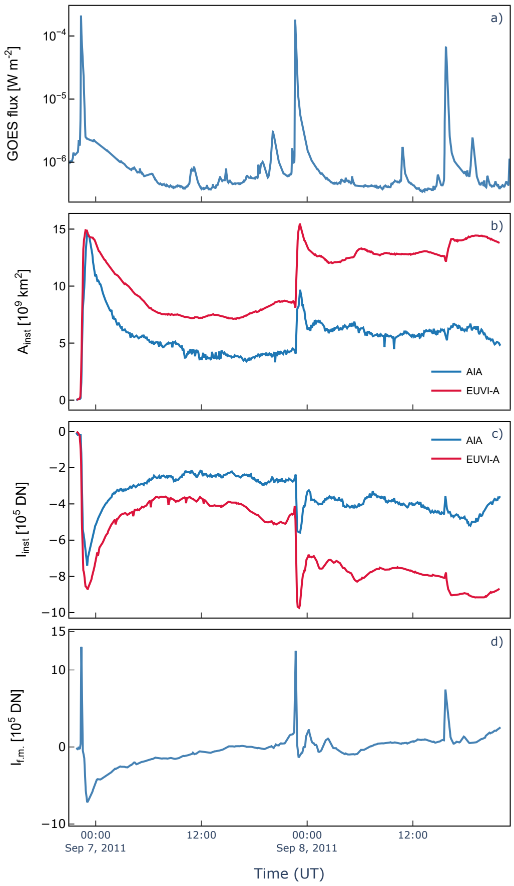

Figure 4.1: Time series (48 hours) of September 06 2011. *Panel a*: GOES 1-8 Åsoft X-ray flux. *Panel b*: Instantaneous dimming area. *Panel c*: Instantaneous dimming brightness. Panels (*b*) and (*c*) show a comparison between SDO/AIA (*in blue*) and STEREO/EUVI-A (*in red*). *Panel d*: Instantaneous brightness within the fixed mask.

In addition, data from EUVI-A, onboard STEREO satellite are employed for a comparison with the results obtained from AIA. Fig.4.2 shows snapshots of the evolution of the first 24 hours of the event, from both the STEREO point of view and the AIA one. In the first four columns (from the left to the right), images from STEREO are displayed: the original image, the BD image, the LBR image and the dimming mask. The last column of the figure (far right) shows the instantaneous dimming mask obtained from AIA and applied on top of the corresponding BD image.

Overall, data obtained from EUVI instrument show a similar trend to the ones obtained from AIA, particularly in the steep decrease (increase) in brightness (area) curve after the flare, which reaches the maximum (minimum) value at almost the same time. Even when using data from EUVI-A there is no observation of the dimmings' complete recovery. By looking at these two panels, it appears that the coronal dimming does not recover by the end of the observation time, being present even after 24 hours and being then influenced by the other two flares/CMEs. At the end of the data set there is no final recovery of the solar corona to the pre-eruption state.

Lastly, Fig.4.1-d shows the behaviour of the instantaneous brightness within the fixed mask. In this case, both dimming and non-dimming pixels are present inside the selected region, hence bright pixels belonging to the flare emission strongly contribute to the total intensity. Indeed, the three flares/CMEs appear like three spikes and, after the first one, a sharp decrease in brightness is observed, until the minimum which is co-temporal with the maximum extension of the dimming region as designed.

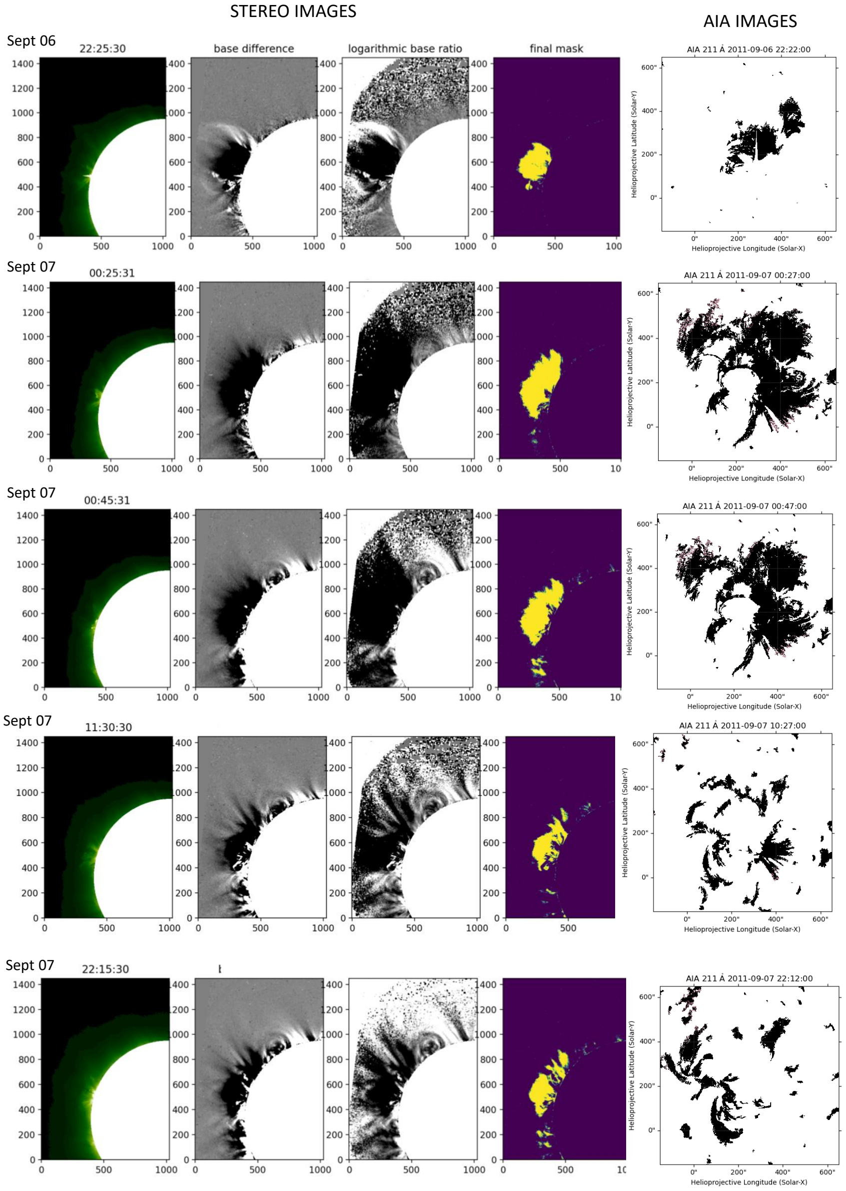

Figure 4.2: Snapshots of the September 6, 2011 case. Evolution during the first 24 hours seen from STEREO (*first four columns, from left to right*: original, BD and LBR images, and instantaneous dimming masks.) *Right column*: instantaneous AIA dimming mask on top of the corresponding AIA BD image (the non-dimming pixels are masked out).

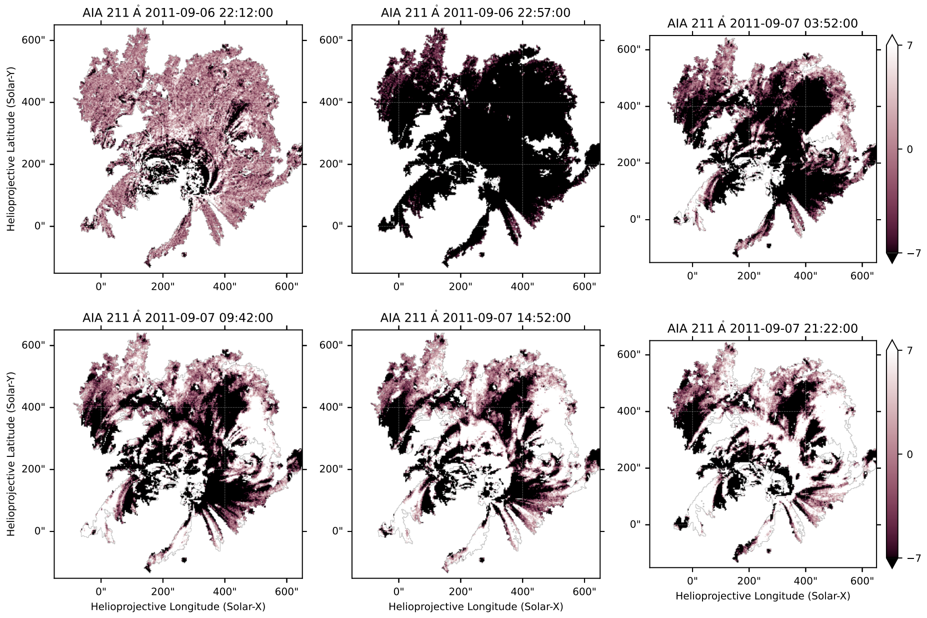

Figure 4.3: Fixed mask applied on top of the BD image at six different time step, from the beginning of the eruption until almost one day later. The non-dimming pixels are masked out. The average brightness recovers around 15:00 UT on September 7 and an overall balance between bright and dark pixels can be observed in the corresponding image.

The fixed-mask approach indicates an interesting evolution, since it shows a complete recovery of the average brightness on September 7 at 14:57 UT.

Even when the second flare on September 7 occurs, it does not affect much the intensity within the fixed region previously identified. One reason could be because the first dimming expanded mostly towards the North-West of the eruption site, while the second one expanded both in that direction and towards North-East, thus forming partially outside of the region-of-interest. The portion of the second dimming that remains inside the fixed mask is smaller compared to the first dimming extension, so the average brightness of the fixed region oscillates around the zero value, since both dimming pixels and bright pixels are present. By comparing the results from the plot with the original images in Fig.4.3, it is possible to observe that the dimming recovers gradually from its outer edges inward and towards the center. By looking at the figure, it is also of note that the dimming region located the furthest away from the eruption center, is the first to recover, while some dark dimming regions still linger close to the centre of the eruption. This is investigated further by specifically analyzing the recovery behaviour of secondary and core dimming regions by applying the 3 × 3 pixels boxes approach. Fig.4.4 shows a LBR map during the impulsive dimming phase with four colored small squares indicating where the boxes have been positioned. The yellow, red and blue boxes are located in proximity to the eruption centre; their goal is to investigate the ongoing dynamics of that area that contains candidates of core dimming regions. On the contrary, the pink box is positioned in the middle of the darkest and furthest away dimming region, most likely a secondary dimming region with a magnetic plage region, to keep track of the intensity behaviour in that area.

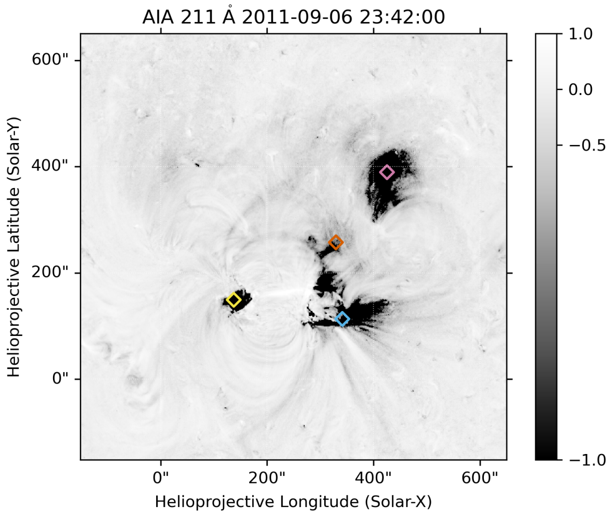

Figure 4.4: September 6 2011, 23:42 UT. Four boxes of size 3x3 pixels are located on top of the LBR image. The greyscale is in logarithmic scale to better visualize the darkest pixels. *Box 1*: yellow marker. *Box 2*: pink marker. *Box 3*: red marker. *Box 4*: light blue marker.

The evolution over time of intensity obtained from the sum of the pixels inside each box is shown in Fig. 4.5. What appears immediately is that box 2 and box 3 are the ones showing a complete recovery. When looking closer at the evolution of the original, BD and LBR images, it can be seen that there are post-flare loops gradually expanding into/towards the dimming region of box 3. Thus, this recovery can be considered as a projection effect due to the line-of-sight integration of these loops on top of the dimming region. On the contrary, box 2, in the secondary dimming area, is related to the stretching of the overlying field. This region recovers the fastest to its pre-event intensity and shows a linear, gradual recovery behaviour. For what regards box 1, its nature is more complex. At the beginning, it shows a similar recovery rate as box 3 and a possible reason might be that the same post-flare loops are expanding in this region, but from the opposite site, however it stays darker after that. The region, where the box is located, shrinks by the expansion of flare ribbons into it, which could be indicative of reconnection between the overlying field and the erupting flux rope. Lastly, box 4 shows a weaker recovery in intensity during the first 12 hours after the CME, especially when compared to box 2. This result is in agreement with Attrill et al. 2008 [7] (see Chap.2.2.2) and hence it makes sense to classify this dimming area as core dimming region, from an observational point-of-view. However, it should be noted, that this region might not represent the footpoints of an erupting flux rope in a classical sense.This box is localized within a dimming region that is hypothesized to contain field lines that opened up during the eruption [115]. Combining observations and MHD simulations, Prasad et al. 2020 ([115]) found that this dimming region is co-spatial with the footpoints of the dome surface of a 3D magnetic null point. A causal connection between the magnetic reconnections at the 3D null and the dimming, due to transformation of field lines of the inner spine to open field lines of the outer spine, was concluded in this study.

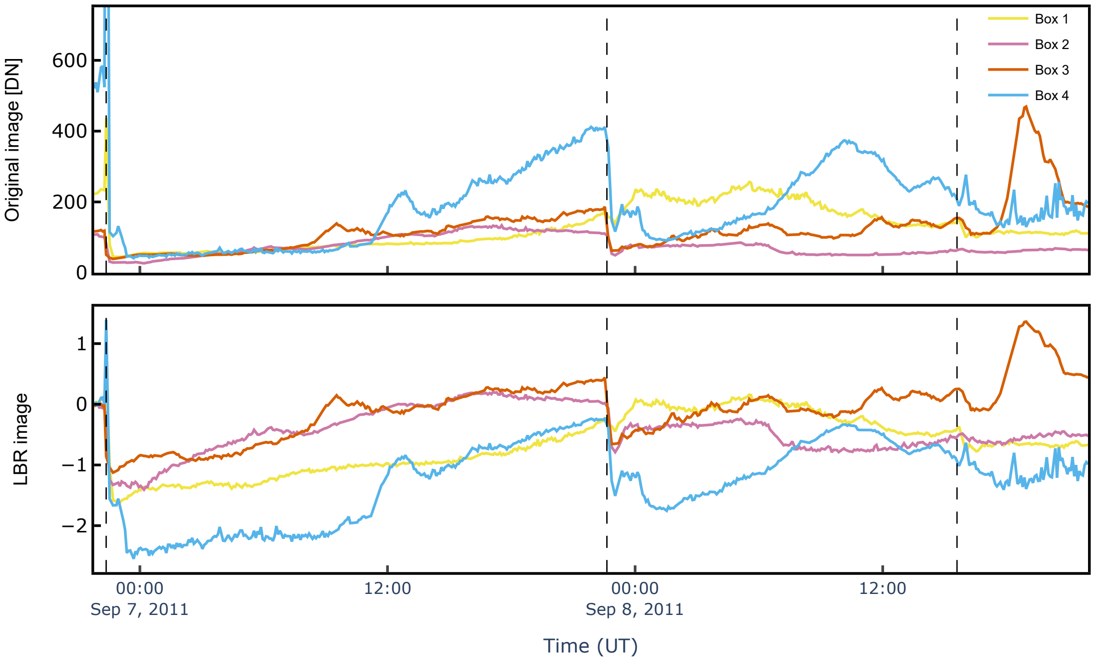

Figure 4.5: Comparison of the brightness behaviour for each of the chosen 3x3 pixel box showed in Fig.4.4. Dashed line is the peak time of each flare. *Top*: intensity evolution from the original AIA images. The y axis is reduced to enable a comparison of the four curves. Note that the intensity of box 4 at the first flare time is over 2000 DN. *Bottom*: intensity evolution from the LBR images.

4.0.2. March 7 2012

In a similar way to what is done for the September case, the results for March 7, 2012 are shown in Fig.4.6. The GOES flux (1-8 Å band) helps in visualizing the time of occurrence of the flares/CMEs. From the instantaneous dimming and brightness curves (panels (a)

and (c)), it is possible to notice a continuous growth of the dimming area accompanied by a decrease in brightness, with both SDO/AIA and STEREO/EUVI data.

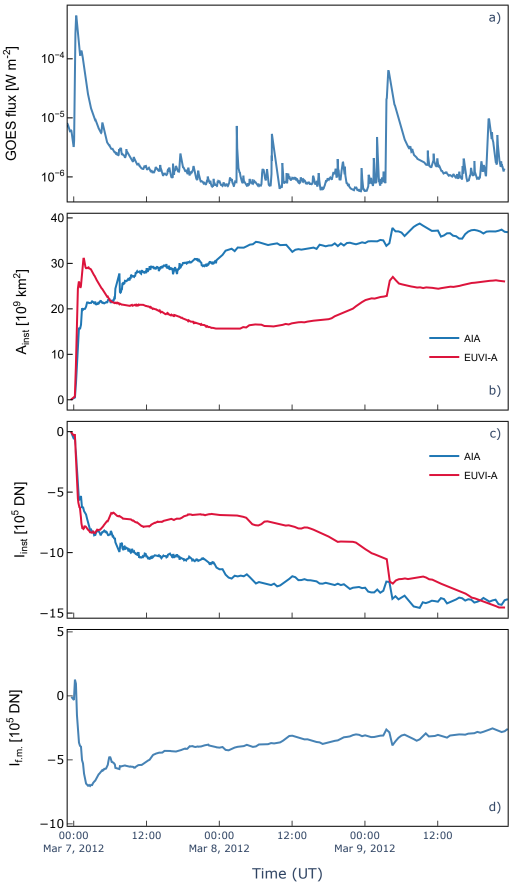

Figure 4.6: Same as Fig.4.1 but for March 7, 2012 (72 hours).

It appears that the dimming that is formed after the flare/CME on March 7 does not recover after two days but continues to grow and, when the flare/CME on March 9 occurs, this trend is perpetuated. It is interesting that a similar behaviour is seen in the data of both the AIA and EUVI instrument, especially in the sharp increase (decrease) of area (brightness) and in the overall decreasing of the instantaneous brightness. However, there is a difference: STEREO/EUVI data indicate a shrinkage of the dimming area, which is accompanied by a mild recovery trend, then followed by an almost steady instantaneous brightness until the second flare time, which results in a further decrease in instantaneous intensity and growth of the area. On the contrary, data from SDO/AIA show a ceaseless growth in size and decrease in brightness. By checking the original images and the detected instantaneous dimming regions (Fig.4.7), it appears that the dimming expands close to the western limb, further increasing its size with the passing of time. The dimming region in the North-East is detected even at the end of the data set, while a huge amount of dimming pixels appears more to the South, alongside the limb. This behaviour is interpreted as an artifact of the differential rotation procedure due to the proximity of the cropped image to the eastern limb.

Therefore, using the fixed mask curve for the interpretation of this event is more reliable. By looking at this curve (Fig.4.6-d), the brightness does not recover. The second flare does not appear as a high and quick peak in intensity, in contrast to what happens for September case (Fig.4.1-d). This is partially due to the presence of dark pixels still being the majority inside the fixed mask, but also due to the bright light of the flare being outside the mask and not masking it, as it is in September case.

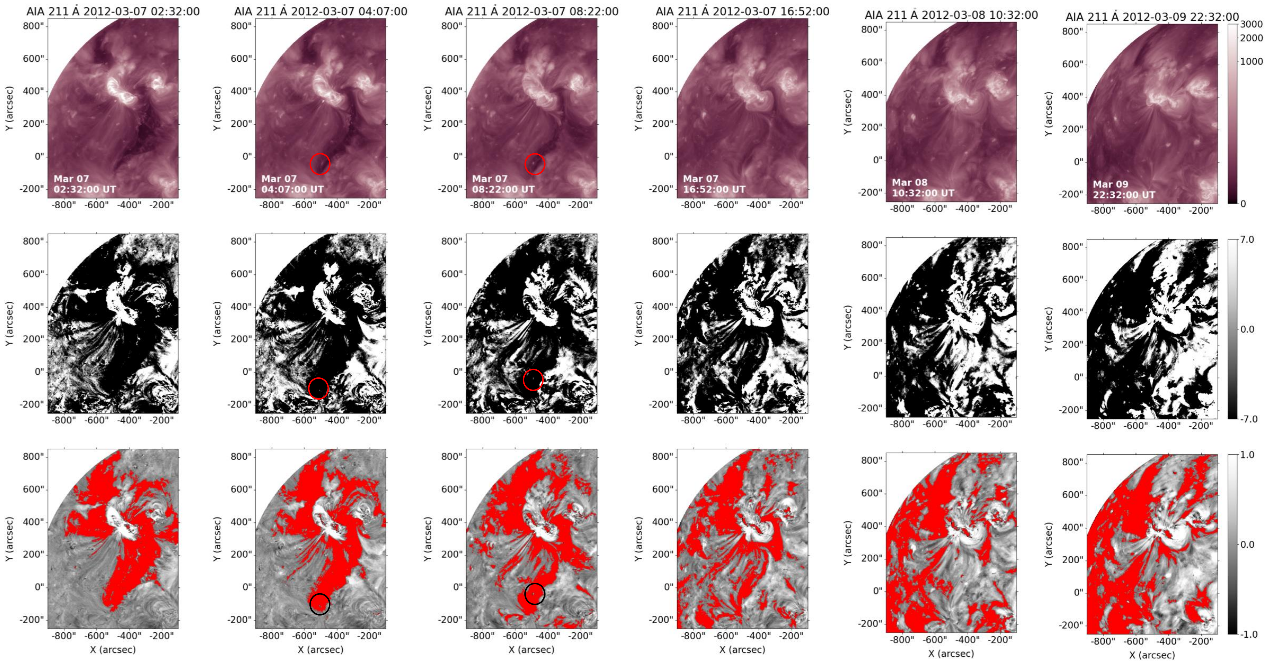

Figure 4.7: Snapshots of March 7, 2012 case. *Top row*: original AIA images in the 211 Å filter. *Middle row*: Base difference images. *Bottom row*: instantaneously detected dimming regions (*in red*) on top of the corresponding LBR images. The red circles in the images of the top row indicate brightenings that are emerging within the dimming region, which are detected visible also in the BD images (red circle) and in the images of the bottom row (black circles).

There is another interesting aspect of March case that is worthy to note. As already mentioned, the region in the North-East does not recover within the 72 hours of observation, but the region in the South does. In particular, it is found that the recovery does not happen only because of the boundaries shrinkage, but there may be some emerging flux from below that helps the refilling of the area: some brightenings are observed at some specific times inside the southern part of the dimming, e.g. on March 7, 2012 at 04:07, 05:42, 08:22 or 09:17 UT. Two of these time steps are shown in Fig.4.7, where a circle marks the brightenings position. They are observable in the original AIA image, but are also detected (or better, not detected) by the region growing algorithm, meaning that some bright pixels are actually appearing from underneath the dimming. The March case is the only case in this study where the recovery may not only be due to the shrinkage of the dimming regions themselves but also due to flux emergence and reconnection inside the regions.

4.0.3. June 14 2012

Results for June 2012 case are shown in Fig.4.8. Data from the STEREO/EUVI-B instrument to observe this event were not available because of the spacecraft's position with respect to the Active Region, hence data from EUVI-A are used.

There is a huge discrepancy in the data obtained using the instantaneous dimming masks from SDO/AIA and STEREO/EUVI (panels (*b*) and (*c*)). A complete recovery is observed by the latter, while the former shows an incessant growth of the dimming. Actually, June 14, 2012 case also suffers from the presence of artifacts related to the differential rotation procedure resulting in the erroneous detection of dimming alongside solar limbs. On the contrary, by limiting the analysis to the region within the fixed mask (panel (*d*)), it is possible to see that the behaviour of the corresponding intensity curve is more similar to the instantaneous brightness obtained with STEREO data. A complete recovery is registered around 03:40 UT and, after that, the average brightness shows an oscillating behaviour. A mosaic of images displaying the application of the fixed mask on top of BD images is shown in Fig.4.9.

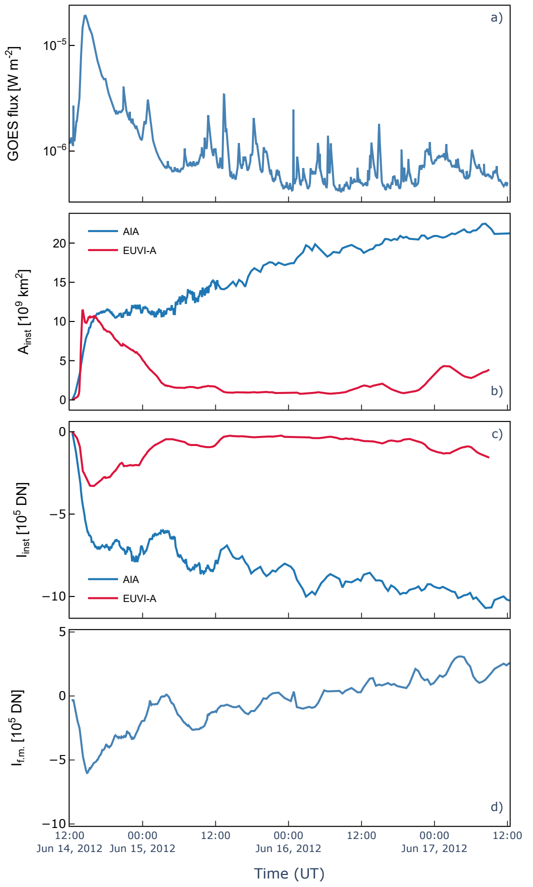

Figure 4.8: Same as Fig.4.1 but for June 14 2012 (72 hours).

By also looking at the original images, it can be concluded that there is some ongoing dynamics in active region of this event and its surrounding which makes the interpretation of this event challenging. This complex dynamics could be explained as ongoing reconnection activity, but further analysis, beyond the scope of this thesis would be required to prove that. The oscillating behaviour of the brightness evolution within the fixed mask also supports this interpretation, as dimming regions form over the course of the full 72 hour time range.

In addition, the proximity of the AR to the coronal hole (CH) makes things a bit more complicated, as it is partially responsible for the detection of darkenings on the right side of the image, mostly because bright loops that covered the CH prior to the CME, disappeared during the eruption. In addition, also jet-like features indicative of ongoing interchange reconnection are observed at the border of the CH.

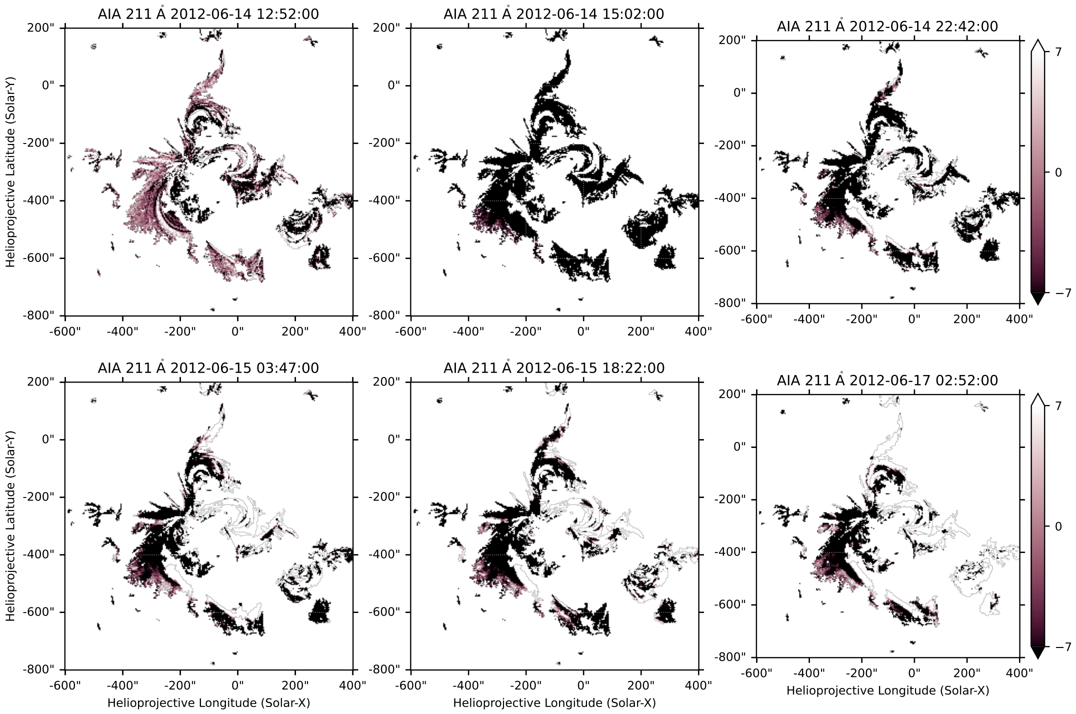

Figure 4.9: Same as 4.3, but for June 2012 case. Fig.4.8 indicates a recovery around 03:40 UT.

4.0.4. March 08 2019

Results for The Women Day case are shown in Fig.4.10. Data from STEREO/EUVI were not available for the entire duration of the analysis, but only for approximately 48 hours. In this case, the data of instantaneous brightness and area from AIA and EUVI show similarities and none of them exhibits a recovery.

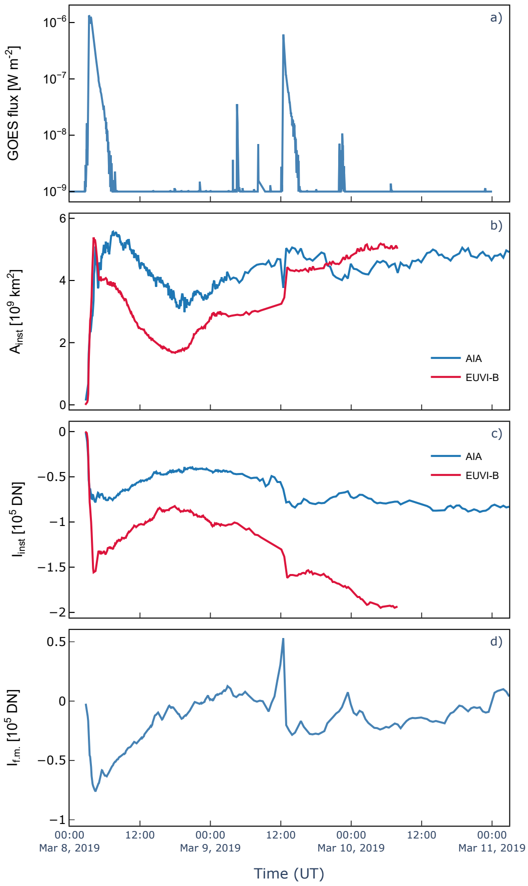

Figure 4.10: Same as Fig.4.1 but for March 08 2019 (72 hours).

A different situation is shown by the fixed mask brightness curve (Fig.4.10-d), where the bright emission of the second flare is evident and is then followed by a decrease in the average brightness, which recovers in a short amount of time. By checking AIA original images in both 211 Å and 193 Å, it looks like there are loops growing (especially in the right region) and it is concluded that the main recovery mechanism for these dimming regions might be simple loop refilling. An interesting observation about this case is related to the recovery trend of the southern secondary dimming, obtained from the pixel boxes 1 and 2 showed in Fig.4.11 and plotted in Fig.4.12. The two boxes are chosen close to each other to better follow the dynamics of the region and show a linear, gradual recovery behavior. This region recovers the fastest to its pre-event intensity. On the contrary box 3 is placed at the center of the left region of the dimming and shows a fast recovery, followed by an almost stationary intensity value until the second flare takes place. These results seem to be in accordance with what was suggested by Attrill et al. [7] (see Chap.2.2.2): it was possible to identify a long-lived part within the dimming which did not recover by the end of the data set, meaning that internal recovery is slower than the process occurring at the peripheral regions. Hence, box 3 could be part of a core dimming, while boxes 1 and 2 belong to the periphery.

In a recent study (see [39] for more details) the author did not distinguish between core and secondary dimmings, focusing mainly on the early evolution of the event. The present work could be integrated with their analysis, helping in the localization of different types of dimming.

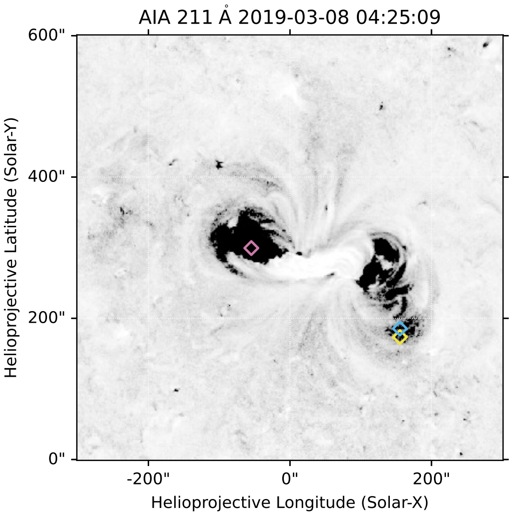

Figure 4.11: March 8 2019, 04:25 UT. Three boxes of size 3x3 pixels are located on top of the LBR image. The greyscale is in logarithmic scale to better visualize the darkest pixels. *Box 1*: yellow marker. *Box 2*: light blue marker. *Box 3*: pink marker.

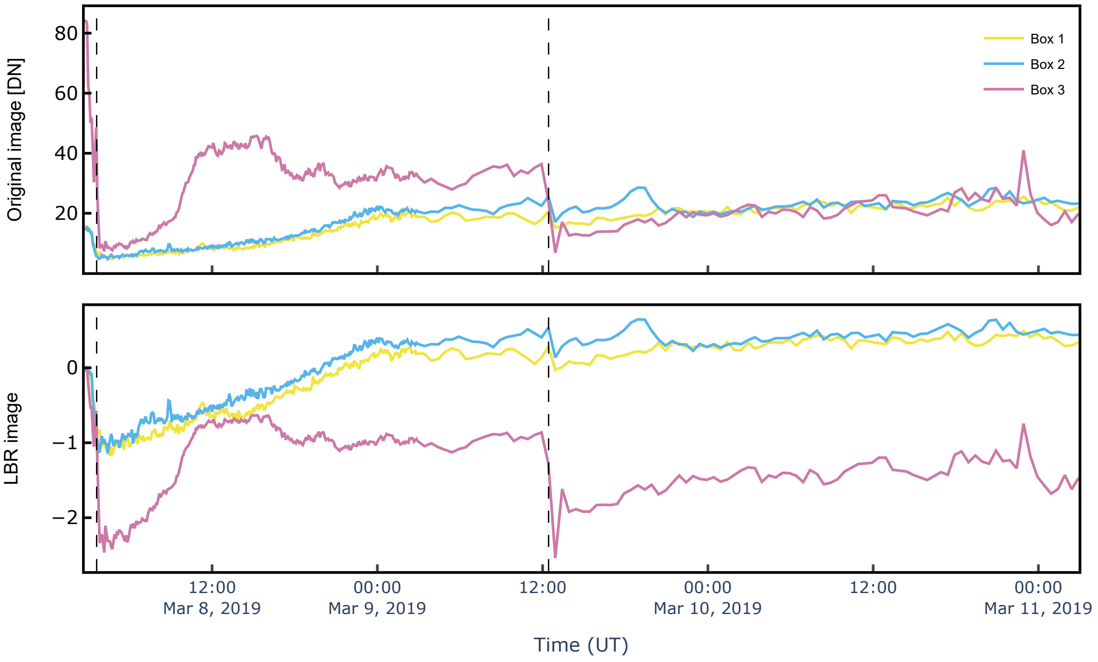

Figure 4.12: Comparison of the brightness behaviour for each of the chosen 3x3 pixel box showed in Fig.4.11. The dashed line marks the peak time of each flare. *Top*: intensity evolution from the original AIA images. *Bottom*: intensity evolution from the LBR images.

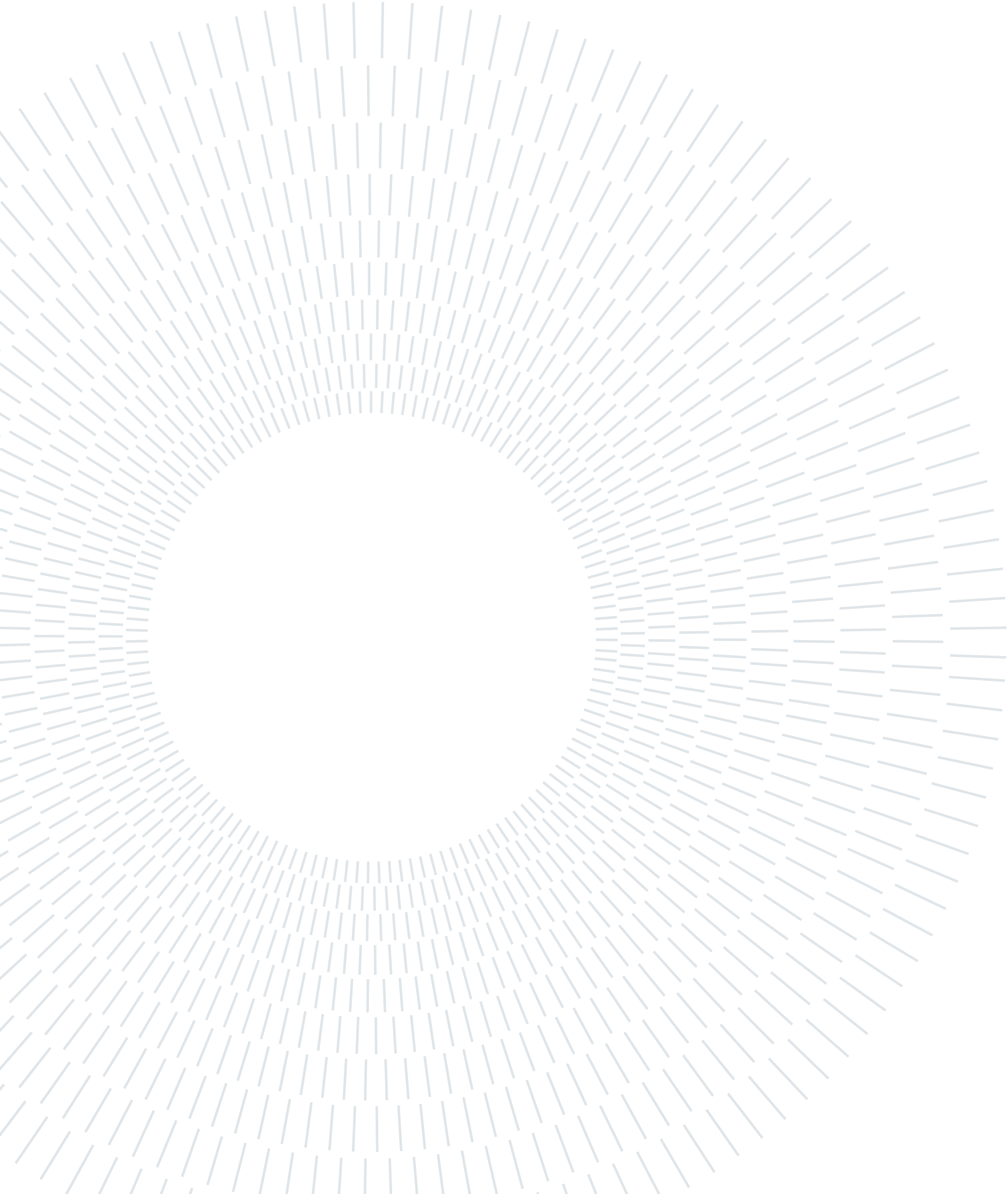

5 | Conclusions and future developments

The goal of this thesis is to analyze coronal dimming lifetimes, focusing mostly on their recovery phase, since its understanding could help in the comprehension of the reconnection dynamics occurring after a coronal mass ejection. It was found that dimmings tend to recover to the pre-eruptions state after a certain amount of time [118], but a distinction between the behaviour of core dimmings and secondary dimmings is to be taken into account ([7], [143]). In addition, the recovery mechanism is currently based on two possible explanations, one that supports a simple reduction of the dimming area, from the outer boundaries towards the center, and the other that suggests a replenishment of the plasma from inside the dimming region.

The purpose of the thesis was to conduct the analysis of the end-of-lifetime of the observed dimmings and extract information about if and how the dimming recovers and the amount of time needed to reach a complete recovery. The analysis has been performed in Python and algorithms for dimming detection and life time analysis have been developed and tested on the chosen set of events. The procedure for the analysis of on-disk solar events works with base-difference data and with the application of the region growing algorithm, to identify dimming pixels and retrieve the relevant dimming parameters, namely area and brightness. Limitations have been found in terms of observation time for events close to either West or East limb, because they are subjected to distortions and therefore artefacts due to differential rotation. New approaches have been identified to reduce the effect of these problematics, hence the decision of restricting the analysis to very specific regions, with the application of the maximum dimming area mask to the entire dataset or with the analysis of 3×3 pixel boxes located in regions of interest within the dimming. The obtained results show similarities with the work of [7], with the identification of core dimmings, showing a slow and sometimes not ended recovery, and secondary dimmings, located far from the center of the eruption, being the first regions to be recovered, with an almost linear, gradual trend. This work is a validation of the created tools and a preliminary analysis of these new investigation approaches. In the future, performing a systematic statistical analysis could be useful to quantify the recovery time of the coronal dimmings by using the fixed mask approach, while the pixel boxes method could be of help to understand the dynamics of different types of dimmings, possibly by integrating the knowledge of already-analysed events, but focusing more on the end of life of the dimming rather than its early evolution, like it has been done for the International Women's Day event [39].

Bibliography

[1] M. Acuña, D. Curtis, J. Scheifele, C. Russell, P. Schroeder, A. Szabo, and J. Luhmann. The stereo/impact magnetic field experiment. *Space Science Reviews*, 136 (1):203–226, 2008.

[2] M. Ajello, A. Albert, A. Allafort, L. Baldini, G. Barbiellini, D. Bastieri, R. Bellazzini, E. Bissaldi, E. Bonamente, T. Brandt, et al. Impulsive and long duration high-energy gamma-ray emission from the very bright 2012 march 7 solar flares. *The Astrophysical Journal*, 789(1):20, 2014.

[3] M. J. Aschwanden. Global energetics of solar flares. iv. coronal mass ejection energetics. *The Astrophysical Journal*, 831(1):105, 2016.

[4] M. J. Aschwanden, A. Caspi, C. M. Cohen, G. Holman, J. Jing, M. Kretzschmar, E. P. Kontar, J. M. McTiernan, R. A. Mewaldt, A. O'Flannagain, et al. Global energetics of solar flares. v. energy closure in flares and coronal mass ejections. *The Astrophysical Journal*, 836(1):17, 2017.

[5] R. Athay. The solar chromosphere and corona. *Physics Today*, 53, 11 1976. doi: 10.1063/1.3024520.

[6] G. Attrill, M. S. Nakwacki, L. Harra, V. Driel-Gesztelyi, C. H. Mandrini, S. Dasso, J. Wang, et al. Using the evolution of coronal dimming regions to probe the global magnetic field topology. *Solar Physics*, 238(1):117–139, 2006.

[7] G. Attrill, L. van Driel-Gesztelyi, P. Démoulin, A. Zhukov, K. Steed, L. Harra, C. H. Mandrini, and J. Linker. The recovery of cme-related dimmings and the icme's enduring magnetic connection to the sun. *Solar Physics*, 252(2):349–372, 2008.

[8] G. Attrill, L. Harra, L. van Driel-Gesztelyi, and M. Wills-Davey. Revealing the fine structure of coronal dimmings and associated flows with hinode/eis. *Solar Physics*, 264(1):119–147, 2010.

[9] G. D. R. Attrill and M. J. Wills-Davey. Automatic detection and extraction of coronal dimmings from sdo/aia data. *Solar Physics*, 262(2):461–480, 2010.

[10] E. H. Avrett. The solar temperature minimum and chromosphere. In *Current Theoretical Models and Future High Resolution Solar Observations: Preparing for ATST*, volume 286, page 419, 2003.

[11] B. Bein, S. Berkebile-Stoiser, A. Veronig, M. Temmer, N. Muhr, I. Kienreich, D. Utz, and B. Vršnak. Impulsive acceleration of coronal mass ejections. i. statistics and coronal mass ejection source region characteristics. *The Astrophysical Journal*, 738 (2):191, 2011.

[12] A. Bemporad. Stereoscopic reconstruction from stereo/euv imagers data of the three-dimensional shape and expansion of an erupting prominence. *The Astrophysical Journal*, 701(1):298, 2009.

[13] R. Bentely and S. Freeland. Solarsoft-an analysis environment for solar physics. In *Crossroads for European solar and heliospheric physics. Recent achievements and future mission possibilities*, volume 417, page 225, 1998.

[14] D. Bewsher, R. Harrison, and D. S. Brown. The relationship between euv dimming and coronal mass ejections-i. statistical study and probability model. *Astronomy & Astrophysics*, 478(3):897–906, 2008.

[15] M. G. Bobra, S. J. Mumford, R. J. Hewett, S. D. Christe, K. Reardon, S. Savage, J. Ireland, T. Pereira, B. Chen, and D. Pérez-Suárez. A survey of computational tools in solar physics. *Solar Physics*, 295(4):1–15, 2020.

[16] J.-L. Bougeret, K. Goetz, M. Kaiser, S. Bale, P. Kellogg, M. Maksimovic, N. Monge, S. Monson, P. Astier, S. Davy, et al. S/waves: The radio and plasma wave investigation on the stereo mission. *Space Science Reviews*, 136(1):487–528, 2008.

[17] R. Brajša, G. Verbanac, M. Bandić, A. Hanslmeier, I. Skokić, and D. Sudar. A prediction for the 25th solar cycle maximum amplitude. *Astronomische Nachrichten*, 343(3):e2113960, 2022.

[18] J. Burkepile, A. Hundhausen, A. Stanger, O. St. Cyr, and J. Seiden. Role of projection effects on solar coronal mass ejection properties: 1. a study of cmes associated with limb activity. *Journal of Geophysical Research: Space Physics*, 109(A3), 2004.

[19] P. Chen. Coronal mass ejections: models and their observational basis. *Living Reviews in Solar Physics*, 8(1):1–92, 2011.

[20] P. Chen, S. Wu, K. Shibata, and C. Fang. Evidence of eit and moreton waves in numerical simulations. *The Astrophysical Journal*, 572(1):L99, 2002.

[21] P. Chen, C. Fang, and K. Shibata. A full view of eit waves. *The Astrophysical Journal*, 622(2):1202, 2005.

[22] J. Cheng and J. Qiu. The nature of cme-flare-associated coronal dimming. *The Astrophysical Journal*, 825(1):37, 2016.

[23] I. Chertok and V. Grechnev. Large-scale dimmings produced by solar coronal mass ejections according to soho/eit data in four euv lines. *Astronomy Reports*, 47(11): 934–945, 2003.

[24] G. Chikunova, K. Dissauer, T. Podladchikova, and A. M. Veronig. Coronal dimmings associated with coronal mass ejections on the solar limb. *The Astrophysical Journal*, 896(1):17, 2020.

[25] F. Clette, L. Svalgaard, J. M. Vaquero, and E. W. Cliver. Revisiting the sunspot number. *Space Science Reviews*, 186(1):35–103, 2014.

[26] E. W. Cliver. History of research on solar energetic particle (sep) events: the evolving paradigm. *Proceedings of the International Astronomical Union*, 4(S257): 401–412, 2008.

[27] N. L. consortium and S. team. Soho lasco cme catalog. `https://cdaw.gsfc.nasa.gov/CME_list/`. Accessed: 2022-11-25.

[28] A. contributors. World coordinate system (astropy.wcs). `https://docs.astropy.org/en/stable/wcs/index.html`, . Accessed: 2022-11-20.

[29] L. contributors. Region_grow. `https://www.l3harrisgeospatial.com/docs/region_grow.html`, . Accessed: 2022-11-20.

[30] N. Crooker. Solar and heliospheric geoeffective disturbances. *Journal of Atmospheric and Solar-Terrestrial Physics*, 62(12):1071–1085, 2000.

[31] R. Cunha-Silva, C. Selhorst, F. Fernandes, and A. O. e Silva. Well-defined euv wave associated with a cme-driven shock. *Astronomy & Astrophysics*, 612:A100, 2018.

[32] J.-P. Delaboudiniere, G. Artzner, J. Brunaud, A. H. Gabriel, J.-F. Hochedez, F. Millier, X. Song, B. Au, K. Dere, R. A. Howard, et al. Eit: extreme-ultraviolet imaging telescope for the soho mission. In *The SOHO Mission*, pages 291–312. Springer, 1995.

[33] K. Dissauer, M. Temmer, A. M. Veronig, K. Vanninathan, and J. Magdalenić. Projection effects in coronal dimmings and associated euv wave event. *The Astrophysical Journal*, 830(2):92, 2016.

[34] K. Dissauer, A. M. Veronig, M. Temmer, T. Podladchikova, and K. Vanninathan. On the detection of coronal dimmings and the extraction of their characteristic properties. *The Astrophysical Journal*, 855(2):137, 2018.

[35] K. Dissauer, A. M. Veronig, M. Temmer, T. Podladchikova, and K. Vanninathan. Statistics of coronal dimmings associated with coronal mass ejections. i. characteristic dimming properties and flare association. *The Astrophysical Journal*, 863(2): 169, 2018.

[36] K. Dissauer, A. M. Veronig, M. Temmer, and T. Podladchikova. Statistics of coronal dimmings associated with coronal mass ejections. ii. relationship between coronal dimmings and their associated cmes. *The Astrophysical Journal*, 874(2):123, 2019.

[37] G. Dittberner, R. Gird, R. Heymann, E. Howard, S. Kirkner, and L. Uccellini. Noaa's future earth observations from advanced goes satellites. *Acta astronautica*, 38(4-8):467–477, 1996.

[38] C. Downs, I. I. Roussev, B. van der Holst, N. Lugaz, I. V. Sokolov, and T. I. Gombosi. Studying extreme ultraviolet wave transients with a digital laboratory: direct comparison of extreme ultraviolet wave observations to global magnetohydrodynamic simulations. *The Astrophysical Journal*, 728(1):2, 2011.

[39] M. Dumbović, A. Veronig, T. Podladchikova, J. K. Thalmann, G. Chikunova, K. Dissauer, J. Magdalenić, M. Temmer, J. Guo, and E. Samara. 2019 international women's day event-two-step solar flare with multiple eruptive signatures and low earth impact. *Astronomy & Astrophysics*, 652:A159, 2021.

[40] A. Emslie, H. Kucharek, B. Dennis, N. Gopalswamy, G. Holman, G. Share, A. Vourlidas, T. Forbes, P. Gallagher, G. Mason, et al. Energy partition in two solar flare/cme events. *Journal of Geophysical Research: Space Physics*, 109(A10), 2004.

[41] F. Eparvier. The extreme ultraviolet and x-ray irradiance sensors (exis) on goes-r: Measurements, calibration, validation, and data products.

[42] F. G. Eparvier, D. Crotser, A. R. Jones, W. E. McClintock, M. Snow, and T. N. Woods. The extreme ultraviolet sensor (euvs) for goes-r. In *Solar Physics and Space Weather Instrumentation III*, volume 7438, pages 31–38. SPIE, 2009.

[43] F. Epavier, T. Woods, A. Jones, M. Snow, D. Woodraska, E. Thiemann, W. Mc-

Clintock, M. Anfinson, R. Viereck, J. Machol, et al. The extreme ultraviolet and x-ray irradiance sensors (exis) on goes-16: Measurements, data products, and first results. In *EGU General Assembly Conference Abstracts*, page 9954, 2017.

[44] R. Erdélyi and I. Ballai. Heating of the solar and stellar coronae: a review. *Astronomische Nachrichten: Astronomical Notes*, 328(8):726–733, 2007.

[45] C. Eyles, R. Harrison, C. J. Davis, N. Waltham, B. Shaughnessy, H. Mapson-Menard, D. Bewsher, S. Crothers, J. Davies, G. Simnett, et al. The heliospheric imagers onboard the stereo mission. *Solar Physics*, 254(2):387–445, 2009.

[46] J. Feynman and S. Gabriel. On space weather consequences and predictions. *Journal of Geophysical Research: Space Physics*, 105(A5):10543–10564, 2000.

[47] S. Freeland and B. Handy. Data analysis with the solarsoft system. *Solar Physics*, 182(2):497–500, 1998.

[48] P. T. Gallagher and D. M. Long. Large-scale bright fronts in the solar corona: a review of "eit waves". *Space science reviews*, 158(2):365–396, 2011.

[49] K. Galsgaard and A. Longbottom. Formation of solar prominences by flux convergence. *The Astrophysical Journal*, 510(1):444, 1999.

[50] A. B. Galvin, L. M. Kistler, M. A. Popecki, C. J. Farrugia, K. D. Simunac, L. Ellis, E. Möbius, M. A. Lee, M. Boehm, J. Carroll, et al. The plasma and suprathermal ion composition (plastic) investigation on the stereo observatories. *Space Science Reviews*, 136(1):437–486, 2008.

[51] C. Gebhardt. Carrington event still provides warning of sun's potential 161 years later, 2020. URL `https://www.nasaspaceflight.com/2020/08/carrington-event-warning/`.

[52] P. A. Gilman. Magnetohydrodynamic "shallow water" equations for the solar tachocline. *The Astrophysical Journal*, 544(1):L79, 2000.

[53] C. Gohd. Solar geomagnetic storms could threaten more satellites after elon musk's starlink, 2022. URL `https://www.space.com/solar-geomagnetic-storms-spacex-starlink-threat`.

[54] S. J. Goodman, R. J. Blakeslee, W. J. Koshak, D. Mach, J. Bailey, D. Buechler, L. Carey, C. Schultz, M. Bateman, E. McCaul Jr, et al. The goes-r geostationary lightning mapper (glm). *Atmospheric research*, 125:34–49, 2013.

[55] N. Gopalswamy, A. Lara, R. Lepping, M. Kaiser, D. Berdichevsky, and O. St. Cyr.

Interplanetary acceleration of coronal mass ejections. *Geophysical research letters*, 27(2):145–148, 2000.

[56] N. Gopalswamy, S. Nunes, S. Yashiro, and R. Howard. Variability of solar eruptions during cycle 23. *Advances in Space Research*, 34(2):391–396, 2004.

[57] N. Gopalswamy, S. Yashiro, G. Michalek, G. Stenborg, A. Vourlidas, S. Freeland, and R. Howard. The soho/lasco cme catalog. *Earth, Moon, and Planets*, 104(1): 295–313, 2009.

[58] G. E. Hale. Solar vortices (contributions from the mt. wilson solar observatory, no. 26). *The Astrophysical Journal*, 28:100, 1908.

[59] G. E. Hale, F. Ellerman, S. B. Nicholson, and A. H. Joy. The magnetic polarity of sun-spots. *The Astrophysical Journal*, 49:153, 1919.

[60] L. K. Harra and A. C. Sterling. Material outflows from coronal intensity "dimming regions" during coronal mass ejection onset. *The Astrophysical Journal*, 561(2): L215, 2001.

[61] R. Harrison. The nature of solar flares associated with coronal mass ejection. *Astronomy and Astrophysics*, 304:585, 1995.

[62] R. Harrison and M. Lyons. A spectroscopic study of coronal dimming associated with a coronal mass ejection. *Astronomy and Astrophysics*, 358:1097–1108, 2000.

[63] H. Hayakawa, Y. Ebihara, D. M. Willis, S. Toriumi, T. Iju, K. Hattori, M. N. Wild, D. M. Oliveira, I. Ermolli, J. R. Ribeiro, et al. Temporal and spatial evolutions of a large sunspot group and great auroral storms around the carrington event in 1859. *Space Weather*, 17(11):1553–1569, 2019.

[64] H. R. Helal and A. Galal. An early prediction of the maximum amplitude of the solar cycle 25. *Journal of Advanced Research*, 4(3):275–278, 2013.

[65] T. Horbury, H. O'brien, I. C. Blazquez, M. Bendyk, P. Brown, R. Hudson, V. Evans, T. Oddy, C. Carr, T. Beek, et al. The solar orbiter magnetometer. *Astronomy & Astrophysics*, 642:A9, 2020.

[66] L. House, W. Wagner, E. Hildner, C. Sawyer, and H. Schmidt. Studies of the corona with the solar maximum mission coronagraph/polarimeter. *The Astrophysical Journal*, 244:L117–L121, 1981.

[67] R. A. Howard, J. Moses, A. Vourlidas, J. Newmark, D. G. Socker, S. P. Plunkett,

C. M. Korendyke, J. Cook, A. Hurley, J. Davila, et al. Sun earth connection coronal and heliospheric investigation (secchi). *Space Science Reviews*, 136(1):67–115, 2008.

[68] H. Hudson and E. Cliver. Observing coronal mass ejections without coronagraphs. *Journal of Geophysical Research: Space Physics*, 106(A11):25199–25213, 2001.

[69] H. Hudson, L. Acton, D. Alexander, S. Freeland, J. Lemen, and K. Harvey. Yohkoh/sxt soft x-ray observations of sudden mass loss from the solar corona. In *AIP Conference Proceedings*, volume 382, pages 88–91. American Institute of Physics, 1996.

[70] H. Hudson, L. Acton, and S. Freeland. A long-duration solar flare with mass ejection and global consequences. *The Astrophysical Journal*, 470:629, 1996.

[71] A. Hundhausen. Coronal mass ejections. In *The Many Faces of the Sun*, pages 143–200. Springer, 1999.

[72] A. J. Hundhausen. *The Solar Wind*, pages 91–128. Cambridge University Press, 1995. doi: 10.1017/9781139878296.005.

[73] N. Hurlburt, S. L. Freeland, S. Timothy, P. Shirts, and G. Slater. The Future Of SolarSoft. In *American Astronomical Society Meeting Abstracts*, volume 53 of *American Astronomical Society Meeting Abstracts*, page 213.01, June 2021.

[74] K. Ichimoto. Spectropolarimetry and magnetic structures. In *The Sun as a Guide to Stellar Physics*, pages 185–206. Elsevier, 2019.

[75] R. Illing and A. Hundhausen. Observation of a coronal transient from 1.2 to 6 solar radii. *Journal of Geophysical Research: Space Physics*, 90(A1):275–282, 1985.

[76] C. Jiang, X. Feng, S. Wu, and Q. Hu. Magnetohydrodynamic simulation of a sigmoid eruption of active region 11283. *The Astrophysical Journal Letters*, 771(2): L30, 2013.

[77] C. Jiang, S. Wu, X. Feng, and Q. Hu. Formation and eruption of an active region sigmoid. i. a study by nonlinear force-free field modeling. *The Astrophysical Journal*, 780(1):55, 2013.

[78] M. Jin, M. Ding, P. Chen, C. Fang, and S. Imada. Coronal mass ejection induced outflows observed with hinode/eis. *The Astrophysical Journal*, 702(1):27, 2009.

[79] S. Kahler and H. Hudson. Origin and development of transient coronal holes. *Journal of Geophysical Research: Space Physics*, 106(A12):29239–29247, 2001.

[80] M. L. Kaiser, T. Kucera, J. Davila, O. St Cyr, M. Guhathakurta, and E. Christian. The stereo mission: An introduction. *Space Science Reviews*, 136(1):5–16, 2008.

[81] E. K. Kilpua, S. W. Good, E. Palmerio, E. Asvestari, E. Lumme, M. Ala-Lahti, M. M. Kalliokoski, D. E. Morosan, J. Pomoell, D. J. Price, et al. Multipoint observations of the june 2012 interacting interplanetary flux ropes. *Frontiers in Astronomy and Space Sciences*, 6:50, 2019.

[82] J. A. Klimchuk. Key aspects of coronal heating. *Philosophical Transactions of the Royal Society A: Mathematical, Physical and Engineering Sciences*, 373(2042): 20140256, 2015.

[83] D. J. Knipp, B. J. Fraser, M. Shea, and D. Smart. On the little-known consequences of the 4 august 1972 ultra-fast coronal mass ejecta: Facts, commentary, and call to action. *Space Weather*, 16(11):1635–1643, 2018.

[84] H. E. Koskinen, D. N. Baker, A. Balogh, T. Gombosi, A. Veronig, and R. von Steiger. Achievements and challenges in the science of space weather. *Space Science Reviews*, 212(3):1137–1157, 2017.

[85] T. Kosugi, T. Sakao, S. Masuda, K. Makishima, M. Inda, T. Murakami, Y. Ogawara, K. Yaji, and K. Matsushita. The hard x-ray telescope (hxt) onboard yohkoh-its performance and some initial results. *Publications of the Astronomical Society of Japan*, 44:L45–L49, 1992.

[86] B. T. Kress, J. V. Rodriguez, and T. G. Onsager. The goes-r space environment in situ suite (seiss): Measurement of energetic particles in geospace. In *The GOES-R Series*, pages 243–250. Elsevier, 2020.

[87] L. D. Krista and A. A. Reinard. Statistical study of solar dimmings using codit. *The Astrophysical Journal*, 839(1):50, 2017.

[88] P. Kumar, K.-S. Cho, P. Chen, S.-C. Bong, and S.-H. Park. Multiwavelength study of a solar eruption from ar noaa 11112: Ii. large-scale coronal wave and loop oscillation. *Solar Physics*, 282(2):523–541, 2013.

[89] M. Kuperus and M. Raadu. The support of prominences formed in neutral sheets. *Astronomy and Astrophysics*, 31:189, 1974.

[90] L. Lanzerotti, D. Thomson, and C. Maclennan. Modern radio science, 1999.

[91] J. R. Lemen, D. J. Akin, P. F. Boerner, C. Chou, J. F. Drake, D. W. Duncan, C. G. Edwards, F. M. Friedlaender, G. F. Heyman, N. E. Hurlburt, et al. The

atmospheric imaging assembly (aia) on the solar dynamics observatory (sdo). In *The solar dynamics observatory*, pages 17–40. Springer, 2011.

[92] Y. D. Liu, J. G. Luhmann, N. Lugaz, C. Möstl, J. A. Davies, S. D. Bale, and R. P. Lin. On sun-to-earth propagation of coronal mass ejections. *The astrophysical journal*, 769(1):45, 2013.

[93] F. López, H. Cremades, L. A. Balmaceda, F. A. Nuevo, and A. Vásquez. Estimating the mass of cmes from the analysis of euv dimmings. *Astronomy & Astrophysics*, 627:A8, 2019.

[94] F. M. López, M. Hebe Cremades, F. A. Nuevo, L. A. Balmaceda, and A. M. Vásquez. Mass-loss evolution in the euv low corona from sdo/aia data. *Solar Physics*, 292(1): 1–19, 2017.

[95] C. H. Mandrini, M. S. Nakwacki, G. Attrill, L. van Driel-Gesztelyi, P. Démoulin, S. Dasso, and H. Elliott. Are cme-related dimmings always a simple signature of interplanetary magnetic cloud footpoints? *Solar Physics*, 244(1):25–43, 2007.

[96] H. M. Marianna Korsos. The sun's atmosphere is hundreds of times hotter than its surface – here's why, 2021. URL `https://theconversation.com/the-suns-atmosphere-is-hundreds-of-times-hotter-than-its-surface-heres-why-16`

[97] J. P. Mason, T. N. Woods, A. Caspi, B. J. Thompson, and R. A. Hock. Mechanisms and observations of coronal dimming for the 2010 august 7 event. *The Astrophysical Journal*, 789(1):61, 2014.

[98] J. P. Mason, T. N. Woods, D. F. Webb, B. J. Thompson, R. C. Colaninno, and A. Vourlidas. Relationship of euv irradiance coronal dimming slope and depth to coronal mass ejection speed and mass. *The Astrophysical Journal*, 830(1):20, 2016.

[99] R. A. Meyers. *Encyclopedia of physical science and technology*. Academic, 2002.

[100] M. Moldwin. *An introduction to space weather*. Cambridge University Press, 2008.

[101] D. Moses, F. Clette, J.-P. Delaboudinière, G. Artzner, M. Bougnet, J. Brunaud, C. Carabetian, A. Gabriel, J.-F. Hochedez, F. Millier, et al. Eit observations of the extreme ultraviolet sun. In *The First Results from SOHO*, pages 571–599. Springer, 1997.

[102] N. Muhr, A. M. Veronig, I. W. Kienreich, B. Vršnak, M. Temmer, and B. M. Bein. Statistical analysis of large-scale euv waves observed by stereo/euvi. *Solar Physics*, 289(12):4563–4588, 2014.

[103] A. Muñoz-Jaramillo, D. Nandy, and P. C. Martens. Helioseismic data inclusion in solar dynamo models. *The Astrophysical Journal*, 698(1):461, 2009.

[104] N. V. Nitta, C. J. Schrijver, W. Liu, et al. Large-scale coronal propagating fronts in solar eruptions as observed by the atmospheric imaging assembly on board the solar dynamics observatory—an ensemble study. *The Astrophysical Journal*, 776(1): 58, 2013.

[105] NOAA/SWPC. About space weather phenomena, 2015. URL `https://www.swpc.noaa.gov/phenomena`.

[106] M. J. Owens and R. J. Forsyth. The heliospheric magnetic field. *Living Reviews in Solar Physics*, 10(1):1–52, 2013.

[107] D. T. Oyedokun and P. J. Cilliers. Geomagnetically induced currents: A threat to modern power systems. In *Classical and recent aspects of power system optimization*, pages 421–462. Elsevier, 2018.

[108] E. N. Parker. Hydromagnetic dynamo models. *The Astrophysical Journal*, 122:293, 1955.

[109] E. N. Parker. Dynamics of the interplanetary gas and magnetic fields. *The Astrophysical Journal*, 128:664, 1958.

[110] S. Patsourakos and A. Vourlidas. On the nature and genesis of euv waves: a synthesis of observations from soho, stereo, sdo, and hinode (invited review). *Solar Physics*, 281(1):187–222, 2012.

[111] W. D. Pesnell, B. J. Thompson, and P. Chamberlin. The solar dynamics observatory (sdo). In *The solar dynamics observatory*, pages 3–15. Springer, 2011.

[112] G. J. Petrie. Photospheric and coronal observations of abrupt magnetic restructuring in two flaring active regions. *Solar Physics*, 291(3):791–821, 2016.

[113] O. Podladchikova and D. Berghmans. Automated detection of eit waves and dimmings. *Solar Physics*, 228(1):265–284, 2005.

[114] T. Podladchikova, A. M. Veronig, K. Dissauer, M. Temmer, and O. Podladchikova. Three-dimensional reconstructions of extreme-ultraviolet wave front heights and their influence on wave kinematics. *The Astrophysical Journal*, 877(2):68, 2019.

[115] A. Prasad, K. Dissauer, Q. Hu, R. Bhattacharyya, A. M. Veronig, S. Kumar, and B. Joshi. Magnetohydrodynamic simulation of magnetic null-point reconnections

and coronal dimmings during the x2. 1 flare in noaa ar 11283. *The Astrophysical Journal*, 903(2):129, 2020.

[116] J. Qiu and J. Cheng. Gradual solar coronal dimming and evolution of coronal mass ejectionin the early phase. *The Astrophysical Journal Letters*, 838(1):L6, 2017.

[117] M. S. Quassim, A.-F. Attia, and H. K. Elminir. Forecasting the peak amplitude of the 24th and 25th sunspot cycles and accompanying geomagnetic activity. *Solar Physics*, 243(2):253–258, 2007.

[118] A. Reinard and D. Biesecker. Coronal mass ejection-associated coronal dimmings. *The Astrophysical Journal*, 674(1):576, 2008.

[119] A. Reinard and D. Biesecker. The relationship between coronal dimming and coronal mass ejection properties. *The Astrophysical Journal*, 705(1):914, 2009.

[120] E. Robbrecht and D. Berghmans. Automated recognition of coronal mass ejections (cmes) in near-real-time data. *Astronomy & Astrophysics*, 425(3):1097–1106, 2004.

[121] E. Robbrecht, D. Berghmans, and R. Van der Linden. Automated lasco cme catalog for solar cycle 23: are cmes scale invariant? *The Astrophysical Journal*, 691(2):1222, 2009.

[122] P. Romano, F. Zuccarello, S. Guglielmino, F. Berrilli, R. Bruno, V. Carbone, G. Consolini, M. De Lauretis, D. Del Moro, A. Elmhamdi, et al. Recurrent flares in active region noaa 11283. *Astronomy & Astrophysics*, 582:A55, 2015.

[123] D. M. Rust. Coronal disturbances and their terrestrial effects. *Space Science Reviews*, 34(1):21–36, 1983.

[124] P. H. Scherrer, J. Schou, R. Bush, A. Kosovichev, R. Bogart, J. Hoeksema, Y. Liu, T. Duvall, J. Zhao, C. Schrijver, et al. The helioseismic and magnetic imager (hmi) investigation for the solar dynamics observatory (sdo). *Solar Physics*, 275(1):207–227, 2012.

[125] T. J. Schmit, P. Griffith, M. M. Gunshor, J. M. Daniels, S. J. Goodman, and W. J. Lebair. A closer look at the abi on the goes-r series. *Bulletin of the American Meteorological Society*, 98(4):681–698, 2017.

[126] R. Schwenn. Space weather: The solar perspective. *Living reviews in solar physics*, 3(1):1–72, 2006.

[127] L. G. Shapiro, G. C. Stockman, et al. *Computer vision*, volume 3. Prentice Hall New Jersey, 2001.

[128] C. Shen, K. K. Reeves, J. C. Raymond, N. A. Murphy, Y.-K. Ko, J. Lin, Z. Mikić, and J. A. Linker. Non-equilibrium ionization modeling of the current sheet in a simulated solar eruption. *The Astrophysical Journal*, 773(2):110, 2013.

[129] Y. Shen and Y. Liu. Simultaneous observations of a large-scale wave event in the solar atmosphere: From photosphere to corona. *The Astrophysical Journal Letters*, 752(2):L23, 2012.

[130] H. Singer, L. Matheson, R. Grubb, A. Newman, and D. Bouwer. Monitoring space weather with the goes magnetometers. In *GOES-8 and Beyond*, volume 2812, pages 299–308. SPIE, 1996.

[131] A. C. Sterling and H. S. Hudson. Yohkoh sxt observations of x-ray "dimming" associated with a halo coronal mass ejection. *The Astrophysical Journal*, 491(1): L55, 1997.

[132] M. Temmer, A. Veronig, B. Vršnak, J. Rybák, P. Gömöry, S. Stoiser, and D. Maričić. Acceleration in fast halo cmes and synchronized flare hxr bursts. *The Astrophysical Journal*, 673(1):L95, 2008.

[133] M. Temmer, A. Veronig, E. Kontar, S. Krucker, and B. Vršnak. Combined stereo/rhessi study of coronal mass ejection acceleration and particle acceleration in solar flares. *The Astrophysical Journal*, 712(2):1410, 2010.

[134] M. Temmer, A. Veronig, N. Gopalswamy, and S. Yashiro. Relation between the 3d-geometry of the coronal wave and associated cme during the 26 april 2008 event. In *Energy Storage and Release through the Solar Activity Cycle*, pages 115–126. Springer, 2011.

[135] The SunPy Community, W. T. Barnes, M. G. Bobra, S. D. Christe, N. Freij, L. A. Hayes, J. Ireland, S. Mumford, D. Perez-Suarez, D. F. Ryan, A. Y. Shih, P. Chanda, K. Glogowski, R. Hewett, V. K. Hughitt, A. Hill, K. Hiware, A. Inglis, M. S. F. Kirk, S. Konge, J. P. Mason, S. A. Maloney, S. A. Murray, A. Panda, J. Park, T. M. D. Pereira, K. Reardon, S. Savage, B. M. Sipőcz, D. Stansby, Y. Jain, G. Taylor, T. Yadav, Rajul, and T. K. Dang. The sunpy project: Open source development and status of the version 1.0 core package. *The Astrophysical Journal*, 890:68–, 2020. doi: 10.3847/1538-4357/ab4f7a. URL `https://iopscience.iop.org/article/10.3847/1538-4357/ab4f7a`.

[136] A. Thernisien, A. Vourlidas, and R. Howard. Cme reconstruction: pre-stereo and stereo era. *Journal of Atmospheric and Solar-Terrestrial Physics*, 73(10):1156–1165, 2011.

[137] B. Thompson and D. Myers. A catalog of coronal “eit wave” transients. *The Astrophysical Journal Supplement Series*, 183(2):225, 2009.

[138] B. Thompson, S. Plunkett, J. Gurman, J. Newmark, O. St. Cyr, and D. Michels. Soho/eit observations of an earth-directed coronal mass ejection on may 12, 1997. *Geophysical Research Letters*, 25(14):2465–2468, 1998.

[139] B. Thompson, E. Cliver, N. Nitta, C. Delannée, and J.-P. Delaboudiniere. Coronal dimmings and energetic cmes in april-may 1998. *Geophysical research letters*, 27 (10):1431–1434, 2000.

[140] W. Thompson. Cds software note no. 49. *Deriving Statistics from NIS data*, 1998.

[141] W. T. Thompson, J. M. Davila, R. R. Fisher, L. E. Orwig, J. E. Mentzell, S. E. Hetherington, R. J. Derro, R. E. Federline, D. C. Clark, P. T. Chen, et al. The cor1 inner coronagraph for stereo-secchi. In *Innovative Telescopes and Instrumentation for Solar Astrophysics*, volume 4853, pages 1–11. SPIE, 2003.

[142] D. D. Tim Sharp. The sun’s atmosphere: Photosphere, chromosphere and corona, 2022. URL `https://www.space.com/17160-sun-atmosphere.html`.

[143] K. Vanninathan, A. M. Veronig, K. Dissauer, and M. Temmer. Plasma diagnostics of coronal dimming events. *The Astrophysical Journal*, 857(1):62, 2018.

[144] G. Vasudevan, L. Shing, D. Mathur, C. Edwards, M. Shaw, D. Seaton, and J. Darnel. Design and on-orbit calibration of the solar ultraviolet imager (suvi) on the goes-r series weather satellite. In *International Conference on Space Optics—ICSO 2018*, volume 11180, pages 2769–2778. SPIE, 2019.

[145] A. Veronig, P. Odert, M. Leitzinger, K. Dissauer, N. Fleck, and H. Hudson. First detections of stellar coronal mass ejections through coronal dimmings. 2020.

[146] C. Vita-Finzi. *The sun: A user’s manual.* Springer Science & Business Media, 2008.

[147] A. Vourlidas, R. A. Howard, E. Esfandiari, S. Patsourakos, S. Yashiro, and G. Michalek. Comprehensive analysis of coronal mass ejection mass and energy properties over a full solar cycle. *The Astrophysical Journal*, 722(2):1522, 2010.

[148] A. Vourlidas, R. Howard, E. Esfandiari, S. Patsourakos, S. Yashiro, and G. Michalek. Erratum:“comprehensive analysis of coronal mass ejection mass and energy properties over a full solar cycle”(2010, apj, 722, 1522). *The Astrophysical Journal*, 730 (1):59, 2011.

[149] A. Vourlidas, B. J. Lynch, R. A. Howard, and Y. Li. How many cmes have flux ropes?

deciphering the signatures of shocks, flux ropes, and prominences in coronagraph observations of cmes. *Solar Physics*, 284(1):179–201, 2013.

[150] B. Vršnak and T. Žic. Transit times of interplanetary coronal mass ejections and the solar wind speed. *Astronomy & Astrophysics*, 472(3):937–943, 2007.

[151] B. Vršnak, D. Sudar, and D. Ruždjak. The cme-flare relationship: Are there really two types of cmes? *Astronomy & Astrophysics*, 435(3):1149–1157, 2005.

[152] B. Vršnak, D. Maričić, A. L. Stanger, A. M. Veronig, M. Temmer, and D. Roša. Acceleration phase of coronal mass ejections: I. temporal and spatial scales. *Solar Physics*, 241(1):85–98, 2007.

[153] A. Warmuth. Large-scale globally propagating coronal waves. *Living Reviews in Solar Physics*, 12(1):1–101, 2015.

[154] D. Webb and A. Hundhausen. Activity associated with the solar origin of coronal mass ejections. *Solar physics*, 108(2):383–401, 1987.

[155] D. Webb, E. Cliver, N. Crooker, O. St. Cyr, and B. Thompson. Relationship of halo coronal mass ejections, magnetic clouds, and magnetic storms. *Journal of Geophysical Research: Space Physics*, 105(A4):7491–7508, 2000.

[156] D. Webb, R. Lepping, L. Burlaga, C. DeForest, D. Larson, S. Martin, S. Plunkett, and D. Rust. The origin and development of the may 1997 magnetic cloud. *Journal of Geophysical Research: Space Physics*, 105(A12):27251–27259, 2000.

[157] D. F. Webb and T. A. Howard. Coronal mass ejections: Observations. *Living Reviews in Solar Physics*, 9(1):1–83, 2012.

[158] B. Wood, R. Howard, A. Thernisien, S. Plunkett, and D. Socker. Reconstructing the 3d morphology of the 17 may 2008 cme. *Solar Physics*, 259(1):163–178, 2009.

[159] T. Woods, F. Eparvier, R. Hock, A. Jones, D. Woodraska, D. Judge, L. Didkovsky, J. Lean, J. Mariska, H. Warren, et al. Extreme ultraviolet variability experiment (eve) on the solar dynamics observatory (sdo): Overview of science objectives, instrument design, data products, and model developments. *The solar dynamics observatory*, pages 115–143, 2010.

[160] J.-P. Wülser, J. R. Lemen, T. D. Tarbell, C. J. Wolfson, J. C. Cannon, B. A. Carpenter, D. W. Duncan, G. S. Gradwohl, S. B. Meyer, A. S. Moore, et al. Euvi: the stereo-secchi extreme ultraviolet imager. In *Telescopes and Instrumentation for Solar Astrophysics*, volume 5171, pages 111–122. SPIE, 2004.

[161] N. H. Zell. Layers of the sun. `https://www.nasa.gov/mission_pages/iris/multimedia/layerzoo.html`. Accessed: 2022-11-05.

[162] A. Zhukov and F. Auchère. On the nature of eit waves, euv dimmings and their link to cmes. *Astronomy & Astrophysics*, 427(2):705–716, 2004.

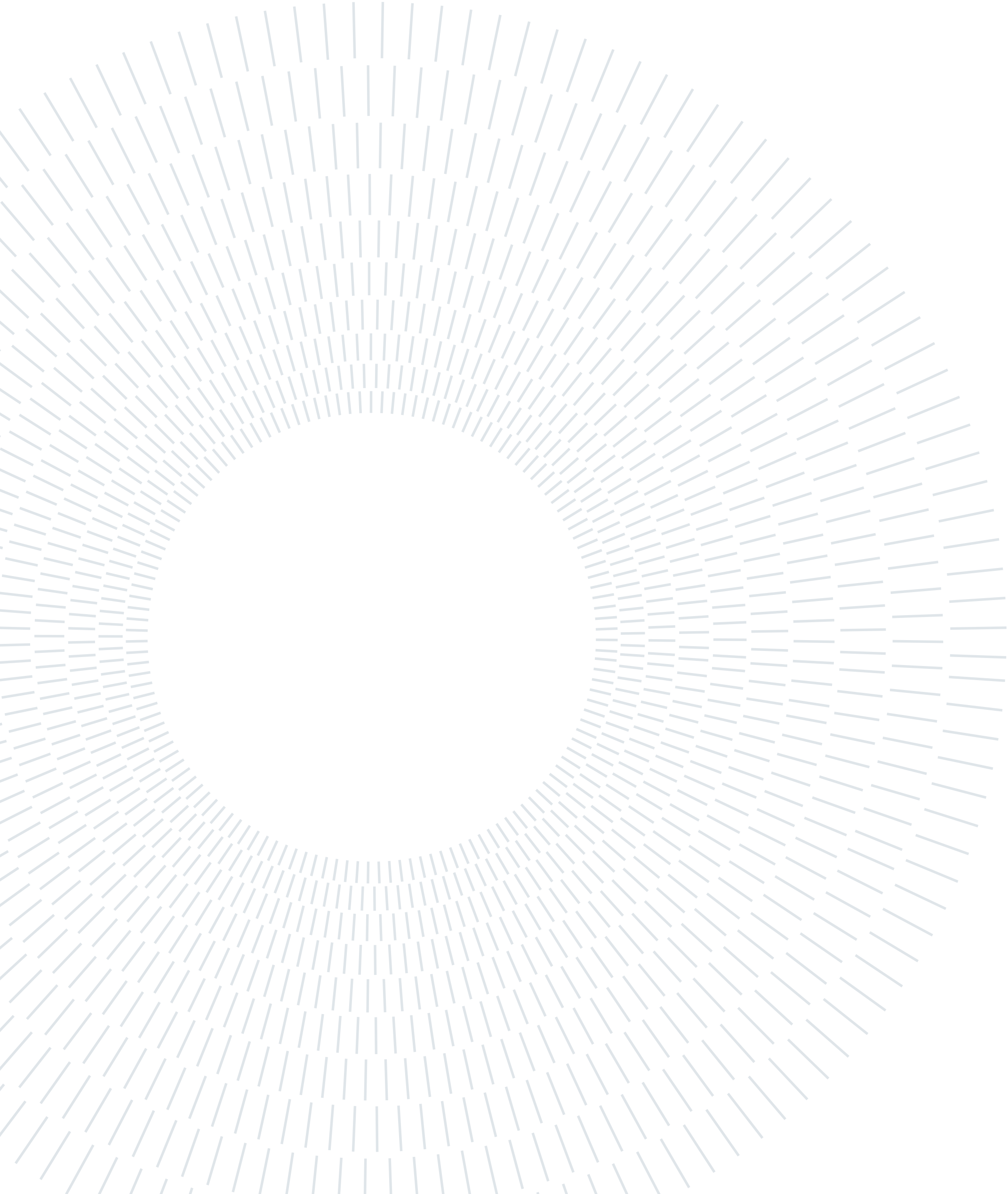

List of Figures

List of Tables

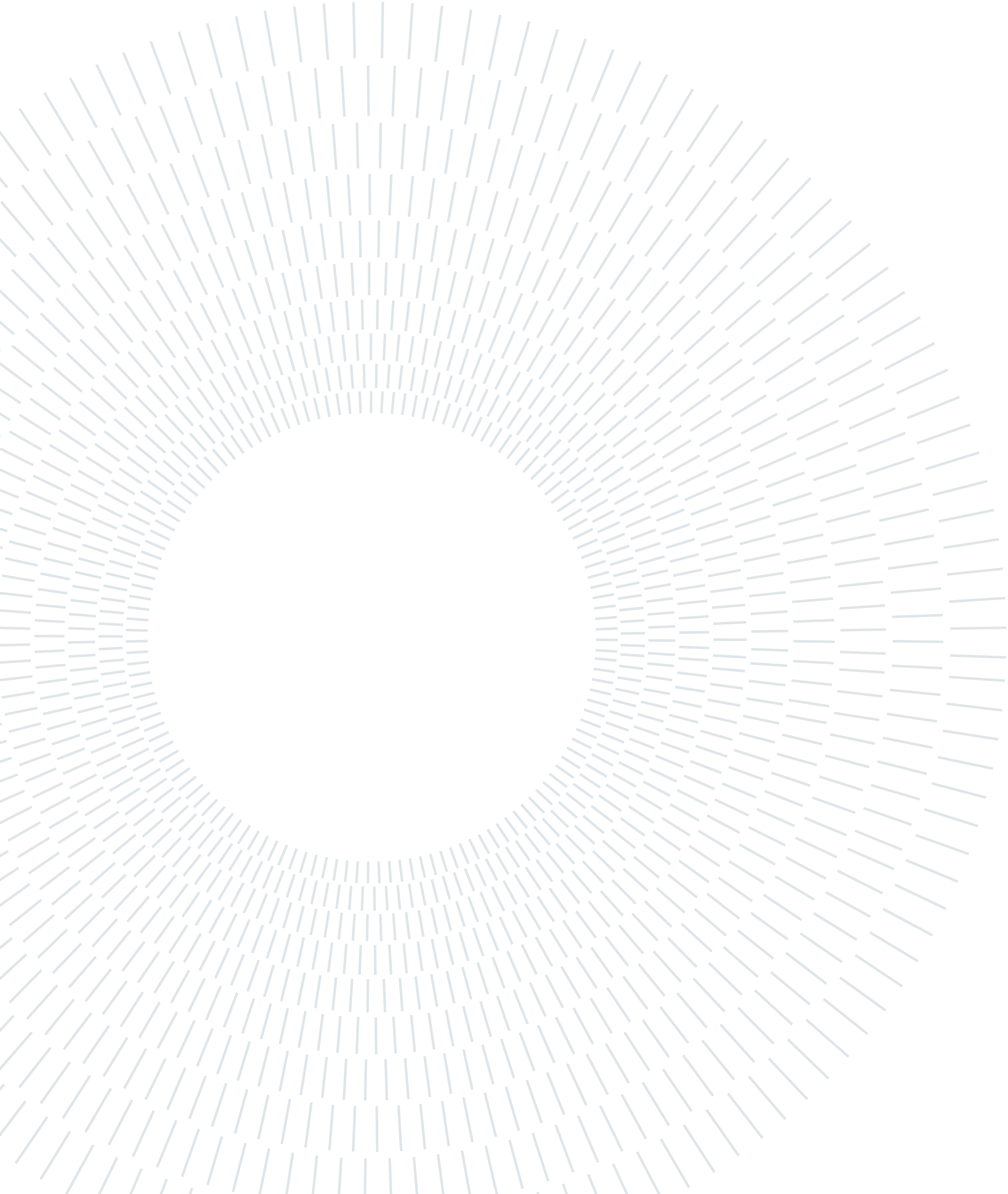

List of Symbols

Acronym	**Description**
AIA	Atmospheric Imaging Assembly
AR	Active Region
AU	Astronomical Unit
BD	Base-Difference
CH	Coronal Hole
CME	Coronal Mass Ejection
CoDiT	Coronal Dimming Tracker
DEM	Differential Emission Measure
EIT	Extreme-ultraviolet Imaging Telescope
EUV	Extreme Ultra-Violet
EUVI	Extreme UltraViolet Imager
EXIS	Extreme Ultraviolet X-Ray Irradiance Sensor
FITS	Flexible Image Transport System
GCR	Galactic Cosmic Rays
GOES	Geostationary Operational Environmental Satellites
HF	High Frequency
HMF	Heliospheric Magnetic Field
HMI	Helioseismic and Magnetic Imager
IDL	Interactive Data Language
IMF	Interplanetary Magnetic Field
LBR	Logarithmic Base-Ratio
MC	Magnetic Cloud
MHD	Magnetohydrodynamics
NEMO	Novel EIT wave Machine Observing
NL	Neutral Line

NOAA	National Oceanic and Atmospheric Association
RD	Running Difference
SDO	Solar Dynamics Observatory
SECCHI	Sun Earh Connection Coronal and Heliospheric Investigation
SEP	Solar Energetic Particles
SOHO	Solar and Heliospheric Observatory
SOT	Solar Optical Telescope
SSW	SolarSoftWare
STEREO	Solar TErrestrial RElations Observatory
STP	Solar Terrestrial Probes
SWPC	Space Weather Prediction Center
SXR	Soft X-Rays
TCH	Transient Coronal Hole
WCS	World Coordinate System
XRS	X-Ray Sensor

Symbol	**Description**	**units**
A	area	km^2
D	dimming mask	-
F	image frame	pixels
I	intensity	DN
p	pixel	-
$R_\odot$	Solar radius	km
t	time	s

Acknowledgements

I would like to express my thanks to professor Tatiana Podladchikova for letting me into the wonderful world of solar physics and Space Weather, and offering me the opportunity to be in Moscow and live Skoltech atmosphere, not only from behind a computer screen.

A special thanks to Galina Chikunova, because she assisted me since the very beginning and was a precious help and guide. Now, she is not only "the PhD student who helps me", but a friend.

I would like to thank PhD Karin Dissauer for the attention she paid to this work and her precious suggestions and corrections. I am so glad for having been together at the SOLARNET Summer School and finally meeting in person.

My gratitude also goes to professor Astrid Veronig, for the time invested in this work and for worthy insights on the subject.

Being part of this research group has been an amazing experience for me. Thank you everyone.

I would like to express my gratitude to professor Giovanni Consolati, for being supportive throughout my work, helping me with precision and punctuality, and for making the last step of this Master's go smoothly.